HIGH ORDER DNS FOR VORTEX STRUCTURE IN LATE FLOW TRANSITION

by

YONG YANG

Presented to the Faculty of the Graduate School of

The University of Texas at Arlington in Partial Fulfillment

of the Requirements

for the Degree of

DOCTOR OF PHILOSOPHY

THE UNIVERSITY OF TEXAS AT ARLINGTON

August 2017

Acknowledgements

I would like to thank my supervising professor and committee chairman, Dr. Chaoqun Liu, for his constantly support and guidance, and also for his encouragement and advice throughout my four years of doctoral program. I wish to thank my committee members Dr. Guojun Liao, Dr. Hristo V. Kojouharov and Dr. Jianzhong Su, for their support and for taking time to serve in my dissertation committee.

I would also like to thank the Department of Mathematics, for the financial support in my doctoral program. And I would like to thank all colleagues and friends for valuable advices and inspirations.

Most importantly, I would like to express my gratitude to my parents, who always stand by me. I am also extremely grateful to my wife Yiqi for her love, encouragement and patience and making this work a success.

July 17, 2017

Abstract

HIGH ORDER DNS FOR VORTEX STRUCTURE IN LATE FLOW TRANSITION

Yong Yang, PhD

The University of Texas at Arlington, 2017

Supervising Professor: Chaoqun Liu

Turbulence is still a world puzzle after over one hundred years research, and the current and classical theories brim with self-contradictions. C. Liu proposed a new theory on turbulence generation and structure after 28 years research, which are consistent without self-contradictions and well explain turbulence generation and structure.

Based on this new theory, this dissertation (1) gives some mathematical explanations for new vortex identify method – Ω method; (2) analyzes the instability of shear layer by applying Chebyshev spectrum method to solve Orr-Sommerfeld eigenvalue equation; (3) investigates the vortex structure development in late flow transition; (4) utilizes the proper orthogonal decomposition to find the principal components of the flow in late stage of transition because of the flow complexity caused by hairpin vortex packet intertwining and interacting with each other.

It is found that (1) Ω method can capture low-pressure region very well; (2) the high shear layer induced by the counter-rotation of two legs of Λ vortex ejection is unstable and the Λ vortex develops to a hairpin vortex packet with vortex rings generates; (3) streamwise vortices are principal in late stage of transition. It confirms the consistency of Liu's theory: a pair of streamwise vortices ejects the low speed zone up and high shear layer generates; because of the instability of the high shear layer in boundary layer, the vortex ring forms and hairpin vortex generates.

Table of Contents

List of Illustrations

List of Tables

Chapter 1

Introduction

Vortices are ubiquitously seen in nature, which range from smoke rings to clouds, from bubble rings to hurricanes, from swirl in the washing pool to whirlpools in the sea. Human have developed an intuitional concept of vortices as fluid regions with rotational motions since very ancient time, however, a rational description of vortices was not established until 19th century. People's understanding towards vortices was greatly deepened ever since and went through several historical stages.

Helmholtz [1] firstly gave the mathematical definition of vorticity as the curl of velocity field and further derived the well-known three vorticity theorems, which along with Kelvin's circulation theorem and others laid the foundation for this field. Since then vorticity and vortices dynamics has been a central topic in both fluid mechanics researches and textbooks. The classical monograph of Lamb [2] summarized this time's theoretical achievements of incompressible, ideal fluid, dealing with mostly irrotational flow with only a small part of rotational flow. Prandlt's ground-breaking boundary layer theory [3] and the invention of aircraft in the beginning of 20th century opened a new stage of vortical flow research. Prandlt's work revealed the fundamental importance of viscosity in fluid motion and explained that the circulation around the wing is generated by the viscous shearing process within the thin boundary layer. The rapid development of aeronautical techniques in this time is largely due to people's understanding, utilization and control of vortices, as summarized by Durand [4] and Goldstein [5].

At almost the same time, the important role of vortical structures in transitional and turbulent flow was recognized by researchers, as put by Küchemann's [6] famous quote "vortices are the sinews and muscles of turbulence". A few structure models are conjectured and proposed, such as "horseshoe" model and hairpin vortex. Theodorsen

[7] proposed the conceptual “horseshoe” vortex model (Figure 1-1) to describe generation and sustenance of turbulence. The model provided an instantaneous description of near wall dynamics and laid a foundation for study of “coherent structures”. Hairpin vortices have been recognized to be a typical vortical structure in transitional flows [8]–[12]. The difference between “horseshoe” vortex and “hairpin” vortex lies on the fact that the former is almost as wide as their normal height, while the latter is narrower with elongated legs [13] (Figure 1-2(a)). Thereafter, the subject received considerable attention from investigators.

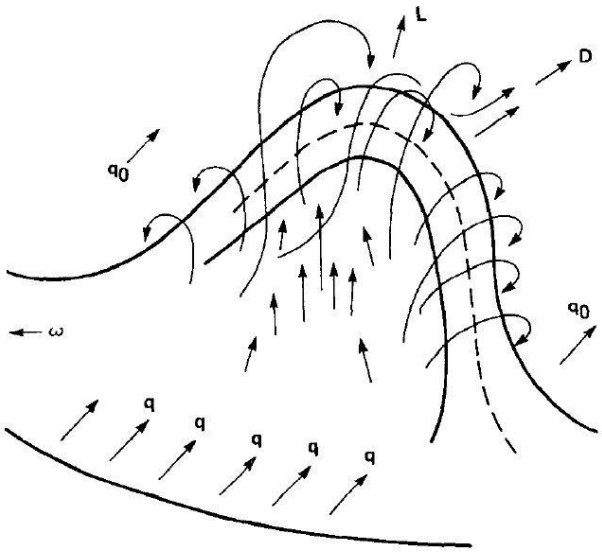

Figure 1-1 Horseshoe vortex

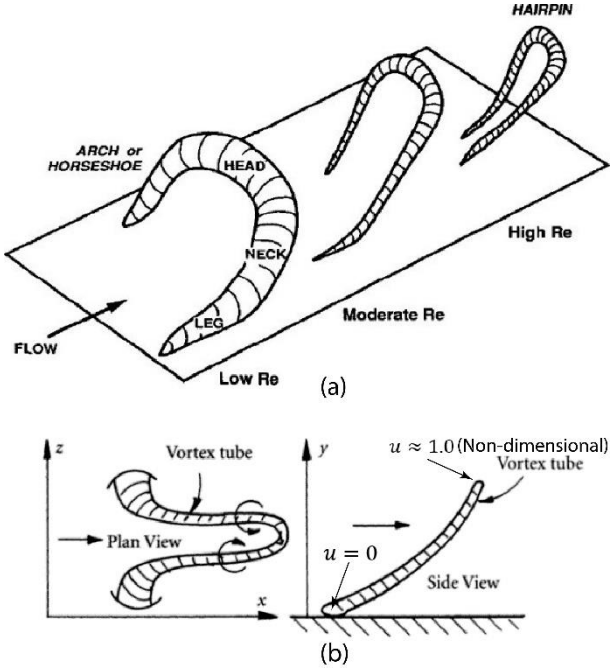

Figure 1-2 (a) Nomenclature for horseshoe or hairpin vortices; (b) Classical views on hairpin vortices.

The development of experimental techniques provided researchers richer information about the turbulent field than ever. Hama and Nutant [14] observed the formation and development of Λ-shaped vortices in experiment. Kline et al [15] observed the streamwise narrow streaks of high and low momentum fluid in boundary layer using hydrogen bubbles, Corino and Brodkey [16] observed that the “ejection” and “sweep” are driven by streamwise vortices.

After over a hundred year of study, researchers have figured out the linear and weakly non-linear stage of flow transition pretty well [17], [18]. However, it is the DNS and PIV emerged in the late 1980s that really enables researchers to directly observe the dynamical, detailed turbulent field and study the late non-linear transitional stage, especially DNS, which provided full information, 3D turbulence. Since the first DNS of channel [19] and turbulent boundary layer [20], many significant discoveries have been

made on the coherent structures in the transitional and turbulent flow based on DNS [21]. Smith et al. [22] acknowledged the hairpin vortex as the basic flow structures of turbulent boundary layer. It is argued the interaction of hairpin vortices with background shear, with each other, with the wall surface determines the central features of boundary layer flow. In Robinson's [23] review paper, a summary on conceptual models, idealized description of mechanism behind turbulence generation, is given. The dominant theme is hairpin vortex and its variations. Robinson [24] also describes the "quasi-streamwise vortices" as "one-legged" hairpins. These quasi-streamwise vortices and associated buffer layer streaks drew considerable attention [25] and are believed to be very important. Liu et al [26], [27] reported the whole process of K- and H-type transition in 1995 and 1996 and Rist [10] gave a quantitative comparison of experiment and direct numerical simulation in 2002. Adrian [28] gave a review about the hairpin vortex organization in boundary layer in 2007. Wu and Moin [11] reported a new DNS for flow transition on a flat plate and confirmed the coherent structures found by previous researchers [8], [29]. T. Sayadi et al [30] studied the vortices evolution in H and K type controlled transition process using DNS. C. Liu [31] proposed a new theory of turbulence generation and sustenance from the aspect of flow structure based on DNS analysis recently. Parallel to the research frontier, vorticity and vortices dynamics is also a central topic in fluid mechanics textbooks from Batchlor's classic [32] to more recent monographs by Saffman [33], Lugt [34], and Wu [35].

On the other hand, many studies have been focused on the stability analysis [36], [37]. Schoppa and Hussain [36] believes instability of ejected low-speed streaks directly generates new streamwise vortices near the wall. The vortex formation and turbulence production are assumed to be reliant on those low-speed streaks.

Bake et al. [10] experimentally and numerically investigated turbulence development in a boundary layer. The flow randomization is believed to be developed on the tip of the Λ-vortex, where the ring-like vortex with spikes induced locates. The role of ring-like vortices which is basically spanwise in inducing near-wall structures and generating pressure gradients is highlighted.

It is also noted that hairpin vortices always appear in packets [28], [38], [39]. Adrian [28] addressed that hairpin vortex packets together with quasi-streamwise vortices are prevalent coherent structures in wall turbulence. He also believes hairpins can autogenerate to form packets.

In Wallace's [40] recent review paper, it is argued that in spite of numerous attempts to relate the essential properties of turbulent boundary flow to its vortical structure, the investigation has not been very successful. Wallace also pointed out study on transitional boundary layer flows at low-Reynolds numbers, in which the vortical structures are more organized, might be very helpful in understanding turbulence generation and sustenance.

Vorticity is defined as the curl of velocity and interpreted as twice the local angular velocity of the fluid element. Because of the much simpler governing equations than velocity, vorticity received considerable attention from investigators. Classical fluid dynamics believes that vorticity cannot be generated nor destroyed within the interior of fluids, and it is transported inside the flow by advection and diffusion [41]. The physical meaning and properties of vorticity make itself of great value in investigating vortices dominant flows. Therefore, many researchers have tried to utilize vorticity magnitude to educe coherent structures and identify vortex cores in turbulent flows. As pointed out by Jeong and Hussain [42], however, this approach is not always successful, especially if the background shear is comparable to the vorticity magnitude within the vortex. It has

been recognized that vorticity does not represent global rotation, i.e. vortices. For example, a laminar boundary layer possesses vorticity, but there is clearly no rotational motion in the laminar boundary layer.

In spite of the stated consensus about vorticity, several concepts are still rather confusing in fluid mechanics. A flow is called irrotational if $\nabla \times \boldsymbol{V} = 0$ in all space, while a rotational flow simply indicates the vorticity is not zero somewhere [43]. The previous example of the laminar boundary layer can serve as a counterexample in which vorticity exists without any rotational motion or vortices. Evidently, there is a difference between vorticity (local quantity) and vortices (group rotation).

On the other hand, vortex definition and identification have been a longstanding issue. Robinson *et al.* [44] proposed a rather accurate definition: a vortex exists when instantaneous streamlines mapped onto a plane normal to the vortex core exhibit a roughly circular or spiral pattern, when viewed from a reference frame moving with the center of the vortex core. The definition, however, suffers from a requirement to identify the vortex core as a priori. In the meantime, several vortex identification methods are introduced trying to fulfil the need to investigate the vortex structures in turbulent flows.

Perry and Chong [45] suggested vortices exist where eigenvalues of velocity gradient tensor $\nabla \boldsymbol{V}$ are complex, which implies the streamline pattern is spiral or closed viewed from a reference frame moving with the point. The method, named the $\tilde{\Delta}$-method, was further developed by Zhou *et al.* [39]. They suggested employing iso-surfaces of imaginary part of the complex eigenvalue to capture vortices. Around the same time, the famous Q-criterion was introduced by Hunt, Wray, and Moin [46], in which an eddy is defined as the region with positive second invariant Q of the velocity gradient tensor. The idea behind this method is Q represents the balance between shear strain rate and vorticity magnitude since it can be derived that $Q = \frac{1}{2}(\left|\left|\boldsymbol{\Omega}\right|\right|^2 - ||\boldsymbol{S}||^2)$, where $\boldsymbol{S}$ and $\boldsymbol{\Omega}$ are

the symmetric and antisymmetric components of $\nabla \boldsymbol{V}$. Another well-known scheme is the λ_2 method, introduced by Jeong and Hussain [42]. They suggested the usage of second eigenvalue of the symmetric tensor $\boldsymbol{S}^2 + \boldsymbol{\Omega}^2$ trying to capture the pressure minimum in a plane normal to the vortex axis. Haller [47] and Shawn *et al* [48] used the concept of "finite time Lyapunov Exponent" to defined vortices boundary as the separatrix of stable and unstable manifolds, from a Lagrangian viewpoint.

All these methods have achieved some success. As demonstrated by Pierce, Moin and Sayadi [49], the $\tilde{\Delta}$, Q, λ_2 criteria can produce the same images when applied to DNS data of a transitional boundary layer provided appropriately iso-surface thresholds are chosen respectively. These criteria, however, suffer from some common issues. First, a case related threshold is required; second, the physical meaning of $\tilde{\Delta}$, Q, and λ_2 is unclear; third, inappropriate thresholds may lead to strong vortices captured while weak ones are skipped.

Opposite to current and classical theories brimming with self-contradictions, Liu [50] proposed a new theory on turbulence generation and structure after 28-years research, which are consistent without self-contradictions and well explain turbulence generation and structure:

1) Turbulent flow has unique and deterministic solution. Turbulence is not generated by vortex "breakdown", but vortex "buildup".

2) Vorticity and vortex are totally different concepts. A new vortex identification method has been given by Liu et al. [51], which has a unique threshold and physical meaning.

3) The nature of turbulence generation is that fluid cannot tolerate high shear stress and vorticity must transfer to rotation when Reynolds number is large enough.

4) The vorticity is large near the wall surface where the shear is dominant. The role of linear unstable modes is to push the vorticity up from the wall (rollup). When leaving away from the wall, the streamwise vortex legs and spanwise vortex rings will form due to the trend from shear to rotation. The rotation is a stable state with minimized dissipation (deformation is very small).

5) There is no such a process that the Λ-vortex self-deforms to hairpin vortex. The Λ-vortex root and ring head are formed separately by different mechanisms and ring is not part of Λ-vortex which is a pair of open rotation cores and is not a vortex tube.

6) A momentum deficit zone (low speed zone) is formed above the Λ-vortex and further generates a high shear due to the vortex root ejection. The vortex rings are generated by the high shear layer (K-H type) instability.

7) The second level vortices are generated by second level shear layer which is caused by first level vortex rings through sweeps, ejections, positive and negative spikes.

8) Multiple vortex rings are all formed by shear layer instability which is generated by momentum deficit.

9)The vortex structure is quite stable. The hairpin vortex is confirmed by both DNS [52] of Liu's team and experiment with a fine resolution of 1 μm of Cai's team [50].

10) All small vortices are generated by shear layer instability without exception. In other words, "shear layer instability is the mother of turbulence." There is no way that small vortices (turbulence) are generated by "large vortex breakdown".

11) The multiple level shear layers are generated by vortex sweeps and ejections. The sweep brings high-speed flow down (positive spike) to the lower boundary layer and the ejection brings the low-speed flow up (negative spike) to the upper boundary layer (momentum deficit). They form the multiple level shear layers and multiple vortex rings.

12) The energy transport channel is that the high energy is brought down to the lower boundary layer by multiple level sweeps. Without these sweeps, all small vortices (turbulence) would be dissipated quickly. Large vortex cannot pass energy to smaller vortices through “vortex breakdown” which was never observed by any experiment or DNS.

13) The disordering of flow structure is mainly not caused by the background noise or non-symmetric spanwise boundary conditions, but internal property of the multiple level vortex structure. The non-symmetry starts in the middle of the vortex packages.

14) Richardson eddy cascade revisit: it is not found.

15) Kolmogorov hypothesis revisit: there is no proof that large vortex passes energy to small vortices through vortex breakdown.

16) Turbulence bursting and intermittency: the term is generated by misunderstanding of turbulence package self-motion and relative motion. Turbulence cannot suddenly burst and suddenly disappear.

Based on Liu’s new theory, this dissertation (1) gives some mathematical explanations for new vortex identify method – Ω method; (2) analyzes the instability of shear layer by applying Chebyshev spectrum method to solve Orr-Sommerfeld eigenvalue equation; (3) investigates the vortex structure development in late flow transition; (4) utilizes the proper orthogonal decomposition to find the principal components of the flow in late stage of transition because of the flow complexity caused by hairpin vortex packet intertwining and interacting with each other.

Chapter 2

Governing Equation System and Numerical Methods

In this chapter, the governing equation system and numerical methods will be introduced in the following order: the dimensionless Navier-Stokes system and a form in curvilinear coordinates will be shown in section 2.1. The numerical methods in spatial and time discretization and boundary conditions will be given in section 2.2. Section 2.3 will give the set-up of DNS case and the code validation will be shown in section 2.4.

2.1 Governing Equation System

The flow field is governed by the Navier-Stokes system which is

$$\frac{\partial \boldsymbol{Q}}{\partial t}+\frac{\partial \boldsymbol{F}}{\partial x}+\frac{\partial \boldsymbol{G}}{\partial y}+\frac{\partial \boldsymbol{H}}{\partial z}=\frac{1}{Re}\left(\frac{\partial \boldsymbol{F_v}}{\partial x}+\frac{\partial \boldsymbol{G}_v}{\partial y}+\frac{\partial \boldsymbol{H}_v}{\partial z}\right) \tag{2-1}$$

Where the vector of conserved quantities $\boldsymbol{Q}$, inviscid flux vector $\boldsymbol{E}, \boldsymbol{F}$ and $\boldsymbol{G}$, and viscous flux vector $\boldsymbol{E}_v, \boldsymbol{F}_v$ and $\boldsymbol{G}_v$ are

$$\boldsymbol{Q}=\begin{pmatrix}\rho\\ \rho u\\ \rho v\\ \rho w\\ e\end{pmatrix},\ \boldsymbol{F}=\begin{pmatrix}\rho u\\ \rho u^2+p\\ \rho uv\\ \rho uw\\ (e+p)u\end{pmatrix},\ \boldsymbol{G}=\begin{pmatrix}\rho v\\ \rho uv\\ \rho v^2+p\\ \rho vw\\ (e+p)v\end{pmatrix},\ \boldsymbol{H}=\begin{pmatrix}\rho w\\ \rho uw\\ \rho vw\\ \rho w^2+p\\ (e+p)w\end{pmatrix} \tag{2-2}$$

$$\boldsymbol{F}_v=\begin{pmatrix}0\\ \sigma_{xx}\\ \sigma_{xy}\\ \sigma_{xz}\\ u\sigma_{xx}+v\sigma_{xy}+w\sigma_{xz}+\dfrac{1}{(\gamma-1)PrM_\infty^2}k(T)\dfrac{\partial T}{\partial x}\end{pmatrix} \tag{2-3}$$

$$\boldsymbol{G}_v=\begin{pmatrix}0\\ \sigma_{xy}\\ \sigma_{yy}\\ \sigma_{yz}\\ u\sigma_{xy}+v\sigma_{yy}+w\sigma_{yz}+\dfrac{1}{(\gamma-1)PrM_\infty^2}k(T)\dfrac{\partial T}{\partial y}\end{pmatrix} \tag{2-4}$$

$$\boldsymbol{H}_v = \begin{pmatrix} 0 \\ \sigma_{xz} \\ \sigma_{yz} \\ \sigma_{zz} \\ (u\sigma_{xz} + v\sigma_{yz} + w\sigma_{zz} + \dfrac{1}{(\gamma-1)PrM_\infty^2} k(T)\dfrac{\partial T}{\partial z} \end{pmatrix} \tag{2-5}$$

The components of viscous stress are

$$\sigma_{xx} = \frac{2}{3}\mu(T)\left(2\frac{\partial u}{\partial x} - \frac{\partial v}{\partial y} - \frac{\partial w}{\partial z}\right) \tag{2-6}$$

$$\sigma_{yy} = \frac{2}{3}\mu(T)\left(-\frac{\partial u}{\partial x} + 2\frac{\partial v}{\partial y} - \frac{\partial w}{\partial z}\right) \tag{2-7}$$

$$\sigma_{xx} = \frac{2}{3}\mu(T)\left(-\frac{\partial u}{\partial x} - \frac{\partial v}{\partial y} + 2\frac{\partial w}{\partial z}\right) \tag{2-8}$$

$$\sigma_{xy} = \mu(T)\left(\frac{\partial u}{\partial y} + \frac{\partial v}{\partial x}\right) \tag{2-9}$$

$$\sigma_{xz} = \mu(T)\left(\frac{\partial u}{\partial z} + \frac{\partial w}{\partial x}\right) \tag{2-10}$$

$$\sigma_{yz} = \mu(T)\left(\frac{\partial w}{\partial y} + \frac{\partial v}{\partial z}\right) \tag{2-11}$$

We can write the governing equations in curvilinear coordinates as

$$\frac{\partial \widehat{\boldsymbol{Q}}}{\partial t} + \frac{\partial \widehat{\boldsymbol{F}}}{\partial \xi} + \frac{\partial \widehat{\boldsymbol{G}}}{\partial \eta} + \frac{\partial \widehat{\boldsymbol{H}}}{\partial \zeta} = \frac{1}{Re}\left(\frac{\partial \widehat{\boldsymbol{F}}_v}{\partial \xi} + \frac{\partial \widehat{\boldsymbol{G}}_v}{\partial \eta} + \frac{\partial \widehat{\boldsymbol{H}}_v}{\partial \zeta}\right) \tag{2-12}$$

where

$$\widehat{\boldsymbol{Q}} = \frac{\boldsymbol{Q}}{J}, \tag{2-13}$$

$$\widehat{\boldsymbol{F}} = \frac{\xi_x \boldsymbol{F} + \xi_y \boldsymbol{G} + \xi_z \boldsymbol{H}}{J}, \tag{2-14}$$

$$\widehat{\boldsymbol{G}} = \frac{\eta_x \boldsymbol{F} + \eta_y \boldsymbol{G} + \eta_z \boldsymbol{H}}{J}, \tag{2-15}$$

$$\widehat{\boldsymbol{H}} = \frac{\zeta_x \boldsymbol{F} + \zeta_y \boldsymbol{G} + \zeta_z \boldsymbol{H}}{J}, \tag{2-16}$$

$$\widehat{\boldsymbol{F}}_v = \frac{\xi_x \boldsymbol{F}_v + \xi_y \boldsymbol{G}_v + \xi_z \boldsymbol{H}_v}{J}\,, \tag{2-17}$$

$$\widehat{\boldsymbol{G}}_v = \frac{\eta_x \boldsymbol{F}_v + \eta_y \boldsymbol{G}_v + \eta_z \boldsymbol{H}_v}{J}\,, \tag{2-18}$$

$$\widehat{\boldsymbol{H}}_v = \frac{\zeta_x \boldsymbol{F}_v + \zeta_y \boldsymbol{G}_v + \zeta_z \boldsymbol{H}_v}{J}\,, \tag{2-19}$$

The Jacobian J of the coordinate transformation between the curvilinear (ξ, η, ζ) and Cartesian (x, y, z) frames is

$$J = \frac{1}{\begin{vmatrix} 1 & 0 & 0 & 0 \\ 0 & x_\xi & x_\eta & x_\zeta \\ 0 & y_\xi & y_\eta & y_\zeta \\ 0 & z_\xi & y_\eta & z_\zeta \end{vmatrix}}\,, \tag{2-20}$$

and

$$\begin{pmatrix} \xi_x & \xi_y & \xi_z \\ \eta_x & \eta_y & \eta_z \\ \zeta_x & \zeta_y & \zeta_z \end{pmatrix} = J \begin{pmatrix} y_\eta z_\zeta - y_\zeta z_\eta & z_\eta x_\zeta - z_\zeta x_\eta & x_\eta y_\zeta - x_\zeta y_\eta \\ y_\zeta z_\xi - y_\xi z_\zeta & z_\zeta x_\xi - z_\xi x_\zeta & x_\zeta y_\xi - x_\xi y_\zeta \\ y_\xi z_\eta - y_\eta z_\zeta & z_\xi x_\eta - z_\eta x_\zeta & x_\xi y_\eta - x_\eta y_\zeta \end{pmatrix}. \tag{2-21}$$

The reference values for length, density, velocity, temperature and pressure are $\delta_{in}, \rho_\infty, U_\infty, T_\infty$ and $\rho_\infty U_\infty^2$ respectively, where δ_{in} is the inflow displacement thickness. And the Mach number M_∞ and Reynolds number Re are expressed as

$$M_\infty = \frac{U_\infty}{\sqrt{\gamma R T_\infty}}\,, \qquad Re = \frac{\rho_\infty U_\infty \delta_{in}}{\mu_\infty}\,, \tag{2-22}$$

where R is the ideal gas constant, γ the ratio of specific heats and μ_∞ the viscosity.

2.2 Numerical Methods

Compact scheme has an implicit form and involves the derivative of neighboring grid point, which results in additional free parameters. These free parameters can be used to improve the accuracy and optimize other properties such as resolution, stability, and conservation. It also has been proved to have spectral-like resolution, and can

achieve higher order without increasing the stencil width which are necessary for studying instability problem by direct numerical simulation.

A sixth order compact scheme [53] is used for the spatial discretization in the streamwise and wall normal directions. For internal points $j = 3, \dots, N-2$, the sixth order compact scheme is

$$\frac{1}{3}f'_{j-1} + f'_j + \frac{1}{3}f'_{j+1} = \frac{1}{h}\left(-\frac{1}{36}f_{j-2} - \frac{7}{9}f_{j-1} + \frac{7}{9}f_{j+1} + \frac{1}{36}f_{j+2}\right), \tag{2-23}$$

where f'_j is the derivative at point j. The fourth order compact scheme is used at points $j = 2$ and $j = N-1$, and the third order one-sided compact scheme is used at the boundary points $j = 1$ and $j = N$.

In the spanwise direction where periodical conditions are applied, the pseudo-spectral method is used. To eliminate the spurious numerical oscillations caused by central difference schemes, a high-order spatial scheme is used instead of artificial dissipation. An implicit sixth-order compact scheme for space filtering is applied to the primitive variables u, v, w, ρ and p after a specified number of time steps.

In time marching, a third order TVD Runge-Kutta scheme [54] is adopted:

$$\begin{aligned} Q^{(0)} &= Q^{(n)}, \\ Q^{(1)} &= Q^{(0)} + \Delta t R^{(0)}, \\ Q^{(2)} &= \frac{3}{4}Q^{(0)} + \frac{1}{4}Q^{(1)} + \frac{1}{4}\Delta t R^{(1)}, \\ Q^{(n+1)} &= \frac{1}{3}Q^{(0)} + \frac{2}{3}Q^{(2)} + \frac{2}{3}\Delta t R^{2}. \end{aligned} \tag{2-24}$$

The adiabatic and the non-slipping conditions are enforced at the wall boundary on the flat plate. On the far field and the outflow boundaries, the non-reflecting boundary conditions [55] are applied. The inflow is given in the form of

$$q = q_{lam} + A_{2d}q'_{2d}e^{i(\alpha x - \omega t)} + A_{3d}q'_{3d}e^{i(\alpha x \pm \beta y - \omega t)}, \tag{2-25}$$

where q represents u, v, w, p and T, and q_{lam} represents the Blasius solution for a two-dimensional laminar boundary layer. The T-S wave parameters are obtained by solving the compressible boundary layer stability equations [56]. The streamwise wavenumber, spanwise wavenumber, frequency and amplitude are listed in Table 2-1.

Table 2-1 Parameters for inflow condition

α	β	ω	A_{2d}	A_{3d}
$0.29919 - i5.0958 \times 10^{-3}$	± 0.5712	0.114027	0.03	0.01

2.3 Case Setup

The physical domain is displayed in Figure 2-1, where x_{in} represents the distance between leading edge and inlet, Lx and Ly are the lengths of the computational domain in x and y directions respectively, and Lz_{in} is the length of the inlet in z direction. The details are listed in Table 2-2. The grid level is $1920 \times 128 \times 241$, representing the number of grids in streamwise (x), spanwise (y), and wall normal (z) directions. The grid is stretched in the normal direction and uniform in the streamwise and spanwise directions. The length of the first grid interval in the normal direction at the entrance is found to be 0.43 in wall units ($Z^+ = 0.43$).

The Jacobian coordinate transformation is employed from physical domain to computational domain, see Figure 2-2(a) and the Message Passing Interface (MPI), together with domain decomposition in the ξ-direction, is utilized to accomplish the parallel computation, see Figure 2-2(b). The flow parameters, including Mach number, Reynolds number, etc. are listed in Table 2-3. Here, $T_w = 273.15K$ is the wall temperature.

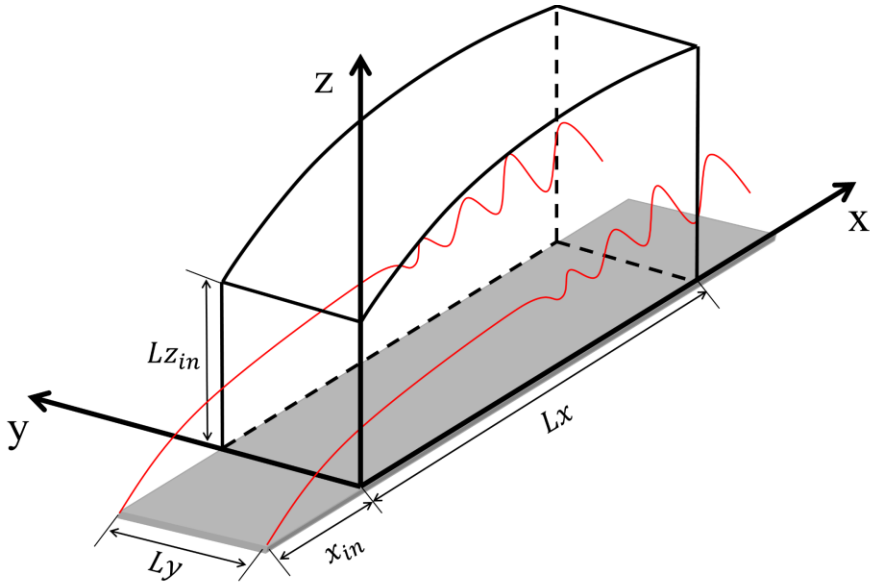

Figure 2-1 Physical domain

Table 2-2 Geometry parameters

x_{in}	Lx	Ly	Lz_{in}
$300.79\delta_{in}$	$798.03\delta_{in}$	$22\delta_{in}$	$40\delta_{in}$

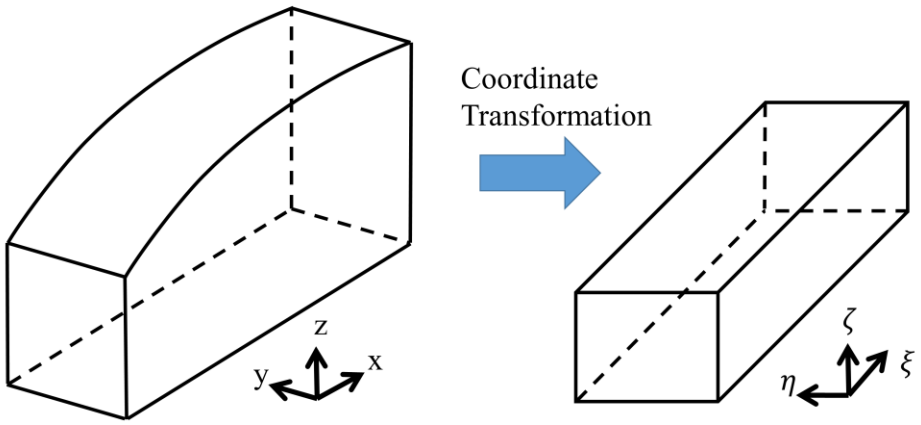

(a)

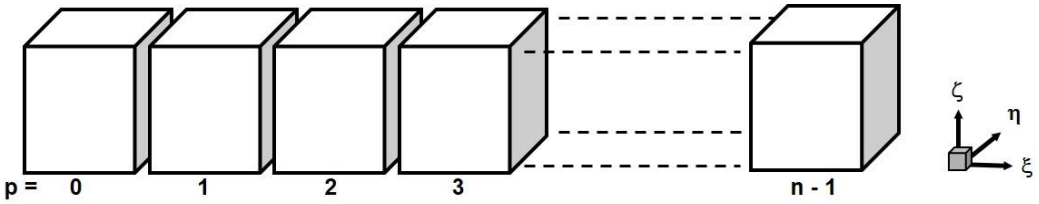

(b)

Figure 2-2 Schematics of (a) coordinate transformation and (b) domain decomposition.

Table 2-3 Flow paramaters

M_∞	Re	T_w	T_∞
0.5	1000	273.15K	273.15K

2.4 Code validation

The DNS code – ‘‘DNSUTA’’ has been validated by NASA Langley and UTA researchers [57]–[59] carefully to make sure that the DNS results are correct. Since the detailed code validation has been reported by Liu and Chen [60] we only give a short description here.

2.4.1 Comparison with Log Law and grid convergence

Time and spanwise-averaged streamwise velocity profiles for various streamwise locations in two different grid levels are shown in Figure 2-3. The inflow velocity profiles at $x = 300.79\delta_{in}$ is a typical laminar flow velocity profile. At $x = 632.33\delta_{in}$, the mean velocity profile approaches a turbulent flow velocity profile (Log law). This comparison shows that the velocity profile from the DNS results is turbulent flow velocity profile and the grid convergence has been realized.

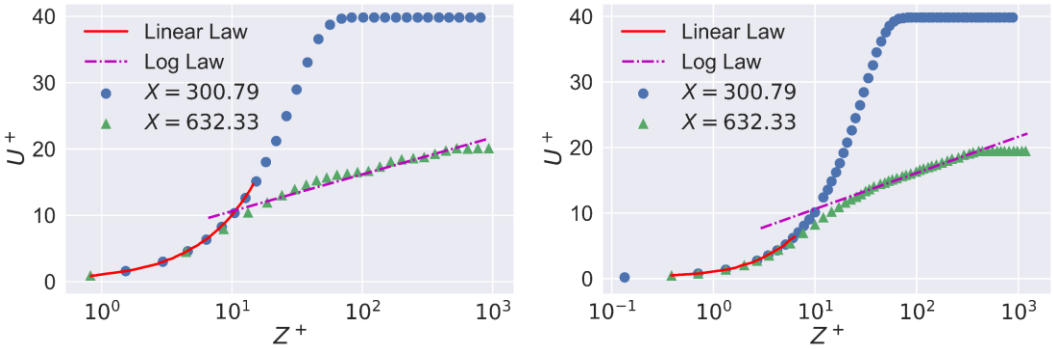

(a) Coarse Grids (960x64x121) (b) Fine Grids (1920x128x241)

Figure 2-3 Log-linear plots of the time-and spanwise-averaged velocity profile in wall unit

2.4.2 Comparison with experiment

By using Ω criterion method, the vortex structures shaped by the nonlinear evolution of T-S waves in the transition process are shown in Figure 2-4. The formation of ring-like vortices chains is consistent with the experimental work, see Figure 2-5.

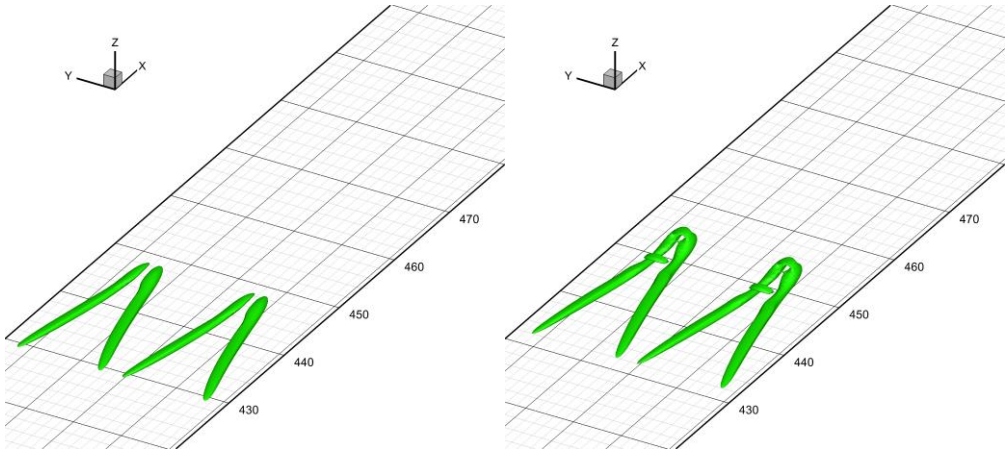

(a) t=6.0T (b) t=6.2T

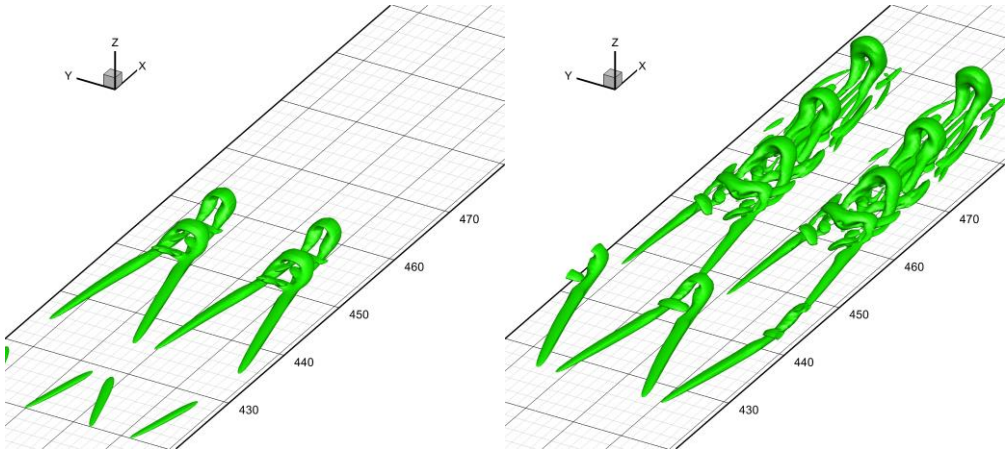

(c) t=6.4T (d) t=7.0T

Figure 2-4 Evolution of vortex structure at the late-stage of transition (Where T is the period of T-S wave)

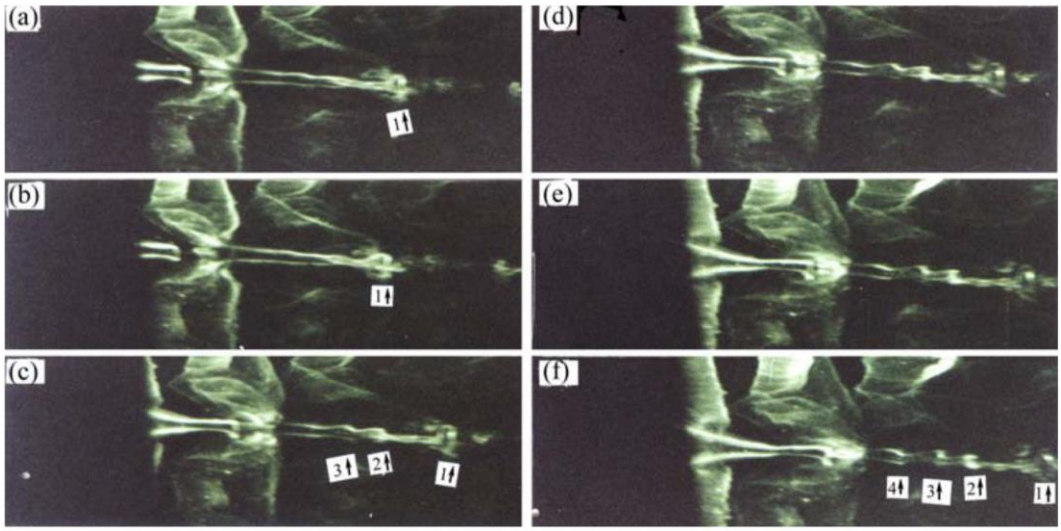

Figure 2-5 Evolution of the ring-like vortex chain by experiment [61].

2.4.3 Comparison with Rist's DNS data

Figure 2-6 shows a comparison of our DNS results with the data set provided by Rist as his personal kindness. The comparison shows both DNS have same vortex structure.

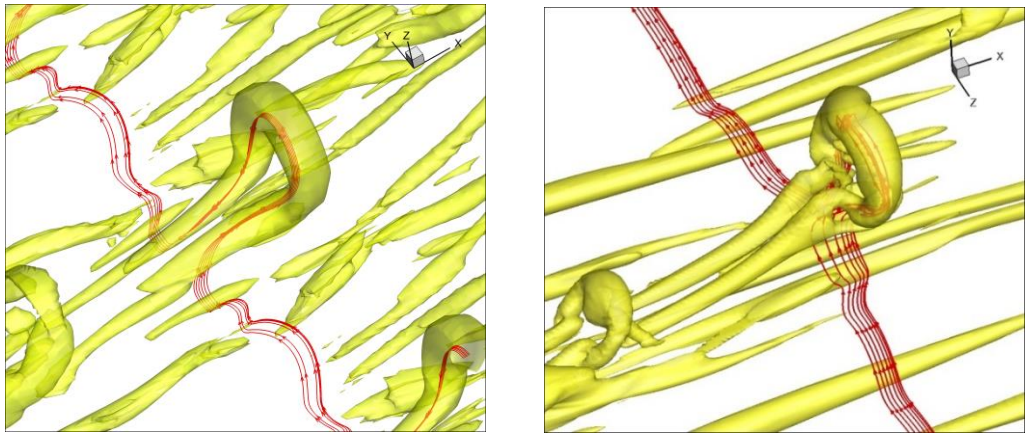

(a) Our DNS (b) Rist's DNS data

Figure 2-6 Comparison of our DNS results with Rist's DNS data.

All these verifications and validations above show that our code is correct and our DNS results are reliable.

2.5 Summary

In this chapter, the governing equation system and numerical methods are introduced. A database is set up via direct numerical simulation for Navier-Stokes system. It is on the grid with dimensions $1920 \times 128 \times 241$ in almost $20T$, where T is TS wave period. Based on this database, the vortical structures analyses are carried out.

Chapter 3

Tensor Analysis and Ω Vortex Identification Method

In this chapter, an analysis on the tensor field $\nabla \boldsymbol{V}$ will be shown in section 3.1 and section 3.2 will revisit the new vortex identification method, Ω-method. In section 3.3, some mathematical explanations for Ω-method will be given.

3.1 Analysis on the tensor field $\nabla \boldsymbol{V}$

In this section, we will study the transformations of an infinitesimal body fluid $\delta\mathcal{V}$ during its motion in an incompressible flow, over an infinitesimal time period. The local analysis in this section is based on the tensor field $\nabla \boldsymbol{V}$ defined by

$$\nabla \boldsymbol{V} = \begin{pmatrix} \frac{\partial u}{\partial x} & \frac{\partial u}{\partial y} & \frac{\partial u}{\partial z} \\ \frac{\partial v}{\partial x} & \frac{\partial v}{\partial y} & \frac{\partial v}{\partial z} \\ \frac{\partial w}{\partial x} & \frac{\partial w}{\partial y} & \frac{\partial w}{\partial z} \end{pmatrix}. \tag{3-1}$$

$\nabla \boldsymbol{V}$ governs the first-order transformations of $\delta\mathcal{V}$ over an infinitesimal time δT.

What is the role of $\nabla \boldsymbol{V}$?

Suppose $\boldsymbol{x}$ is the gravity center of δV at time t_0 and $\boldsymbol{y} \in \delta\mathcal{V}$ is any other point. Let $\boldsymbol{x}(t)$ and $\boldsymbol{y}(t)$ denote the position of two particles sitting on $\boldsymbol{x}$ and $\boldsymbol{y}$ at time t_0. Define $\boldsymbol{\xi}(t) = \boldsymbol{y}(t) - \boldsymbol{x}(t)$. Assume that the particles move to $\boldsymbol{x} + \delta\boldsymbol{x}$ and $\boldsymbol{y} + \delta\boldsymbol{y}$ respectively at time $t + \delta t$ for some $\delta t > 0$. Then the change of $\boldsymbol{\xi}$ will be $\delta\boldsymbol{\xi} = \delta\boldsymbol{y} - \delta\boldsymbol{x}$. By performing the asymptotic expansions, we have

$$\delta\boldsymbol{x} = \boldsymbol{V}(t, \boldsymbol{x})\delta t + o(\delta t)\,, \tag{3-2}$$

$$\delta\boldsymbol{y} = \boldsymbol{V}(t, \boldsymbol{y})\delta t + o(\delta t)\,, \tag{3-3}$$

$$\boldsymbol{V}(t, \boldsymbol{y}) - \boldsymbol{V}(t, \boldsymbol{x}) = \nabla \boldsymbol{V}(t, \boldsymbol{x}) \cdot \boldsymbol{\xi} + o(\|\boldsymbol{\xi}\|)\,. \tag{3-4}$$

Combining these Equation (3-2)-(3-4) yields

$$\frac{\delta \boldsymbol{\xi}}{\delta t} = \nabla \boldsymbol{V}(t, \boldsymbol{x}) \cdot \boldsymbol{\xi} + o(\delta t + \|\boldsymbol{\xi}\|) . \tag{3-5}$$

Then we take the limit of $\frac{\delta \xi}{\delta t}$ as $\delta t \to 0$, which yields the following differential equation:

$$\boldsymbol{\xi}' = \nabla \boldsymbol{V}(t, \boldsymbol{x}) \cdot \boldsymbol{\xi} + o(\|\boldsymbol{\xi}\|) . \tag{3-6}$$

This suggests the following local ODE, which corresponds to the first-order term in above equation,

$$\boldsymbol{\xi}' = \nabla \boldsymbol{V}(t, \boldsymbol{x}) \cdot \boldsymbol{\xi} . \tag{3-7}$$

However, without any specific information about the matrix $\nabla \boldsymbol{V}(t, \boldsymbol{x})$ it is difficult to picture the overall appearance of the solutions. Then we write $\nabla \boldsymbol{V} = \mathbf{A} + \mathbf{B}$, where $\boldsymbol{A} = \frac{1}{2}(\nabla \boldsymbol{V} + \nabla \boldsymbol{V}^{\boldsymbol{t}})$ is the symmetric part of $\nabla \boldsymbol{V}$ and $\mathbf{B} = \frac{1}{2}(\nabla \boldsymbol{V} - \nabla \boldsymbol{V}^{\boldsymbol{t}})$ is the antisymmetric part of $\nabla \boldsymbol{V}$. $\boldsymbol{A}$ is also called deformation tensor.

Next we study the effect of $\boldsymbol{A}$ and $\boldsymbol{B}$ on $\boldsymbol{\xi}$ separately through two special conditions:

1) $\boldsymbol{B} = \mathbf{0}$, then $\boldsymbol{\xi}' = \boldsymbol{A} \cdot \boldsymbol{\xi}$.

Write $\boldsymbol{A}$ in the matrix form

$$\boldsymbol{A} = \begin{pmatrix} \frac{\partial u}{\partial x} & \frac{1}{2}\left(\frac{\partial u}{\partial y} + \frac{\partial v}{\partial x}\right) & \frac{1}{2}\left(\frac{\partial w}{\partial x} + \frac{\partial u}{\partial z}\right) \\ \frac{1}{2}\left(\frac{\partial u}{\partial y} + \frac{\partial v}{\partial x}\right) & \frac{\partial v}{\partial y} & \frac{1}{2}\left(\frac{\partial v}{\partial z} + \frac{\partial w}{\partial y}\right) \\ \frac{1}{2}\left(\frac{\partial w}{\partial x} + \frac{\partial u}{\partial z}\right) & \frac{1}{2}\left(\frac{\partial v}{\partial z} + \frac{\partial w}{\partial y}\right) & \frac{\partial w}{\partial z} \end{pmatrix} . \tag{3-8}$$

We take the inner product by $\boldsymbol{\xi}$ with both side of

$$\boldsymbol{\xi}' = \boldsymbol{A} \cdot \boldsymbol{\xi} , \tag{3-9}$$

which yields

$$(\boldsymbol{\xi}', \boldsymbol{\xi}) = (\boldsymbol{A} \cdot \boldsymbol{\xi}, \boldsymbol{\xi}) . \tag{3-10}$$

Therefore,

$$\frac{1}{2}\frac{d\|\boldsymbol{\xi}\|^2}{dt} = (\boldsymbol{A} \cdot \boldsymbol{\xi}, \boldsymbol{\xi}) . \tag{3-11}$$

Since $\boldsymbol{A}$ is symmetric, all eigenvalue of $\boldsymbol{A}$ are real, say $\lambda_1,\ \lambda_2,\ \lambda_3$. Notice that $\sum_{i=1}^{3} \lambda_i = tr(\boldsymbol{A}) = \frac{\partial u}{\partial x} + \frac{\partial v}{\partial y} + \frac{\partial w}{\partial z} = 0$. So assume first that $\boldsymbol{A} = 0$, then the velocity is locally constant around $\boldsymbol{x}$ and particles move along straight lines.

Assume next that $\boldsymbol{A} \neq 0$, then $\boldsymbol{A}$ has at least one strictly negative eigenvalue, say λ_1, and one strictly positive, say λ_2. In particular, let $\boldsymbol{\xi}$ be an initial vector that is an eigenvector associated with λ_1, then $\boldsymbol{\xi}$ goes to be shorter; let $\boldsymbol{\xi}$ be an initial vector that is an eigenvector associated with λ_2, then $\boldsymbol{\xi}$ goes to be longer.

2) $\boldsymbol{A} = \boldsymbol{0}$, then $\boldsymbol{\xi}' = \boldsymbol{B} \cdot \boldsymbol{\xi}$.

Write $\boldsymbol{B}$ in the matrix form

$$\boldsymbol{B} = \begin{pmatrix} 0 & -\frac{1}{2}\left(\frac{\partial v}{\partial x} - \frac{\partial u}{\partial y}\right) & \frac{1}{2}\left(\frac{\partial u}{\partial z} - \frac{\partial w}{\partial x}\right) \\ \frac{1}{2}\left(\frac{\partial v}{\partial x} - \frac{\partial u}{\partial y}\right) & 0 & -\frac{1}{2}\left(\frac{\partial \mathrm{w}}{\partial y} - \frac{\partial v}{\partial z}\right) \\ -\frac{1}{2}\left(\frac{\partial u}{\partial z} - \frac{\partial w}{\partial x}\right) & \frac{1}{2}\left(\frac{\partial w}{\partial y} - \frac{\partial v}{\partial z}\right) & 0 \end{pmatrix} . \tag{3-12}$$

Notice that the vorticity $\boldsymbol{\omega} = \nabla \times \boldsymbol{V}$, then it is easily found that

$$\boldsymbol{B} = \frac{1}{2}\begin{pmatrix} 0 & -\omega_z & \omega_y \\ \omega_z & 0 & -\omega_x \\ -\omega_y & \omega_x & 0 \end{pmatrix} , \tag{3-13}$$

where ω_x, ω_y and ω_z are three components of $\boldsymbol{\omega}$.

Then it can be shown that $\boldsymbol{B} \cdot \boldsymbol{\xi} = \frac{1}{2}\boldsymbol{\omega} \times \boldsymbol{\xi}$. By plugging in, we have

$$\boldsymbol{\xi}' = \frac{1}{2}\boldsymbol{\omega} \times \boldsymbol{\xi} . \tag{3-14}$$

If $\boldsymbol{\omega} = 0$, then $\boldsymbol{\xi}$ will keep unchanged. Let us assume that $\boldsymbol{\omega} \neq 0$ and consider $\boldsymbol{e_1} = \frac{\boldsymbol{\omega}}{\|\boldsymbol{\omega}\|}$. Let $\boldsymbol{e_2}$ and $\boldsymbol{e_3}$ be such that $(\boldsymbol{e_1}, \boldsymbol{e_2}, \boldsymbol{e_3})$ is an orthogonal basis of $\mathbb{R}^3$ that in particularly satisfies

$$\begin{aligned} \boldsymbol{e_1} \times \boldsymbol{e_2} &= \boldsymbol{e_3}\,, \\ \boldsymbol{e_2} \times \boldsymbol{e_3} &= \boldsymbol{e_1}\,, \\ \boldsymbol{e_3} \times \boldsymbol{e_1} &= \boldsymbol{e_2}\,, \end{aligned} \tag{3-15}$$

We write $\boldsymbol{\xi} = \xi_1 \boldsymbol{e_1} + \xi_2 \boldsymbol{e_2} + \xi_3 \boldsymbol{e_3}$. Setting $z = \xi_2 + i\xi_3$, we get

$$\xi_1' = 0, \quad z' = i\frac{\|\boldsymbol{\omega}\|}{2} z\,, \tag{3-16}$$

which yields

$$\xi_1(t) = \xi_1(0), \;\; z(t) = e^{i\frac{\|\boldsymbol{\omega}\|}{2}t} z(0)\,. \tag{3-17}$$

Therefore, trajectories rotate around the axis spanned by $\boldsymbol{\omega}$ with a frequency equal to $\|\boldsymbol{\omega}\|/2$.

When both $\boldsymbol{A}$ and $\boldsymbol{B}$ are nonzero, the infinitesimal body fluid $\delta\mathcal{V}$ has deformation as well as vorticity. To reveal the relation between $\boldsymbol{A}$, $\boldsymbol{B}$ and vortices, A new vortex identification method is proposed in next section.

3.2 Ω Vortex Identification Method

A new vortex identification method is proposed by Liu et al. [51], called Ω-method.

The new parameter is defined as

$$\Omega = \frac{\|\boldsymbol{B}\|_F^2}{\|\boldsymbol{A}\|_F^2 + \|\boldsymbol{B}\|_F^2}\,, \tag{3-18}$$

provided $\nabla \boldsymbol{V} \neq \mathbf{0}$, where $\| \cdot \|_F$ is the Frobenius norm. In the case of $\nabla \boldsymbol{V} = \mathbf{0}$, Ω is defined as a constant 0.5. A vortex is identified as the region where $\Omega > 0.5$, which means vorticity overtakes deformation.

We will evaluate this identification by several exact solutions and DNS data.

1) At a wall

The most general velocity gradient at the wall is given by

$$\nabla \boldsymbol{V} = \begin{pmatrix} 0 & 0 & a \\ 0 & 0 & b \\ 0 & 0 & 0 \end{pmatrix}. \tag{3-19}$$

Then symmetric components $\boldsymbol{A}$ and antisymmetric components $\boldsymbol{B}$ of $\nabla \boldsymbol{V}$ are

$$\boldsymbol{A} = \begin{pmatrix} 0 & 0 & \frac{a}{2} \\ 0 & 0 & \frac{b}{2} \\ \frac{a}{2} & \frac{b}{2} & 0 \end{pmatrix}, \qquad \boldsymbol{B} = \begin{pmatrix} 0 & 0 & \frac{a}{2} \\ 0 & 0 & \frac{b}{2} \\ -\frac{a}{2} & -\frac{b}{2} & 0 \end{pmatrix}, \tag{3-20}$$

which gives $\|\boldsymbol{A}\|_F^2 = \frac{1}{2}(a^2 + b^2)$ and $\|\boldsymbol{B}\|_F^2 = \frac{1}{2}(a^2 + b^2)$, hence $\Omega = 0.5$.

2) Blasius boundary layer

The velocity gradient in Blasius boundary layer is given by

$$\nabla \boldsymbol{V} = \begin{pmatrix} 0 & 0 & a \\ 0 & 0 & 0 \\ 0 & 0 & 0 \end{pmatrix}. \tag{3-21}$$

Then symmetric components $\boldsymbol{A}$ and antisymmetric components $\boldsymbol{B}$ of $\nabla \boldsymbol{V}$ are

$$\boldsymbol{A} = \begin{pmatrix} 0 & 0 & \frac{a}{2} \\ 0 & 0 & 0 \\ \frac{a}{2} & 0 & 0 \end{pmatrix}, \qquad \boldsymbol{B} = \begin{pmatrix} 0 & 0 & \frac{a}{2} \\ 0 & 0 & 0 \\ -\frac{a}{2} & 0 & 0 \end{pmatrix}, \tag{3-22}$$

which gives $\|\boldsymbol{A}\|_F^2 = \frac{a^2}{2}$ and $\|\boldsymbol{B}\|_F^2 = \frac{a^2}{2}$, hence $\Omega = 0.5$.

3) Pure rotation

We consider here a spanwise pure rotation with angular velocity Φ, see Figure 3-1. The velocity gradient in this flow is

$$\nabla \boldsymbol{V} = \begin{pmatrix} 0 & 0 & \Phi \\ 0 & 0 & 0 \\ -\Phi & 0 & 0 \end{pmatrix}. \tag{3-23}$$

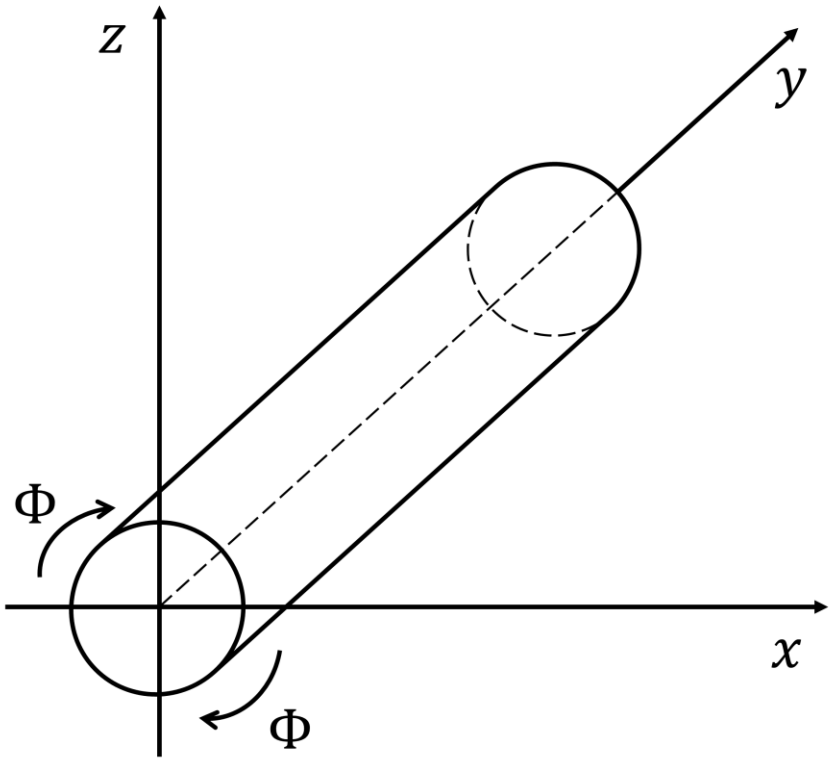

Figure 3-1 A spanwise pure rotation with angular velocity Φ.

Then symmetric components $\boldsymbol{A}$ and antisymmetric components $\boldsymbol{B}$ of $\nabla \boldsymbol{V}$ are

$$\boldsymbol{A} = \begin{pmatrix} 0 & 0 & 0 \\ 0 & 0 & 0 \\ 0 & 0 & 0 \end{pmatrix}, \qquad \boldsymbol{B} = \begin{pmatrix} 0 & 0 & \Phi \\ 0 & 0 & 0 \\ -\Phi & 0 & 0 \end{pmatrix}, \tag{3-24}$$

which gives $\|\boldsymbol{A}\|_F^2 = 0$ and $\|\boldsymbol{B}\|_F^2 = 2\Phi^2$, hence $\Omega = 1$.

4) Pure shear

We then consider a pure shear with $u = az$, $v = 0$ and $w = ax$, where a is a constant, see Figure 3-2. The velocity gradient in this flow is

$$\nabla \boldsymbol{V} = \begin{pmatrix} 0 & 0 & a \\ 0 & 0 & 0 \\ a & 0 & 0 \end{pmatrix}. \tag{3-25}$$

Then symmetric components $\boldsymbol{A}$ and antisymmetric components $\boldsymbol{B}$ of $\nabla \boldsymbol{V}$ are

$$\boldsymbol{A} = \begin{pmatrix} 0 & 0 & a \\ 0 & 0 & 0 \\ a & 0 & 0 \end{pmatrix}, \tag{3-26}$$

$$\boldsymbol{B} = \begin{pmatrix} 0 & 0 & 0 \\ 0 & 0 & 0 \\ 0 & 0 & 0 \end{pmatrix}, \tag{3-27}$$

which gives $\|\boldsymbol{A}\|_F^2 = 2a^2$ and $\|\boldsymbol{B}\|_F^2 = 0$, hence $\Omega = 0$.

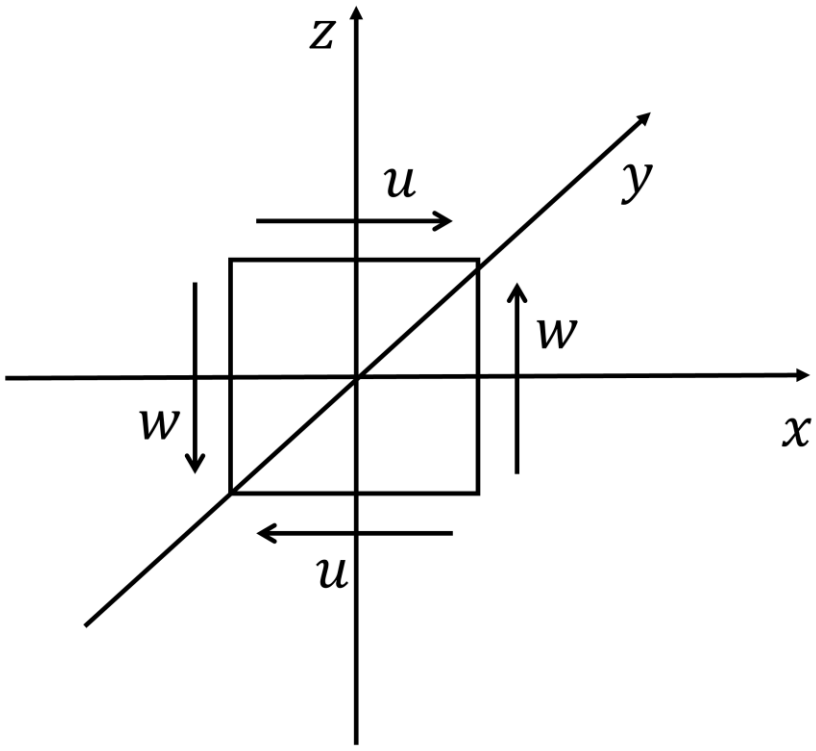

Figure 3-2 A pure shear with $u = az$, $v = 0$ and $w = ax$.

5) Transitional boundary layer flow over flat-plate

The case setup has been given in Chapter 2. Figure 3-3 gives the vortical structures at $t = 8.16T$, where T is the period of T-S wave, by Q-, λ_2- and Ω-criteria respectively. It shows that Ω-criteria identifies vortical structure clearly.

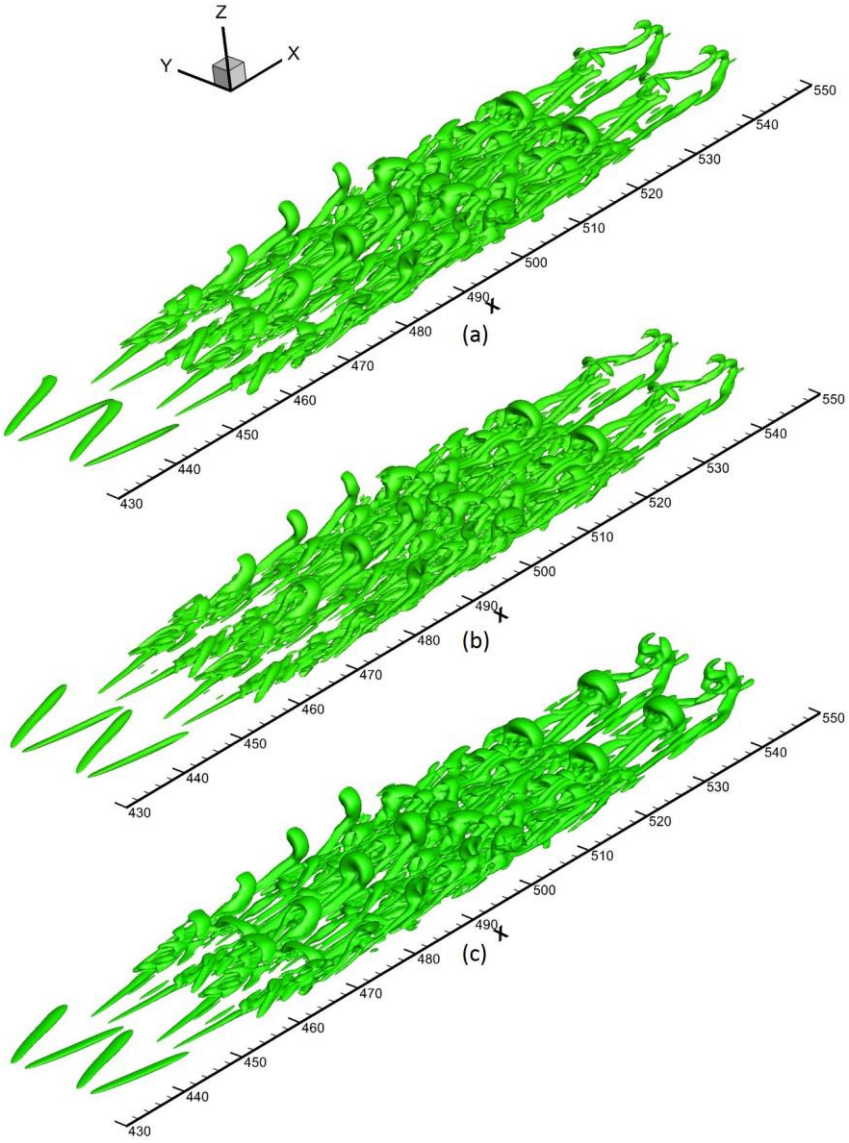

Figure 3-3 Iso-surface of (a) $Q = 0.005$ (b) $\lambda_2 = -0.005$ (c) $\Omega = 0.52$ at $t = 8.16T$, where T is the period of T-S wave.

In these five cases, the new definition of vortex are evaluated well. Vortices vanish at the wall ($\Omega = 0.5$), in the Blasius boundary layer ($\Omega = 0.5$) and in the pure shear flow ($\Omega = 0$), whereas vortices are identified in pure rotation flow ($\Omega = 1.0$) and in transition boundary layer flow over flat-plate.

Consequently, vortical structures can be identified by the iso-surface of $\Omega = 0.52$. This is a relatively unique threshold, comparing to Q- and λ_2-criteria which are both case-related [51].

3.3 Some Mathematical Explanations for Ω Vortex Identification Method

Recall Equation (3-8) and (3-12), we have

$$\begin{aligned}\|\boldsymbol{A}\|_F^2 &= \left(\frac{\partial u}{\partial x}\right)^2 + \left(\frac{\partial v}{\partial y}\right)^2 + \left(\frac{\partial w}{\partial z}\right)^2 + \frac{1}{2}\left(\frac{\partial u}{\partial y} + \frac{\partial v}{\partial x}\right)^2 + \frac{1}{2}\left(\frac{\partial u}{\partial z} + \frac{\partial w}{\partial x}\right)^2 + \frac{1}{2}\left(\frac{\partial v}{\partial z} + \frac{\partial w}{\partial y}\right)^2 \\ &= \left(\frac{\partial u}{\partial x}\right)^2 + \left(\frac{\partial v}{\partial y}\right)^2 + \left(\frac{\partial w}{\partial z}\right)^2 + \frac{1}{2}\left(\frac{\partial u}{\partial y}\right)^2 + \frac{1}{2}\left(\frac{\partial u}{\partial z}\right)^2 + \frac{1}{2}\left(\frac{\partial v}{\partial x}\right)^2 + \frac{1}{2}\left(\frac{\partial v}{\partial z}\right)^2 + \frac{1}{2}\left(\frac{\partial w}{\partial x}\right)^2 \\ &\quad + \frac{1}{2}\left(\frac{\partial w}{\partial y}\right)^2 + \frac{\partial u}{\partial y}\frac{\partial v}{\partial x} + \frac{\partial u}{\partial z}\frac{\partial w}{\partial x} + \frac{\partial v}{\partial z}\frac{\partial w}{\partial y}\end{aligned} \tag{3-28}$$

$$\begin{aligned}\|\boldsymbol{B}\|_F^2 &= \frac{1}{2}\left(\frac{\partial u}{\partial y} - \frac{\partial v}{\partial x}\right)^2 + \frac{1}{2}\left(\frac{\partial u}{\partial z} - \frac{\partial w}{\partial x}\right)^2 + \frac{1}{2}\left(\frac{\partial v}{\partial z} - \frac{\partial w}{\partial y}\right)^2 \\ &= \frac{1}{2}\left(\frac{\partial u}{\partial y}\right)^2 + \frac{1}{2}\left(\frac{\partial u}{\partial z}\right)^2 + \frac{1}{2}\left(\frac{\partial v}{\partial x}\right)^2 + \frac{1}{2}\left(\frac{\partial v}{\partial z}\right)^2 + \frac{1}{2}\left(\frac{\partial w}{\partial x}\right)^2 + \frac{1}{2}\left(\frac{\partial w}{\partial y}\right)^2 \\ &\quad - \frac{\partial u}{\partial y}\frac{\partial v}{\partial x} - \frac{\partial u}{\partial z}\frac{\partial w}{\partial x} - \frac{\partial v}{\partial z}\frac{\partial w}{\partial y}\end{aligned} \tag{3-29}$$

We can rewrite $\|\boldsymbol{A}\|_F^2$ as

$$\|\boldsymbol{A}\|_F^2 = \|\boldsymbol{B}\|_F^2 + \left(\frac{\partial u}{\partial x}\right)^2 + \left(\frac{\partial v}{\partial y}\right)^2 + \left(\frac{\partial w}{\partial z}\right)^2 + 2\frac{\partial u}{\partial y}\frac{\partial v}{\partial x} + 2\frac{\partial u}{\partial z}\frac{\partial w}{\partial x} + 2\frac{\partial v}{\partial z}\frac{\partial w}{\partial y}, \tag{3-30}$$

then Equation (3-18) can be rewritten as

$$\Omega = \frac{\|\boldsymbol{B}\|_F^2}{\|\boldsymbol{A}\|_F^2 + \|\boldsymbol{B}\|_F^2} = \frac{1}{2 + \frac{g}{\|\boldsymbol{B}\|_F^2}}, \tag{3-31}$$

where

$$g = g_0 + g_x + g_y + g_z\,,$$

$$g_0 = \left(\frac{\partial u}{\partial x}\right)^2 + \left(\frac{\partial v}{\partial y}\right)^2 + \left(\frac{\partial w}{\partial z}\right)^2,$$

$$g_x = 2\frac{\partial v}{\partial z}\frac{\partial w}{\partial y}\,, \tag{3-32}$$

$$g_y = 2\frac{\partial u}{\partial z}\frac{\partial w}{\partial x},$$

$$g_z = 2\frac{\partial u}{\partial y}\frac{\partial v}{\partial x}.$$

Note that $g = -Q$ where $Q = \|\boldsymbol{B}\|_F^2 - \|\boldsymbol{A}\|_F^2$ defined by Hunt et al.[46].

So when $g < 0$, $\Omega > 0.5$. Since g_0 is always nonnegative, $g_x + g_y + g_z$ is necessarily negative inside vortex region, which means, in vortex, the product of the cross-velocity derivatives in two directions must be negative. More analyses for g_x, g_y and g_z will be given in Chapter 4. Now we try to figure out the physical meaning of g.

Recall that the incompressible momentum NS equations are in the form

$$\frac{\partial u}{\partial t} = -u\frac{\partial u}{\partial x} - v\frac{\partial u}{\partial y} - w\frac{\partial u}{\partial z} + \frac{1}{Re}\left(\frac{\partial^2 u}{\partial x^2} + \frac{\partial^2 u}{\partial y^2} + \frac{\partial^2 u}{\partial z^2}\right) - \frac{\partial p}{\partial x}\,, \tag{3-33}$$

$$\frac{\partial v}{\partial t} = -u\frac{\partial v}{\partial x} - v\frac{\partial v}{\partial y} - w\frac{\partial v}{\partial z} + \frac{1}{Re}\left(\frac{\partial^2 v}{\partial x^2} + \frac{\partial^2 v}{\partial y^2} + \frac{\partial^2 v}{\partial z^2}\right) - \frac{\partial p}{\partial y}\,, \tag{3-34}$$

$$\frac{\partial w}{\partial t} = -u\frac{\partial w}{\partial x} - v\frac{\partial w}{\partial y} - w\frac{\partial w}{\partial z} + \frac{1}{Re}\left(\frac{\partial^2 w}{\partial x^2} + \frac{\partial^2 w}{\partial y^2} + \frac{\partial^2 w}{\partial z^2}\right) - \frac{\partial p}{\partial z}\,. \tag{3-35}$$

Then taking partial derivatives along x, y and z, respectively, yields

$$\begin{aligned}\frac{\partial^2 u}{\partial t\partial x} = &-\left(\frac{\partial u}{\partial x}\right)^2 - u\frac{\partial^2 u}{\partial x^2} - \frac{\partial v}{\partial x}\frac{\partial u}{\partial y} - v\frac{\partial^2 u}{\partial x\partial y} - \frac{\partial w}{\partial x}\frac{\partial u}{\partial z} - w\frac{\partial^2 u}{\partial x\partial z}\\ &+\frac{1}{Re}\left(\frac{\partial^3 u}{\partial x^3} + \frac{\partial^3 u}{\partial x\partial y^2} + \frac{\partial^3 u}{\partial x\partial z^2}\right) - \frac{\partial^2 p}{\partial x^2}\,,\end{aligned} \tag{3-36}$$

$$\frac{\partial^2 v}{\partial t \partial y} = -\frac{\partial u}{\partial y}\frac{\partial v}{\partial x} - u\frac{\partial^2 v}{\partial x \partial y} - \left(\frac{\partial v}{\partial y}\right)^2 - v\frac{\partial^2 v}{\partial y^2} - \frac{\partial w}{\partial y}\frac{\partial v}{\partial z} - w\frac{\partial^2 v}{\partial x \partial z} + \frac{1}{Re}\left(\frac{\partial^3 v}{\partial x^2 \partial y} + \frac{\partial^3 v}{\partial y^3} + \frac{\partial^3 v}{\partial y \partial z^2}\right) - \frac{\partial^2 p}{\partial y^2}, \tag{3-37}$$

$$\frac{\partial^2 w}{\partial t \partial z} = -\frac{\partial u}{\partial z}\frac{\partial w}{\partial x} - u\frac{\partial^2 w}{\partial x \partial z} - \frac{\partial v}{\partial z}\frac{\partial w}{\partial y} - v\frac{\partial^2 w}{\partial y \partial z} - \left(\frac{\partial w}{\partial z}\right)^2 - w\frac{\partial^2 w}{\partial z^2} + \frac{1}{Re}\left(\frac{\partial^3 w}{\partial x^2 \partial z} + \frac{\partial^3 w}{\partial y^2 \partial z} + \frac{\partial^3 w}{\partial z^3}\right) - \frac{\partial^2 p}{\partial z^2}. \tag{3-38}$$

By adding Equation (3-36) (3-37) and (3-38), we have

$$\begin{aligned}&\frac{\partial\left(\frac{\partial u}{\partial x} + \frac{\partial v}{\partial y} + \frac{\partial w}{\partial z}\right)}{\partial t} \\ &= -\left(\left(\frac{\partial u}{\partial x}\right)^2 + \left(\frac{\partial v}{\partial y}\right)^2 + \left(\frac{\partial w}{\partial z}\right)^2 + 2\frac{\partial u}{\partial y}\frac{\partial v}{\partial x} + 2\frac{\partial u}{\partial z}\frac{\partial w}{\partial x} + 2\frac{\partial v}{\partial z}\frac{\partial w}{\partial y} + \frac{\partial^2 p}{\partial x^2} + \frac{\partial^2 p}{\partial y^2} + \frac{\partial^2 p}{\partial z^2}\right) \\ &\quad -u\frac{\partial\left(\frac{\partial u}{\partial x} + \frac{\partial v}{\partial y} + \frac{\partial w}{\partial z}\right)}{\partial x} - v\frac{\partial\left(\frac{\partial u}{\partial x} + \frac{\partial v}{\partial y} + \frac{\partial w}{\partial z}\right)}{\partial y} - w\frac{\partial\left(\frac{\partial u}{\partial x} + \frac{\partial v}{\partial y} + \frac{\partial w}{\partial z}\right)}{\partial z} \\ &\quad +\frac{1}{Re}\left(\frac{\partial^2\left(\frac{\partial u}{\partial x} + \frac{\partial v}{\partial y} + \frac{\partial w}{\partial z}\right)}{\partial x^2} + \frac{\partial^2\left(\frac{\partial u}{\partial x} + \frac{\partial v}{\partial y} + \frac{\partial w}{\partial z}\right)}{\partial y^2} + \frac{\partial^2\left(\frac{\partial u}{\partial x} + \frac{\partial v}{\partial y} + \frac{\partial w}{\partial z}\right)}{\partial z^2}\right)\end{aligned} \tag{3-39}$$

From mass equation, we have

$$\frac{\partial u}{\partial x} + \frac{\partial v}{\partial y} + \frac{\partial w}{\partial z} = 0, \tag{3-40}$$

so Equation (3-39) becomes

$$\Delta p + g = 0 \tag{3-41}$$

This is a Poisson's equation. Provided a low-pressure region, $\Delta p > 0$, then $g < 0$. By Equation (3-31), $\Omega > 0.5$, which means Ω method can capture low-pressure region very well. This is consistent with our intuitive understanding that the pressure inside a vortex is lower.

3.4 Summary

In this chapter, an analysis on the symmetric part (deformation) and antisymmetric part (vorticity) of tensor field $\nabla \boldsymbol{V}$ is shown. And the new vortex identification method based on the idea that vorticity overtakes deformation in vortices, Ω-method, is revisited. The Ω-method has a relative uniform threshold to reveal the vortical structures and it is shown that Ω-method can capture the low-pressure zone very well. After equipping the vortex identification method, we can move on to next stage: how Λ vortex form.

Chapter 4

Λ Vortex Formation

In this chapter, the formation of Λ vortex will be revisited based on Liu's Theory and Tian's work [62] in detail by DNS data and Ω method. This is the first step of vortical structures build-up in transitional flow. The perturbation from TS wave develop stronger and twist, then Λ vortex forms. An observation of perturbation development to Λ vortex will be given in section 4.1 and an analysis on the velocity tensor about Λ vortex formation will be given in section 4.2. Section 4.3 will show the structure of Λ vortex and the high shear layer induced by Λ vortex.

4.1 Observation of Perturbation Development to Λ Vortex

Let's recall the inflow condition: the inflow is given by Equation (2-25) in the form of

$$q = q_{lam} + A_{2d} q'_{2d} e^{i(\alpha x - \omega t)} + A_{3d} q'_{3d} e^{i(\alpha x \pm \beta y - \omega t)}$$

where q represents u, v, w, p and T, and q_{lam} represents the Blasius solution for a two-dimensional laminar boundary layer. The 2D and 3D T-S waves are added into inflow as perturbation, as shown in Equation (2-25). Figure 4-1 shows the process of vortical structure build-up in transitional flow, shown by iso-surfaces of $\Omega = 0.502$. Here we use a relatively small Ω to capture the structures of perturbations. By Figure 4-1, we can observe the development of perturbations. They are originally spanwise vortices, and then become stronger and twisted, followed by the formation of Λ vortices.

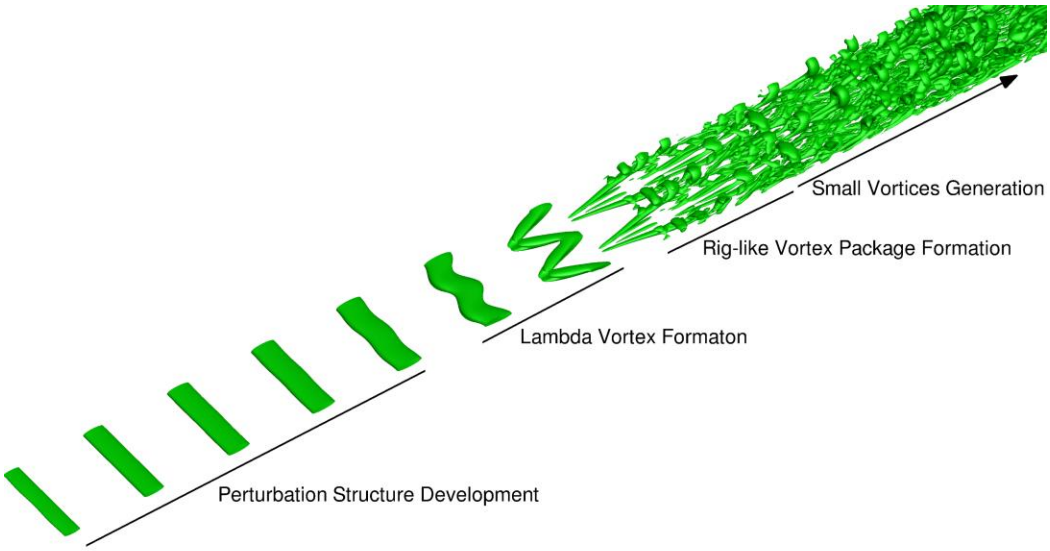

Figure 4-1 The process of vortical structure build-up in transitional flow.

To investigate the details of perturbation development and Λ vortex formation, two spanwise slices (Sy1, Sy2) and seven streamwise slices (Sx1-Sx7) are extracted, see Figure 4-2 and Figure 4-3. Figure 4-2 shows the velocity field distribution on two spanwise slices. From Figure 4-2, we can see the base flow: streamwise velocity u is Blasius flow, while spanwise velocity v and normal velocity w are zeros. Also, we can find some obvious w disturbance s and some inconspicuous v disturbances on the very left of Sy1 and Sy2. These disturbances become gradually significant along x direction, especially after the perturbations are twisted. A special attention should be given to v disturbances which have a more significant growth at where the perturbation twists, while there are w disturbances even at where the perturbation has not been twisted. It seems like the twisting of perturbations and formation of Λ vortices have a strong relation only to the growth of v disturbances. Figure 4-3 shows the velocity field distribution on seven streamwise slices along x direction, where we can investigate v disturbances and w disturbance in more comprehensive perspective. Focusing on Sx4, the disturbances of u, v and w grow to strong enough and are comparable to the base flow. Note that the

slice Sx4 cuts through a twisted perturbation. The black circles on Sx4 are the contour lines of $\Omega = 0.52$, which indicate the positions of vortices. The v disturbances and w disturbances around these black circles shows the vortices has a trend of streamwise rotation. This kind of trend is more significant on Sx2 and Sx1. The observations hint that the twisting of perturbations and formation of Λ vortices are related to both the growth of v disturbances and w disturbance.

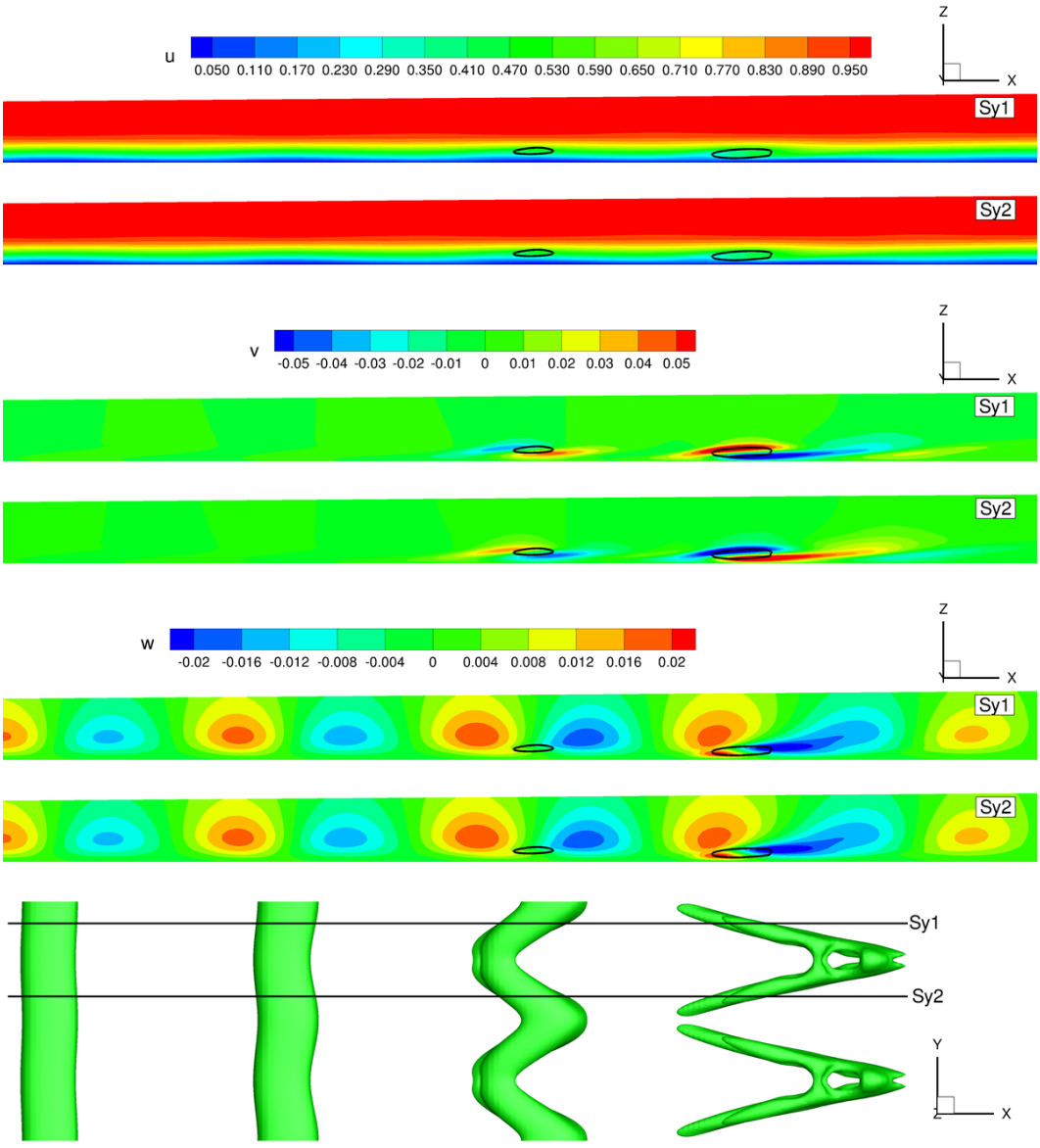

Figure 4-2 Velocity field distribution on two spanwise slices.

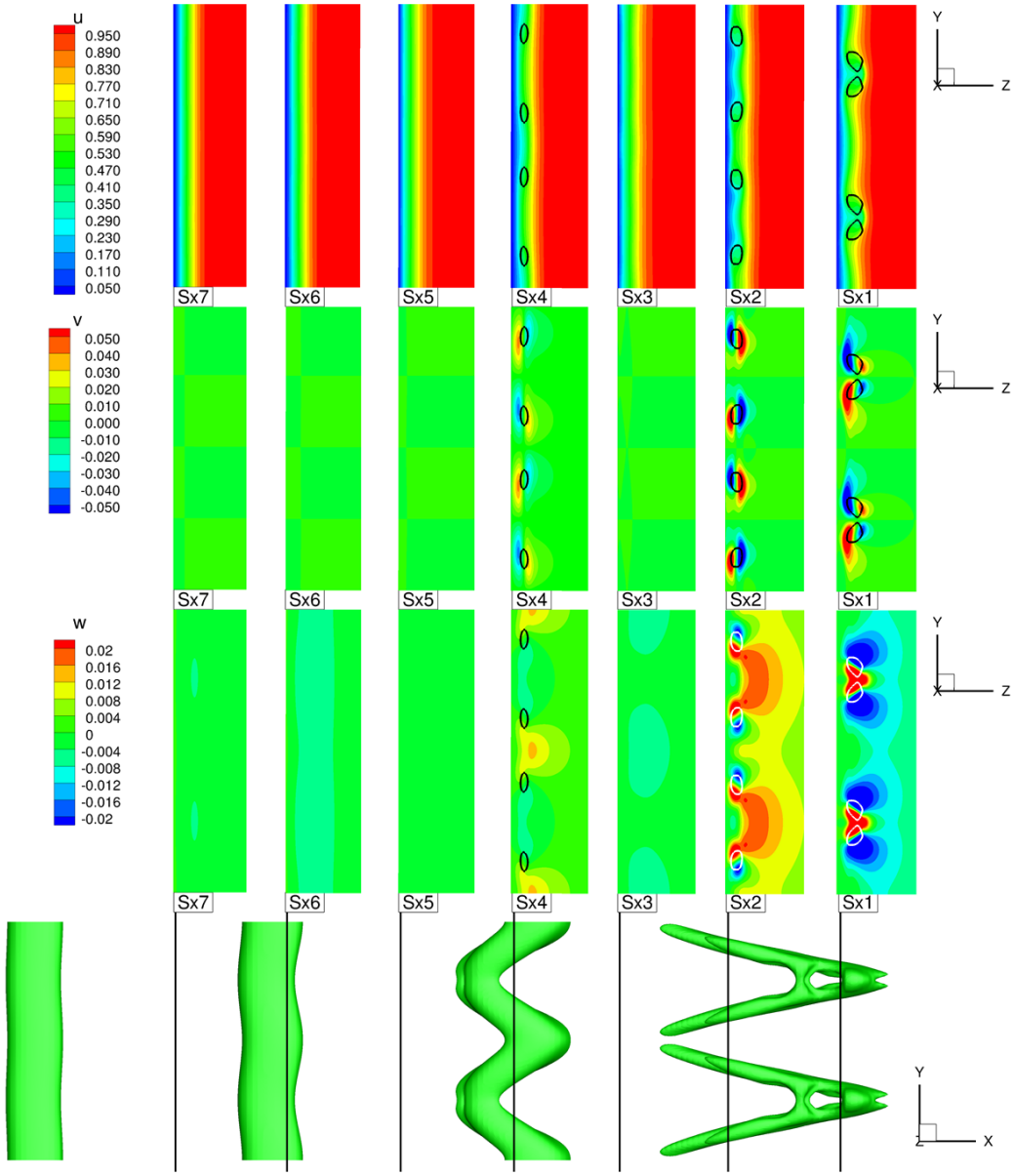

Figure 4-3 Velocity field distribution on seven streamwise slices.

To investigate the change of the velocity field in details, the distributions of velocity tensor field ∇V on Sy1, Sy2 and Sx1-Sx7 are shown in Figure 4-4 to Figure 4-9. The white and black circles on Sy1, Sy2 and Sx1-Sx7 are the contour lines of $\Omega = 0.52$, which indicate the region of vortices. From Figure 4-4, we find $\frac{\partial u}{\partial y}$ has a significant change when perturbation is twisting. Note that $\frac{\partial u}{\partial y}$ have different signs on Sy1 and Sy2 inside vortices (see blue color on Sy1 and red color on Sy2 of $\frac{\partial u}{\partial y}$ at where the perturbation starts twisting). From Figure 4-5, we find $\frac{\partial v}{\partial x}$ and $\frac{\partial v}{\partial z}$ have significant change. Even $\frac{\partial v}{\partial y}$ has a different distribution at where the perturbation is twisting, but the value inside vortices (white circles) almost keep unchanged. Figure 4-6 shows that $\frac{\partial w}{\partial y}$ has a relatively significant change, comparing with $\frac{\partial w}{\partial x}$ and $\frac{\partial w}{\partial z}$, at where the perturbation is twisting. In a different view, Figure 4-7, Figure 4-8 and Figure 4-9 confirm the significant change of $\frac{\partial u}{\partial y}$, $\frac{\partial v}{\partial x}$, $\frac{\partial v}{\partial z}$ and $\frac{\partial w}{\partial y}$, comparing Sx4 with Sx6.

Recalling Equation (3-31) and Equation (3-32)

$$\Omega = \frac{\|\boldsymbol{B}\|_F^2}{\|\boldsymbol{A}\|_F^2 + \|\boldsymbol{B}\|_F^2} = \frac{1}{2 + \frac{g}{\|\boldsymbol{B}\|_F^2}}, \tag{3-31}$$

where

$$g = g_0 + g_x + g_y + g_z ,$$

$$g_0 = \left(\frac{\partial u}{\partial x}\right)^2 + \left(\frac{\partial v}{\partial y}\right)^2 + \left(\frac{\partial w}{\partial z}\right)^2 ,$$

$$g_x = 2\frac{\partial v}{\partial z}\frac{\partial w}{\partial y} , \tag{3-32}$$

$$g_y = 2\frac{\partial u}{\partial z}\frac{\partial w}{\partial x} ,$$

$$g_z = 2\frac{\partial u}{\partial y}\frac{\partial v}{\partial x},$$

we find that $\frac{\partial u}{\partial y}$, $\frac{\partial v}{\partial x}$, $\frac{\partial v}{\partial z}$ and $\frac{\partial w}{\partial y}$ are related to g_z and g_x. Hence, g_z and g_x may play important role in the perturbation development and Λ vortices formation. A detailed investigation will be given in section 4.2.

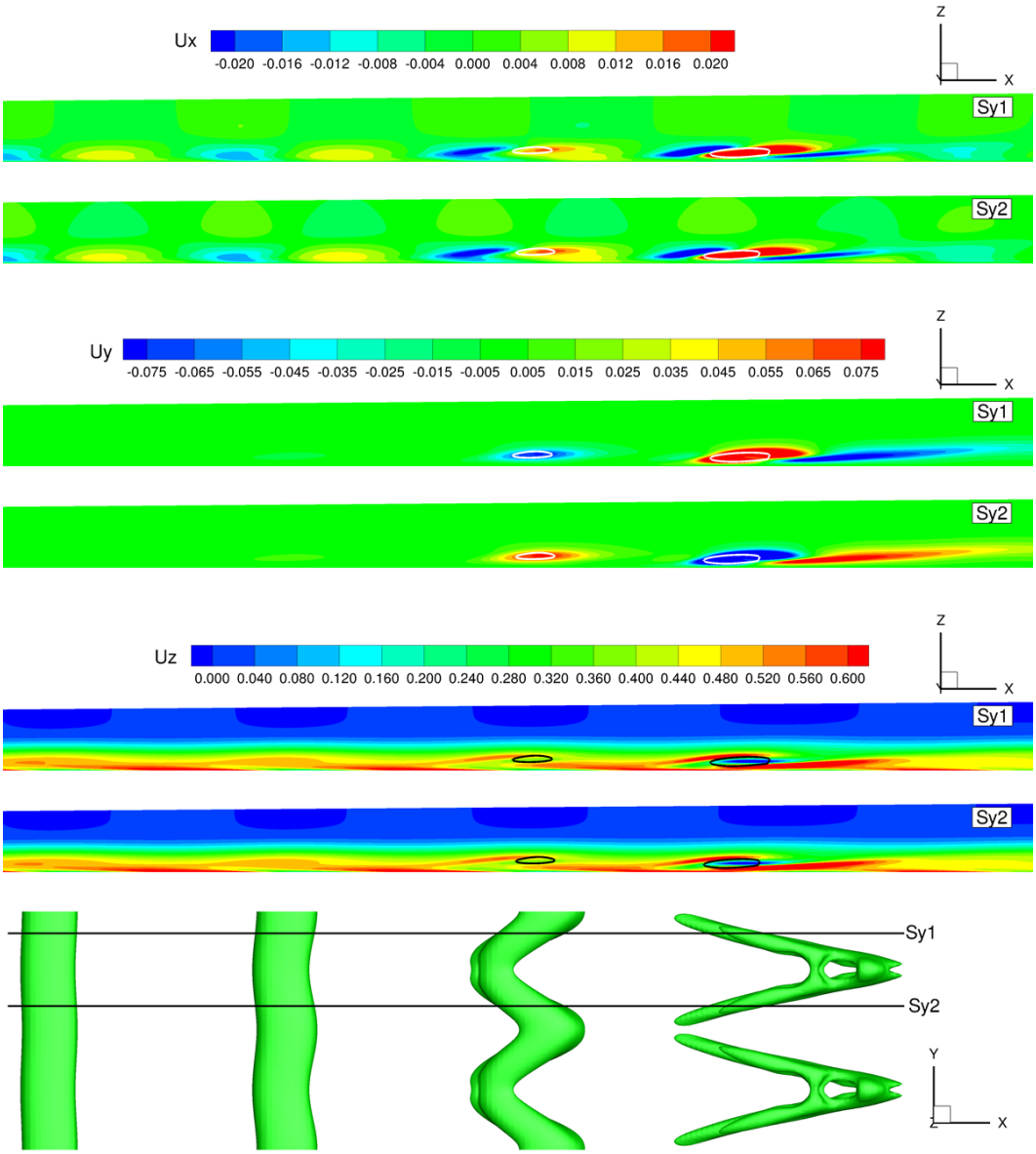

Figure 4-4 Streamwise velocity derivatives ($\frac{\partial u}{\partial x}$, $\frac{\partial u}{\partial y}$ and $\frac{\partial u}{\partial z}$) distribution on two spanwise slices.

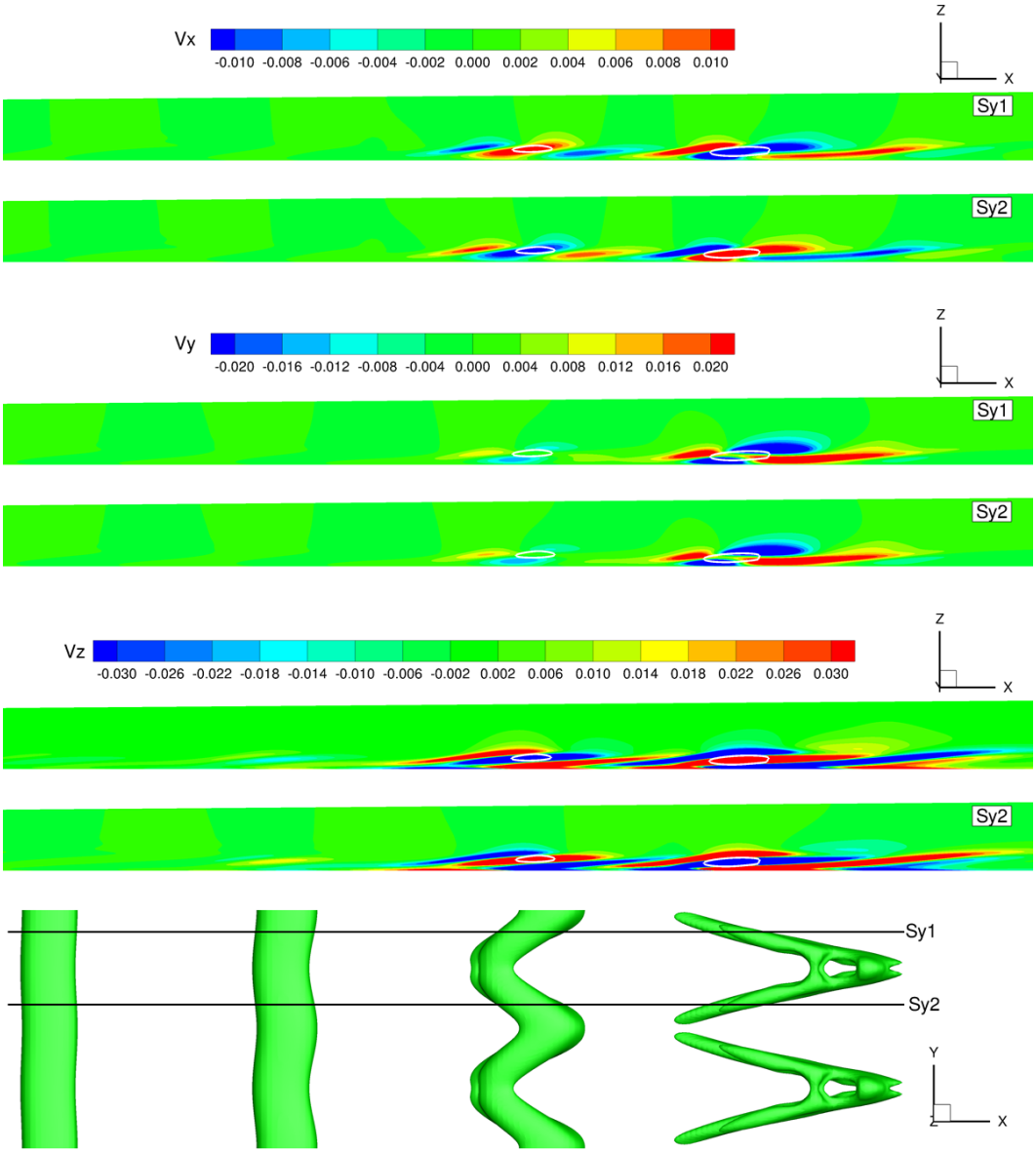

Figure 4-5 Spanwise velocity derivatives ($\frac{\partial v}{\partial x}$, $\frac{\partial v}{\partial y}$ and $\frac{\partial v}{\partial z}$) distribution on two spanwise slices.

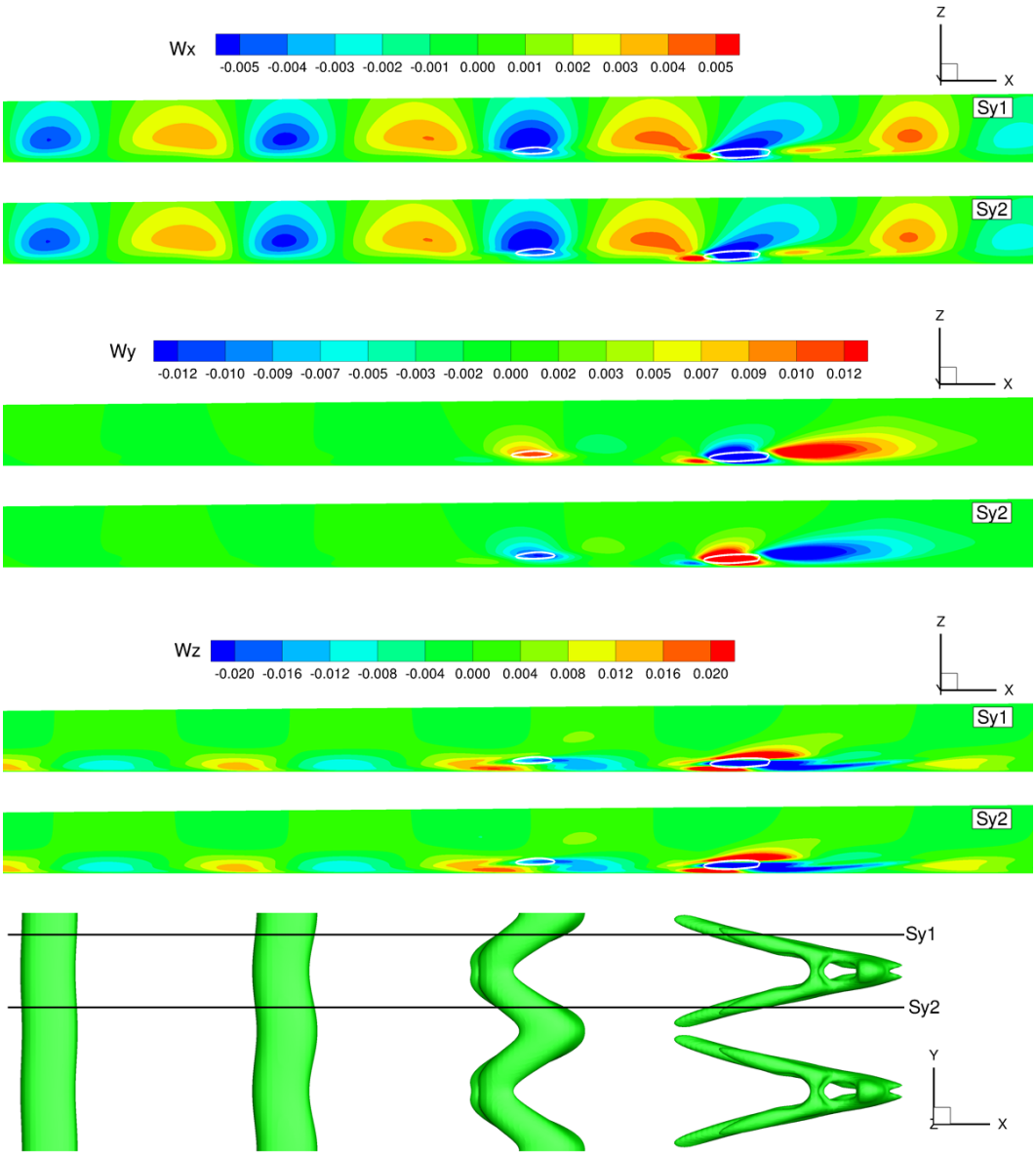

Figure 4-6 Normal velocity derivatives ($\frac{\partial w}{\partial x}$, $\frac{\partial w}{\partial y}$ and $\frac{\partial w}{\partial z}$) distribution on two spanwise slices.

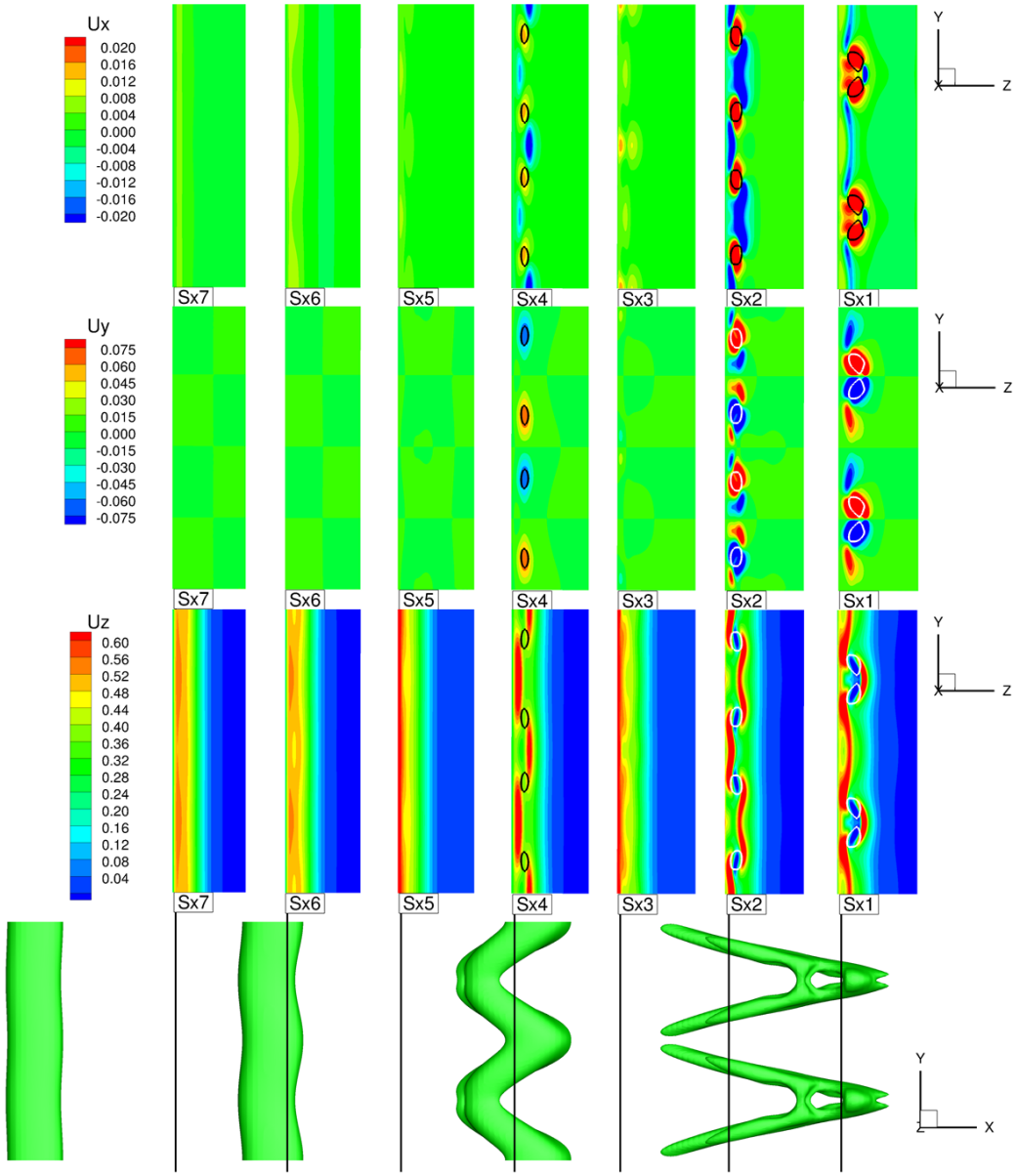

Figure 4-7 Streamwise velocity derivatives ($\frac{\partial u}{\partial x}$, $\frac{\partial u}{\partial y}$ and $\frac{\partial u}{\partial z}$) distribution on seven streamwise slices.

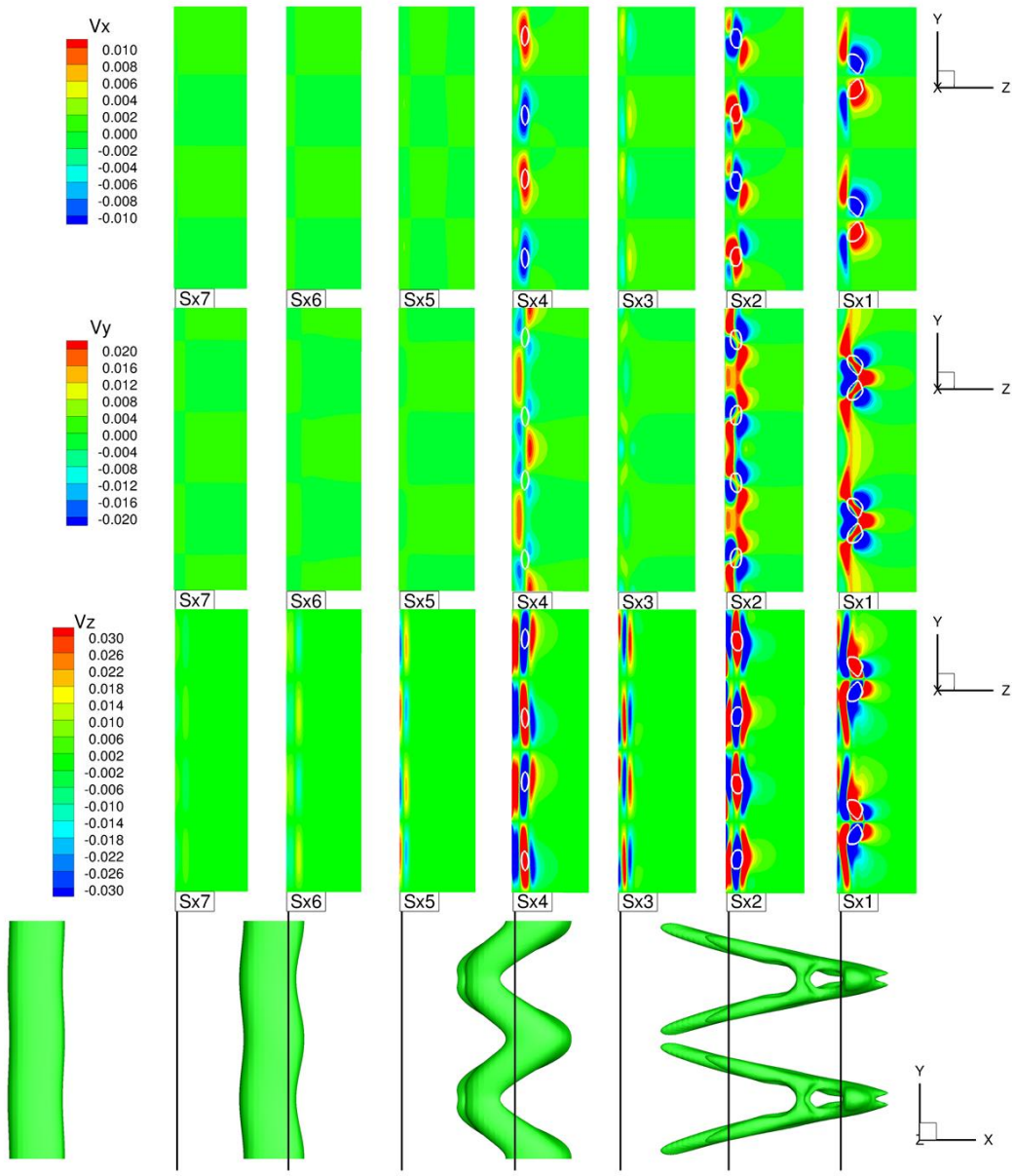

Figure 4-8 Spanwise velocity derivatives ($\frac{\partial v}{\partial x}$, $\frac{\partial v}{\partial y}$ and $\frac{\partial v}{\partial z}$) distribution on seven streamwise slices.

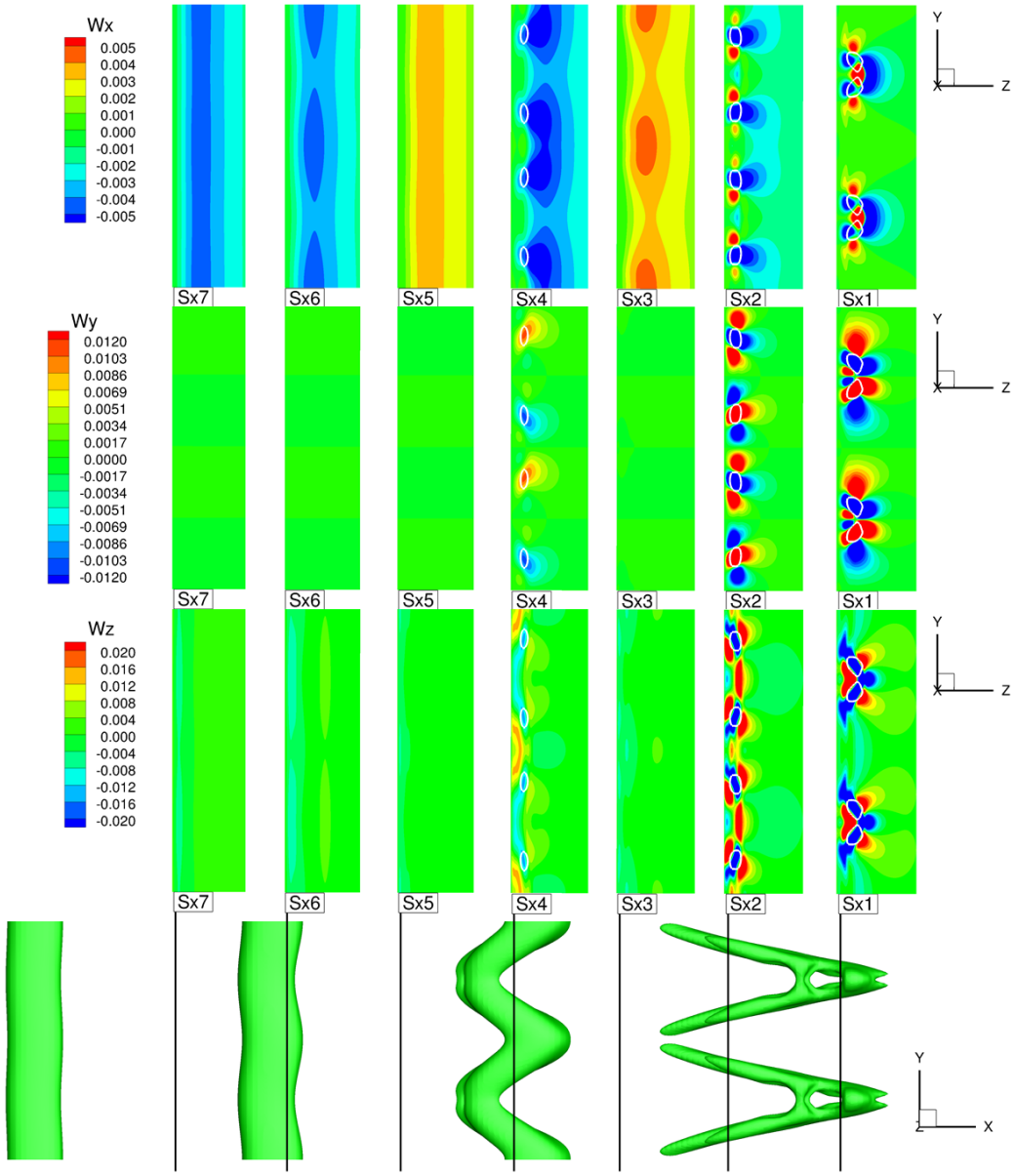

Figure 4-9 Normal velocity derivatives ($\frac{\partial w}{\partial x}$, $\frac{\partial w}{\partial y}$ and $\frac{\partial w}{\partial z}$) distribution on seven streamwise slices.

4.2 Tensor Analyses on Λ Vortex Formation

To investigate the change of velocity tensor field ∇V when Λ vortex forms, the maximal Ω at every x is found and the position is recorded. Note all data in this section are recorded on these positions, basically, the positions where maximal Ω for every x locate.

Figure 4-10 gives the change of maximal Ω along x. It shows that maximal Ω becomes larger and larger in the process of perturbation development. When perturbation is twisted, Ω has a remarkable increase, see Ω at $x = 413$. And after Λ vortex forms, Ω has a huge jump, from 0.5 to 0.78. It indicates Λ vortex has a pretty strong rotation, comparing with the former perturbation.

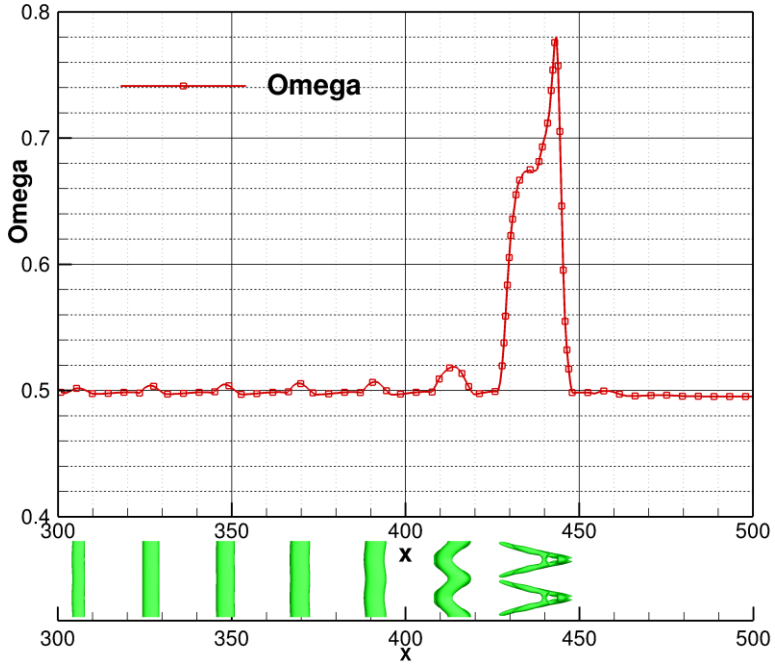

Figure 4-10 The change of maximal Ω along X.

The changes of g, g_0, g_x, g_y and g_z along x are shown in Figure 4-11. Recall Equation (3-31) and Equation (3-32),

$$\Omega = \frac{\|\boldsymbol{B}\|_F^2}{\|\boldsymbol{A}\|_F^2 + \|\boldsymbol{B}\|_F^2} = \frac{1}{2 + \frac{g}{\|\boldsymbol{B}\|_F^2}},$$

$$g = g_0 + g_x + g_y + g_z$$

$$g_0 = \left(\frac{\partial u}{\partial x}\right)^2 + \left(\frac{\partial v}{\partial y}\right)^2 + \left(\frac{\partial w}{\partial z}\right)^2,$$

$$g_x = 2\frac{\partial v}{\partial z}\frac{\partial w}{\partial y},$$

$$g_y = 2\frac{\partial u}{\partial z}\frac{\partial w}{\partial x},$$

$$g_z = 2\frac{\partial u}{\partial y}\frac{\partial v}{\partial x}.$$

From Figure 4-11, we can see g_y is the principal component of g for perturbations. Figure 4-12 gives the change of $\frac{\partial u}{\partial z}$ and $\frac{\partial w}{\partial x}$ along x. And g_y is the double product of $\frac{\partial u}{\partial z}$ and $\frac{\partial w}{\partial x}$. We find $\frac{\partial u}{\partial z}$ is far greater than $\frac{\partial w}{\partial x}$ (Note that the scales of $\frac{\partial u}{\partial z}$ and $\frac{\partial w}{\partial x}$ are different in Figure 4-12). The greater $\frac{\partial u}{\partial z}$ is the result of Blasius flow and $\frac{\partial w}{\partial x}$ is from TS wave. Now we focus on the position $x = 410$. The remarkable changes of g_x and g_z arise. As a result, g becomes greater in amplitude with a negative sign. This is consistent with remarkable increase of Ω in Figure 4-10. Figure 4-13 shows the changes of the components of g_x, $\frac{\partial v}{\partial z}$ and $\frac{\partial w}{\partial y}$, along x. By Figure 4-13, we can see both $\frac{\partial v}{\partial z}$ and $\frac{\partial w}{\partial y}$ are increasing in amplitude around $x = 410$ and the change of $\frac{\partial v}{\partial z}$ is more significant. Hence $\frac{\partial v}{\partial z}$ is the most important reason of g_x changing when perturbation is twisted. Figure 4-14 gives the changes of the components of g_z, $\frac{\partial u}{\partial y}$ and $\frac{\partial v}{\partial x}$, along x. By Figure 4-14, we find that $\frac{\partial u}{\partial y}$ plays a more important role at $x = 410$, where the perturbation is twisted. Figure 4-15 shows the changes of $\frac{\partial u}{\partial x}$, $\frac{\partial v}{\partial y}$ and $\frac{\partial w}{\partial z}$ along x, which are the components of g_0. $\frac{\partial u}{\partial x}$ and

$\frac{\partial w}{\partial z}$ change in an opposite pattern at the beginning, as a result of TS wave. A notice should be given to $\frac{\partial v}{\partial y}$. It is almost zero before perturbation distortion and become negative at $x = 410$ where perturbation is twisted. Noting that $\frac{\partial u}{\partial y}, \frac{\partial v}{\partial y}$ and $\frac{\partial w}{\partial y}$ play some roles in perturbation twisting, it gives us an inspiration about the inlet condition: The 3D TS wave q'_{3d} in Equation (2-25) is very important in perturbation development and Λ formation.

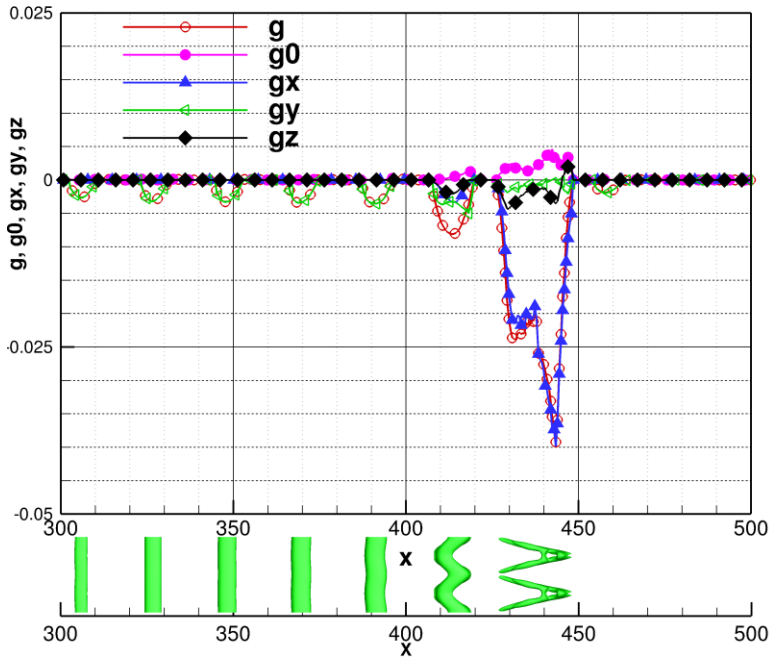

Figure 4-11 The changes of g, g_0, g_x, g_y and g_z along X.

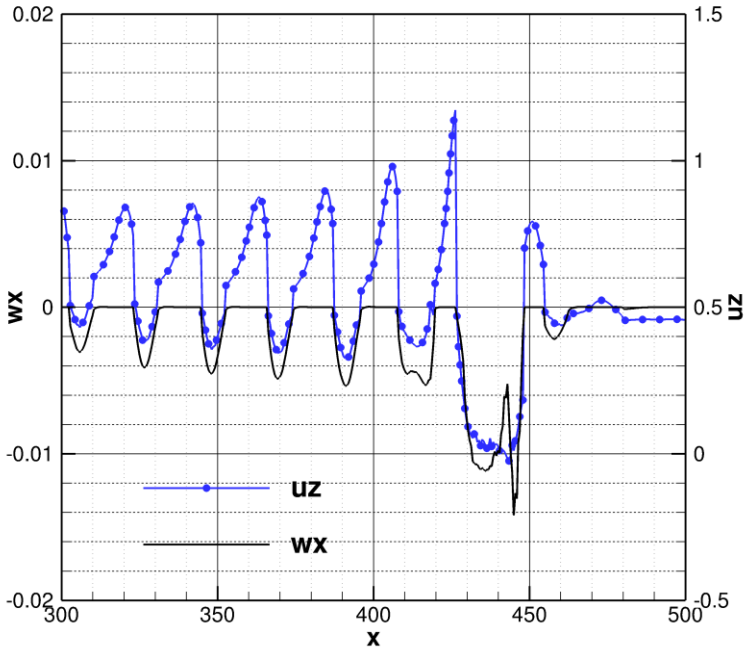

Figure 4-12 The change of $\frac{\partial u}{\partial z}$ and $\frac{\partial w}{\partial x}$ along X.

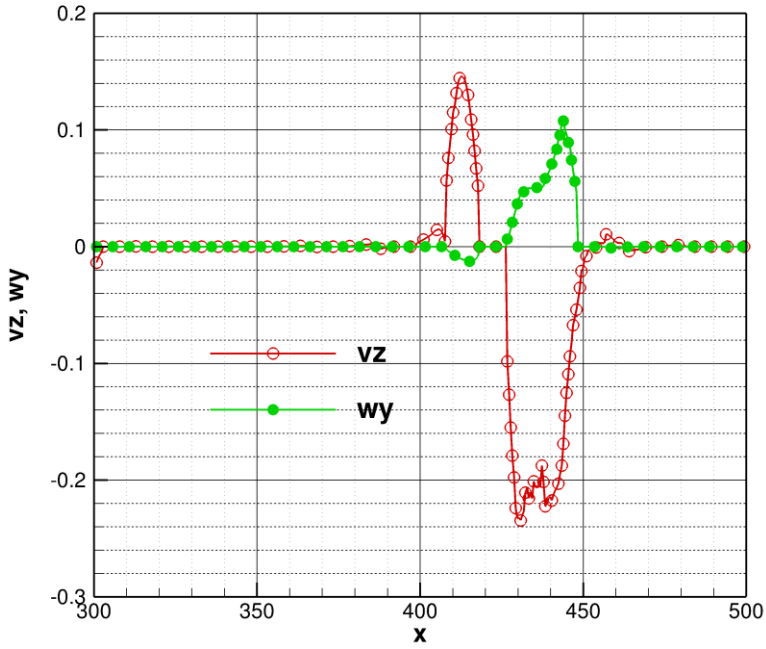

Figure 4-13 The change of $\frac{\partial v}{\partial z}$ and $\frac{\partial w}{\partial y}$ along X.

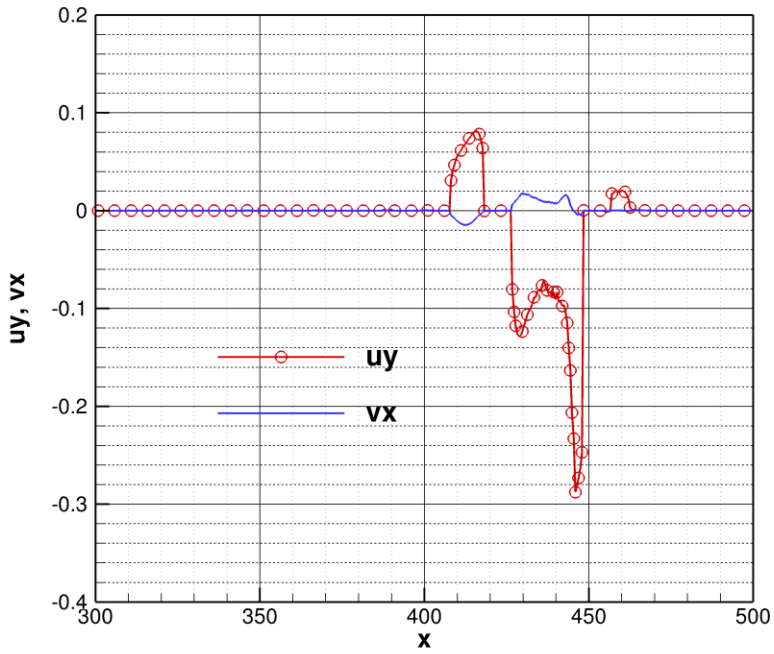

Figure 4-14 The change of $\frac{\partial u}{\partial y}$ and $\frac{\partial v}{\partial x}$ along X.

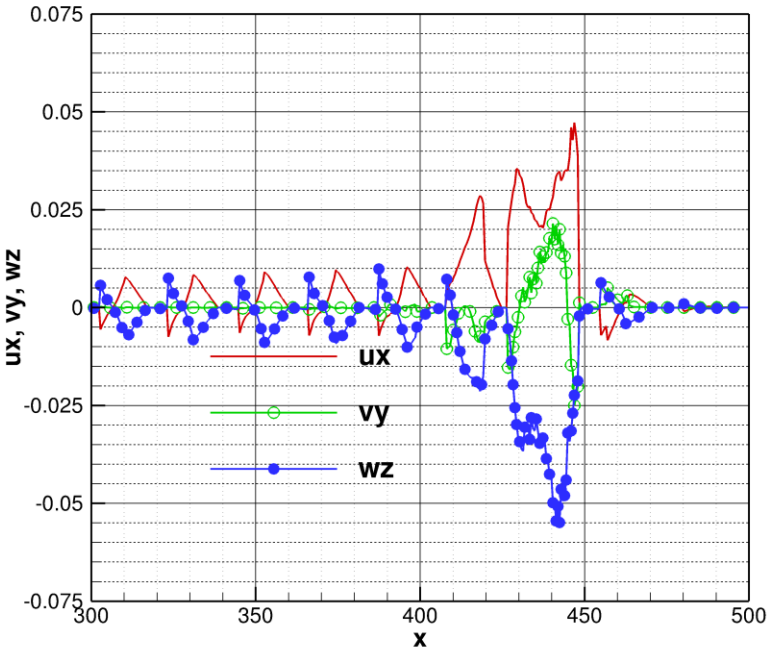

Figure 4-15 The change of $\frac{\partial u}{\partial x}$, $\frac{\partial v}{\partial y}$ and $\frac{\partial w}{\partial z}$ along X.

4.3 Λ-Vortex Structure and High Shear Layer

Figure 4-16 gives the structures of Λ-vortex and strain rate in different views at $t = 6.0T$, where T is T-S wave period. The green surface is the iso-surface of $\Omega = 0.52$ which indicates the structure of Λ-vortex while the yellow surface is the iso-surface of $\|\boldsymbol{A}\|_F = 0.6$ which show the position of shear layer. According to Figure 4-16, the shear layer concentrates beyond the head of the Λ-vortex.

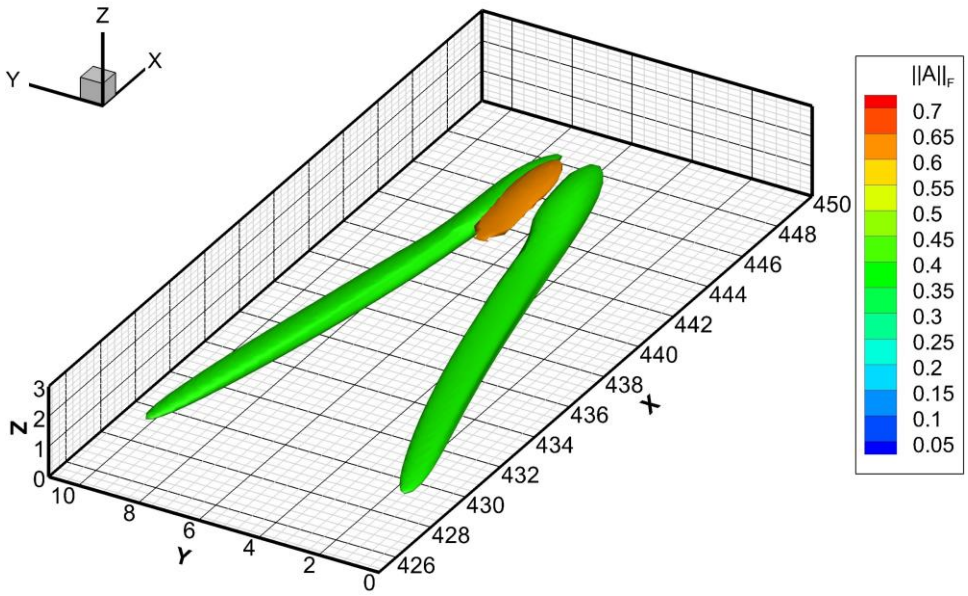

(a) Glabal view

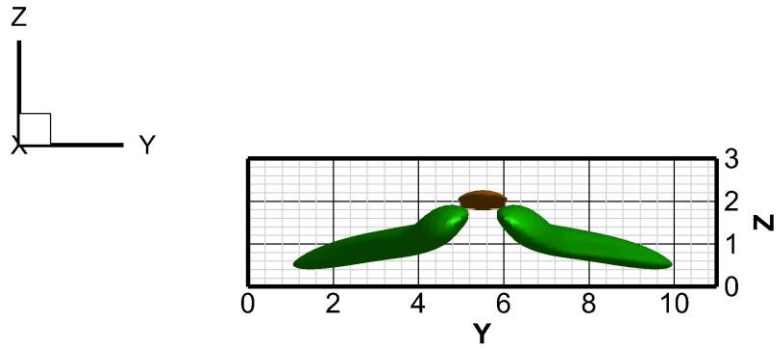

(b) Y-Z view

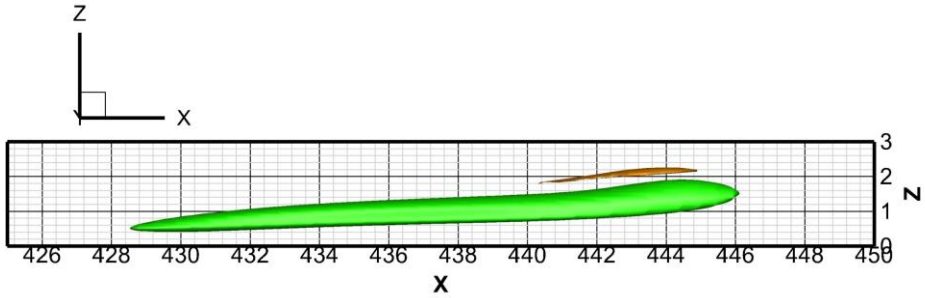

(c) X-Z view

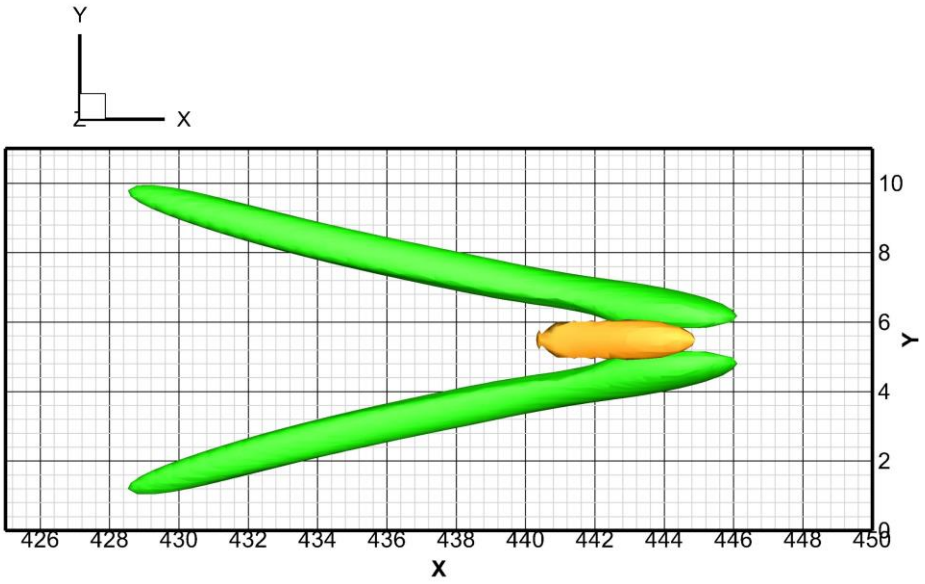

(d) X-Y view

Figure 4-16 The iso-surfaces of $\Omega = 0.52$ (green) and $\|\boldsymbol{A}\|_F = 0.6$ (yellow) at $t = 6.0T$, where T is the period of T-S wave.

When we increase the iso-value of Ω, see Figure 4-17, the shear layer places at the same position along streamwise direction with the iso-surface of $\Omega = 0.65$. It indicates the shear layer is high near the strong vortex. Figure 4-18 gives a more clear explanation. The distributions of ω_x and u on the slice $x = 443$ are given in Figure 4-18(b) and (c). We can find a strong rotation exist at this position and the low speed zone is swept to higher

position, then $\frac{\partial u}{\partial z}$ becomes greater around the position $y = 5.5, z = 2$, where the shear layer places.

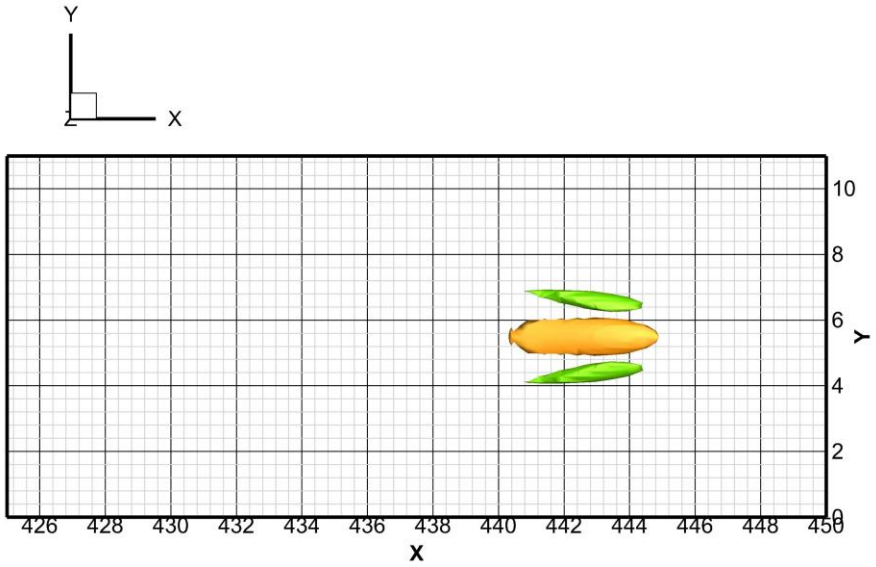

Figure 4-17. The iso-surfaces of $\Omega = 0.65$ (green) and $\|\boldsymbol{A}\|_F = 0.6$ (yellow) at $t = 6.0T$, where T is the period of T-S wave.

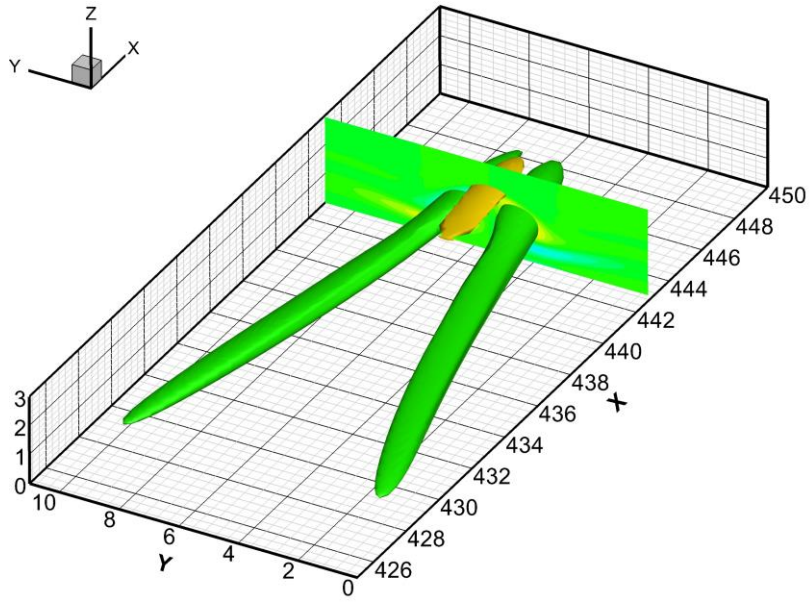

(a) Position of the slice of $x = 443$.

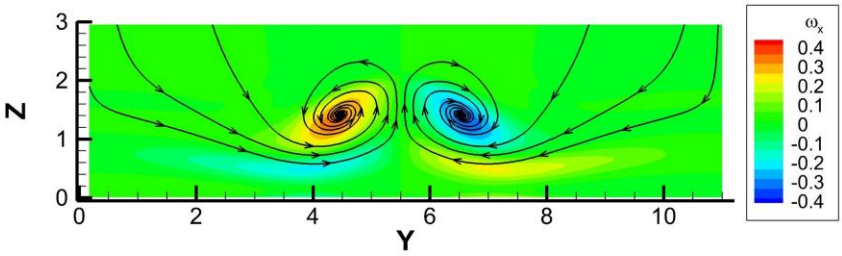

(b) ω_x with stream traces.

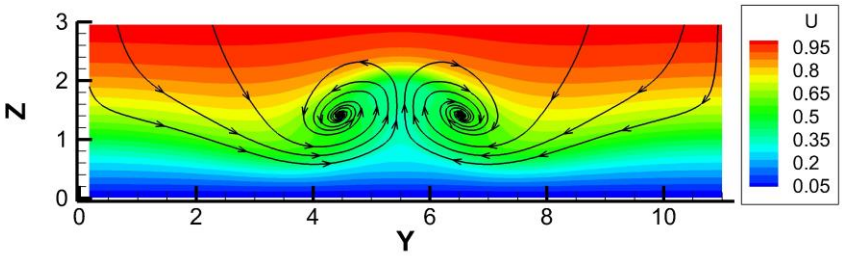

(c) u with stream traces

Figure 4-18. The distribution of ω_x and u on the slice of $x = 443$.

4.4 Summary

In this chapter, the development of perturbation and formation of Λ vortex are observed and analyzed. The partial derivative of velocity along spanwise plays an significant role in perturbation twisting and Λ vortex formation. The Λ vortices are in pair with counter-rotation, resulting in an ejection effect that take the low speed near wall up. A high shear layer generates above the head of Λ vortices because of the ejection effect of Λ vortices. An analysis of shear instability will be given in next chapter.

Chapter 5

Shear Instability Analysis

In this chapter, an analysis about shear instability will be given. The stability analysis is on the Orr-Sommerfeld equation and the derivation of Orr-Sommerfeld equation will be given in section 5.1. The Chebyshev polynomials and nodes will be revisited in section 5.2 and the Chebyshev spectral method for linear stability analysis will be shown in section 5.3. In section 5.4, we will validate the code of Chebyshev spectral method and give the numerical results of shear instability.

5.1 Derivation of Orr-Sommerfeld equation

The Orr-Sommerfeld equation, in fluid dynamics, is an eigenvalue equation describing the linear modes of disturbance to a viscous parallel flow. It is derived from incompressible and non-dimensional Navier-Stokes equations. Equation (5-1) denotes the incompressible and non-dimensional Navier-Stokes equations in which, $\boldsymbol{V} = (u, v, w)$ is the velocity vector.

$$\begin{cases} \dfrac{\partial \boldsymbol{V}}{\partial t} + \boldsymbol{V} \cdot \nabla \boldsymbol{V} = -\nabla p + \dfrac{1}{Re}\nabla^2 \boldsymbol{V} \\ \nabla \cdot \boldsymbol{V} = 0 \end{cases} \tag{5-1}$$

Considering that

$$q(x, y, z, t) = q_0(y) + q'(x, y, z, t)\,, \tag{5-2}$$

where q can be specified as (u, v, w, p) , and $q_0 = (u_0, v_0, w_0, p_0)$ which represents the value of mean flow, and q' denotes the corresponding linear perturbation. By eliminating the second order perturbation terms, the linearized governing equation for small perturbations can be written as,

$$\begin{cases} \dfrac{\partial \boldsymbol{V}'}{\partial t} + (\boldsymbol{V_0} \cdot \nabla)\boldsymbol{V}' + (\boldsymbol{V}' \cdot \nabla)\boldsymbol{V_0} + \nabla p' = \dfrac{\nabla^2 \boldsymbol{V}'}{Re} \\ \nabla \cdot \boldsymbol{V}' = 0 \end{cases}. \tag{5-3}$$

To simplify the problem, a localized 2-D incompressible temporal stability for shear layer is studied. Assume the normal mode is

$$\begin{aligned} \boldsymbol{V}' &= \widehat{\boldsymbol{V}}(y)e^{i(\alpha x+\beta z-\omega t)} + c.c. = \widehat{\boldsymbol{V}}(y)e^{i\alpha\left(x+\frac{\beta}{\alpha}z-ct\right)} + c.c. \\ p' &= \hat{p}(y)e^{i(\alpha x+\beta z-\omega t)} + c.c. = \hat{p}(y)e^{i\alpha\left(x+\frac{\beta}{\alpha}z-ct\right)} + c.c. \ , \\ c &= \frac{\omega}{\alpha} \end{aligned} \tag{5-4}$$

where $\widehat{\boldsymbol{V}} = (\hat{u}, \hat{v}, \hat{w})$ and $\alpha, \beta \in \mathbb{R}$ are the streamwise and spanwise wave numbers, $\omega \in \mathbb{C}$ is the frequency and $c = \frac{\omega}{\alpha} \in \mathbb{C}$ is the phase speed. The choice of a complex frequency ω and real wave numbers is known as the temporal problem where the spatial structure of the wavelike perturbation is unchanged and the amplitude of the wave grows or decays as time progresses.

Plugging Equation (5-4) and $\boldsymbol{V_0} = (u_0, 0, 0)$ in Equation (5-3) yields

$$\begin{aligned} &\mathcal{L}\hat{u} = Re(\mathcal{D}u_0)\hat{v} + i\alpha Re\hat{p} \\ &\mathcal{L}\hat{v} = Re(\mathcal{D}\hat{p}) \\ &\mathcal{L}\widehat{w} = i\beta Re\ \hat{p} \\ &i(\alpha\hat{u} + \beta\widehat{w}) + \mathcal{D}\hat{v} = 0 \end{aligned} \ , \tag{5-5}$$

where $\mathcal{L} = [\mathcal{D}^2 - (\alpha^2 + \beta^2) - iRe(\alpha u_0 - \omega)]$, and $\mathcal{D} = \frac{d}{dy}$.

By eliminating $\hat{u}, \widehat{w}, \hat{p}$ and denote $u_0 = U(y)$, we can obtain the O-S equation on $\hat{v}$,

$$\left(-Uk^2 - U'' - \frac{k^4}{i\alpha Re}\right)\hat{v} + \left(U + \frac{2k^2}{i\alpha Re}\right)\hat{v}'' - \frac{1}{i\alpha Re}\hat{v}'''' = c(\hat{v}'' - k^2\hat{v}), \tag{5-6}$$

where $k^2 = \alpha^2 + \beta^2$. The equation is named after William McFadden Orr and Arnold Sommerfeld, who derived it at the beginning of the 20th century.

Consider O-S equation on the interval $[-1,1]$, the boundary conditions yield

$$\hat{v}(\pm 1) = \hat{v}'(\pm 1) = 0 \tag{5-7}$$

Equation (5-6) is an eigenvalue problem about $\hat{v}$ with eigenvalue c. The eigenvalue c determines the property of stability of the flow. Let $c = c_r + ic_i$, Equation (5-4) yields

$$\boldsymbol{V}'(x,y,z,t) = \widehat{\boldsymbol{V}}(y)e^{\alpha c_i t + i\alpha\left(x+\frac{\beta}{\alpha}z - c_r t\right)},$$

$$p'(x,y,z,t) = \hat{p}(y)e^{\alpha c_i t + i\alpha\left(x+\frac{\beta}{\alpha}z - c_r t\right)}.$$

if $c_i > 0$, then the disturbance will continuously grow and the flow would be unstable. While if c_r is greater, the disturbance will grow faster and the flow would be more unstable. But if $c_i < 0$, the flow would be stable. This chapter will use Chebyshev spectral method to solve this eigenvalue equation. Let's revisit Chebyshev polynomials and nodes at first.

5.2 Chebyshev Polynomials and Nodes

Chebyshev polynomials, named after Pafnuty Chebyshev, are a sequence of orthogonal polynomials. In this paper, we use Chebyshev polynomials of the first kind which can be defined as the unique polynomials satisfying

$$T_n(y) = \cos(n\, cos^{-1}(y)), \tag{5-8}$$

where n is the order of polynomials.

For example,

$$T_0(y) = 1$$

$$T_1(y) = y$$

$$T_2(y) = 2y^2 - 1$$

$$T_3(y) = 4y^3 - 3y$$

$$\vdots$$

The derivatives of Chebyshev polynomials have the following recurrence relation

$$
\begin{aligned}
&T_0^{(k)}(y_j) = 0, \\
&T_1^{(k)}(y_j) = T_0^{(k-1)}(y_j), \\
&T_2^{(k)}(y_j) = 4T_1^{(k-1)}(y_j), \\
&T_n^{(k)}(y_j) = 2nT_{n-1}^{(k-1)}(y_j) + \frac{n}{n-2}T_{n-2}^{(k)}(y_j), \quad n = 3,4,\ldots
\end{aligned}
\tag{5-9}
$$

with the superscript $k \geq 1$ denoting the order of differentiation.

Chebyshev nodes are the roots of the Chebyshev polynomial of the first kind, which are algebraic numbers. For a given natural number N, Chebyshev nodes in the interval $(-1,\ 1)$ are

$$
y_j = \cos\left(\frac{2j+1}{2N}\pi\right),\ j = 0,1,\ldots,N-1 \tag{5-10}
$$

They are often used as nodes in polynomial interpolation because the resulting interpolation polynomial minimizes the effect of Runge's phenomenon. A brief deduction is given as follows.

Given a function $f \in \mathcal{C}^N[-1,1]$ and Chebyshev nodes $y_0, \ldots, y_{N-1}$, for each $y \in [-1,1]$, a number $\xi(y)$ exists in $(-1,1)$ with

$$
f(y) - P_{N-1}(y) = \frac{f^{(N)}(\xi(y))}{N!}\prod_{j=0}^{N-1}(y - y_j) \tag{5-11}
$$

where $P_{N-1}(y)$ is the Lagrange interpolating polynomial.

Notice that $\prod_{j=0}^{N-1}(y - y_j)$ is the monic Chebyshev polynomial, that is, $\prod_{j=0}^{N-1}(y - y_j) = \frac{T_N(y)}{2^{N-1}}$.

Recall $T_N(y) = \cos(n\,cos^{-1}(y))$, we have

$$
\left|\prod_{j=0}^{N-1}(y - y_j)\right| \leq \frac{1}{2^{N-1}}
$$

Then

$$\max_{y\in[-1,1]}|f(y)-P_{N-1}(y)| \le \frac{1}{2^{N-1}N!}\max_{y\in[-1,1]}\left|f^{(N)}(y)\right|$$

As N increases, effect of Runge's phenomenon will be minimized.

5.3 Chebyshev Spectral Method for Linear Stability Analysis

Spectral methods have a significant impact on the accurate discretization of both initial value problems and eigenvalue problems. And spectral method with Chebyshev polynomials has been advantageous, especially in stability analysis of fluid mechanics.

In this stability analysis, the function $\hat{v}$ could be approximated by Chebyshev expansion,

$$\hat{v}(y)=\sum_{n=0}^{\infty}a_nT_n(y)\approx\sum_{n=0}^{N-1}a_nT_n(y)\,, \tag{5-12}$$

where N is the number of Chebyshev polynomials, T_n are the Chebyshev polynomials which are used to approximate the velocity profile and a_n are the coefficients.

By approximating $\hat{v}$ with a certain Chebyshev expansion, Equation (5-6) gives

$$\sum_{n=0}^{N-1}\left[\left(-Uk^2-U''-\frac{k^4}{i\alpha Re}\right)T_n+\left(U+\frac{2k^2}{i\alpha Re}\right)T_n''-\frac{1}{i\alpha Re}T_n''''\right]a_n = c\sum_{n=0}^{N}a_n(T_n''-k^2T_n) \tag{5-13}$$

The discretized boundary conditions read

$$\sum_{n=0}^{N-1}a_nT_n(1)=0 \qquad \sum_{n=0}^{N-1}a_nT_n(-1)=0$$

$$\sum_{n=0}^{N-1}a_nT_n'(1)=0 \qquad \sum_{n=0}^{N-1}a_nT_n'(-1)=0$$

Applying Equation (5-14) on the whole grids with boundary conditions above, a matrix form of generalized eigenvalue problem is given by the form

$$\boldsymbol{A}\boldsymbol{a} = c\boldsymbol{B}\boldsymbol{a} \tag{5-14}$$

with the right-hand side

$$c\boldsymbol{B}\boldsymbol{a} =$$

$$c\begin{pmatrix} T_0(1) & T_1(1) & \cdots \\ T_0'(1) & T_1'(1) & \cdots \\ T_0''(y_2) - k^2 T_0(y_2) & T_1''(y_2) - k^2 T_1(y_2) & \cdots \\ \vdots & \vdots & \vdots \\ T_0''(y_{N-3}) - k^2 T_0(y_{N-3}) & T_1''(y_{N-3}) - k^2 T_1(y_{N-3}) & \cdots \\ T_0'(-1) & T_1'(-1) & \cdots \\ T_0(-1) & T_1(-1) & \cdots \end{pmatrix} \begin{pmatrix} a_0 \\ a_1 \\ a_2 \\ \vdots \\ a_{N-3} \\ a_{N-2} \\ a_{N-1} \end{pmatrix}$$

and similarly for the left-hand side $\boldsymbol{A}\boldsymbol{a}$. We have chosen to use the first, second, last and next-to-last row of $\boldsymbol{B}$ to implement the four boundary conditions. The same rows in the matrix $\boldsymbol{A}$ can be chosen as a complex multiple of the corresponding rows in $\boldsymbol{B}$. By carefully selecting this complex multiple, the spurious modes associated with the boundary conditions can be mapped to an arbitrary location in the complex plane.

The matrix form of this system can be rewritten as

$$\boldsymbol{B}^{-1}\boldsymbol{A}\boldsymbol{a} = c\boldsymbol{a}\,,$$

where c appears as eigenvalue of matrix $\boldsymbol{B}^{-1}\boldsymbol{A}$ with the associated eigenfunction $\hat{v}(y) = \sum_{n=0}^{N-1} a_n T_n(y)$.

Then we have a set of Orr-Sommerfeld modes, denoted as $\{\hat{v}_n, c_n\}_{n=0}^{N-1}$. Note that if c_n has greatest imaginary part, then associated $\hat{v}_n$ is most unstable.

5.4 Code Validation and Numerical Results

In this section, we validate the code by the numerical results of two specific flow, which are plane Poiseuille flow and Couette flow. Then a typical shear and a shear from DNS database are analyzed according to the numerical results.

5.4.1 Plane Poiseuille flow

Poiseuille flow is pressure-induced flow (Channel Flow) in a long duct. Specifically, it is assumed that there is Laminar Flow of an incompressible Newtonian Fluid of viscosity induced by a constant positive pressure difference or pressure drop in a long duct. The schematic diagram of plane Poiseuille flow is given in Figure 5-1.

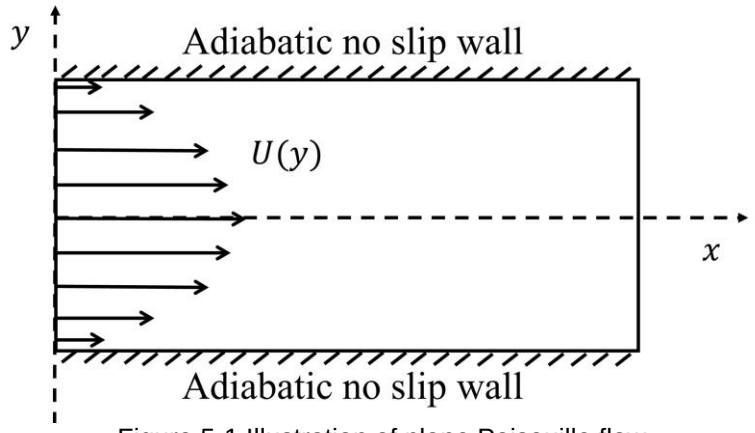

Figure 5-1 Illustration of plane Poiseuille flow.

A typical velocity profile of plane Poiseuille flow is given by Equation (5-15).

$$U(y) = 1 - y^2, \qquad y \in [-1,1] \tag{5-15}$$

To apply Chebyshev Spectral Method, the computing parameters are given as following:

- number of O-S nodes is $N = 100$,
- streamwise wave number is $\alpha = 1$,
- spanwise wave number is $\beta = 0$.

We run two cases here, which are low Reynolds number and high Reynolds number, respectively.

a) Reynolds number is $Re = 1000$.

This case has a low Reynolds number. After running, we obtain the spectrum of plane Poiseuille flow that is shown in Figure 5-2. We can observe that all phase speed c have negative imaginary part. So the flow is stable when $Re = 1000$.

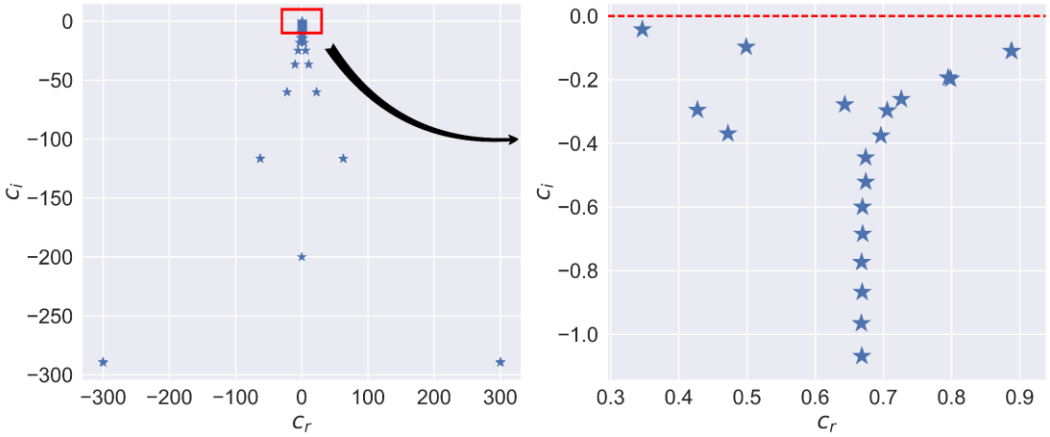

(a) Global view (b) Zoom in view

Figure 5-2 Spectrum of plane Poiseuille flow ($Re = 1000$).

b) Reynolds number is $Re = 10000$.

This case has a high Reynolds number. The spectrum is shown in Figure 5-3. From the spectrum, we find one unstable mode whose phase speed is $c = 0.2377 + 0.0037i$. Because of positive imaginary part, the flow is unstable. And the eigenfunction $\hat{v}$ associated with this unstable mode is shown in Figure 5-4.

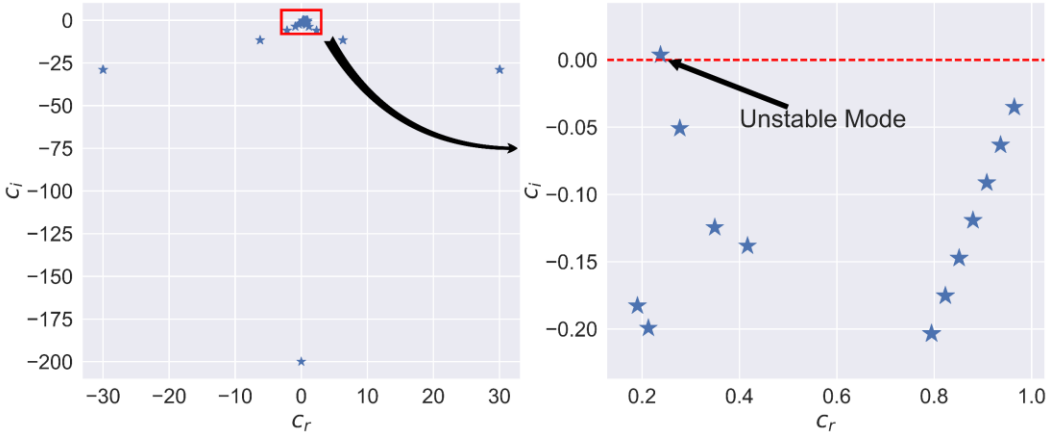

(a) Global view (b) Zoom-in view

Figure 5-3 Spectrum of plane Poiseuille flow ($Re = 10000$).

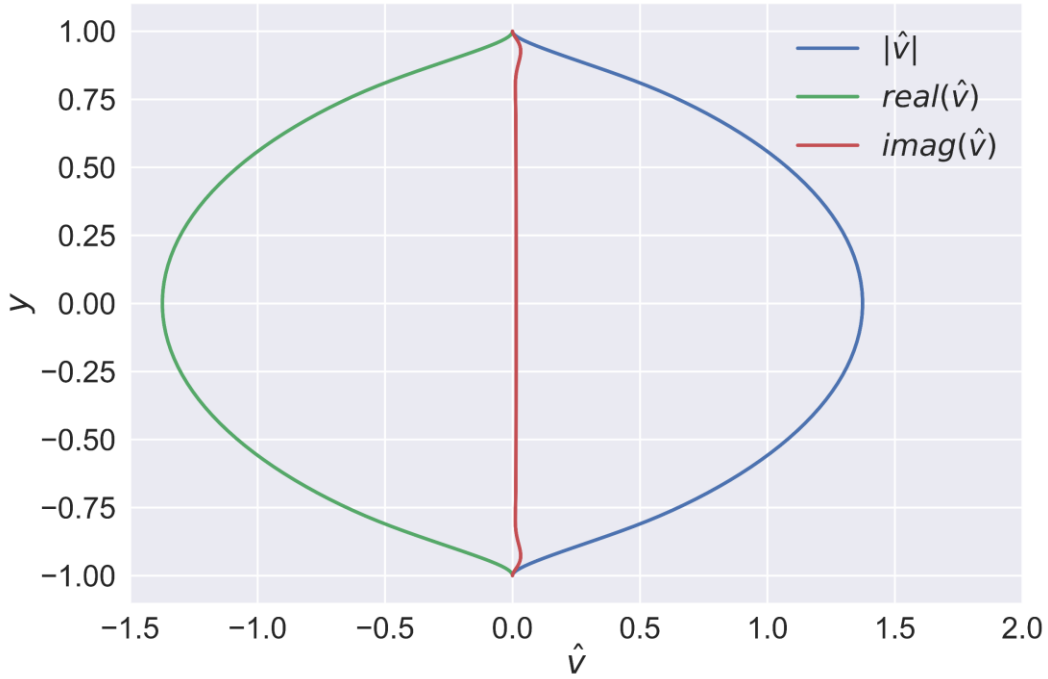

Figure 5-4 Eigenfunction $\hat{v}$ associated with $c = 0.2377 + 0.0037i$.

Therefore, the plane Poiseuille flow is conditional stable, which is consistent with theoretical results.

5.4.2 Couette flow

Couette flow is the flow of a viscous fluid in the space between two surfaces, one of which is moving tangentially relative to the other. The flow is driven by virtue of viscous drag force acting on the fluid, but may additionally be motivated by an applied pressure gradient in the flow direction. The schematic diagram of Couette flow is given in Figure 5-5.

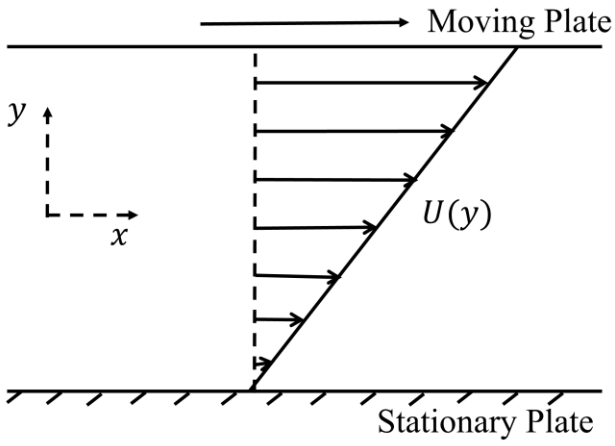

Figure 5-5 Illustration of Couette flow.

A typical velocity profile of Couette flow is given by Equation (5-16)

$$U(y) = y, \qquad y \in [-1,1] \tag{5-16}$$

We give the same computing parameters as in plane Poiseuille flow: $N = 100$, $\alpha = 1$ and β =0. We run several cases for different Reynolds number $(10\sim10000)$, and this kind of flow is always stable. Figure 5-6 shows spectrum of the case with low Reynolds number $Re = 1000$. All modes has a negeative imaginary part, so this kind flow is stable when $Re = 1000$. For other cases, the distributions of spectrum are similar. And the numerical results are consistent with theoretical results.

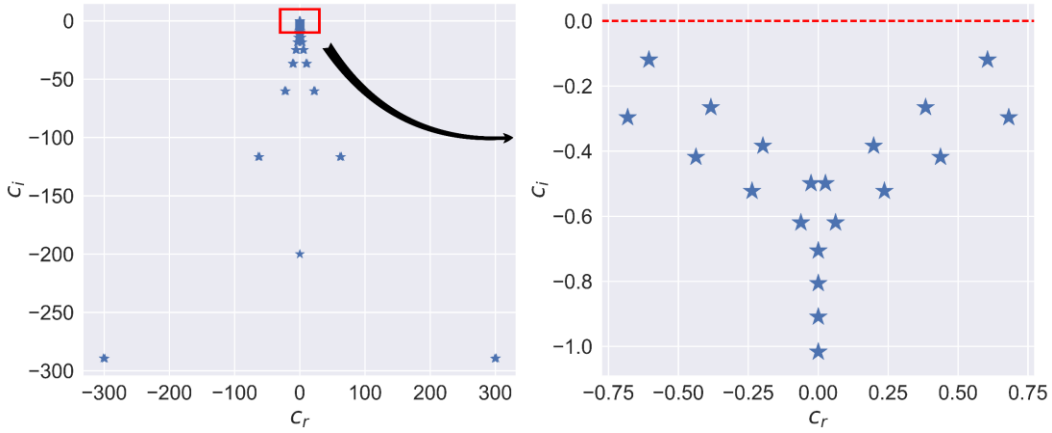

(a) Global view (b) Zoom-in view

Figure 5-6 Spectrum of plane Couette flow ($Re = 1000$).

5.4.3 Typical shear

The velocity profile of a typical shear is shown in Figure 5-7. It is simulated by the hyperbolic tangent function,

$$U(y) = \tanh(4y)\,,\ y \in [-1,1] \tag{5-17}$$

We give the same computing parameters as in two previous flows: $N = 100$, $\alpha = 1$ and β =0. We run two cases with low Reynolds number $Re = 1000$ and even lower Reynolds number $Re = 10$.

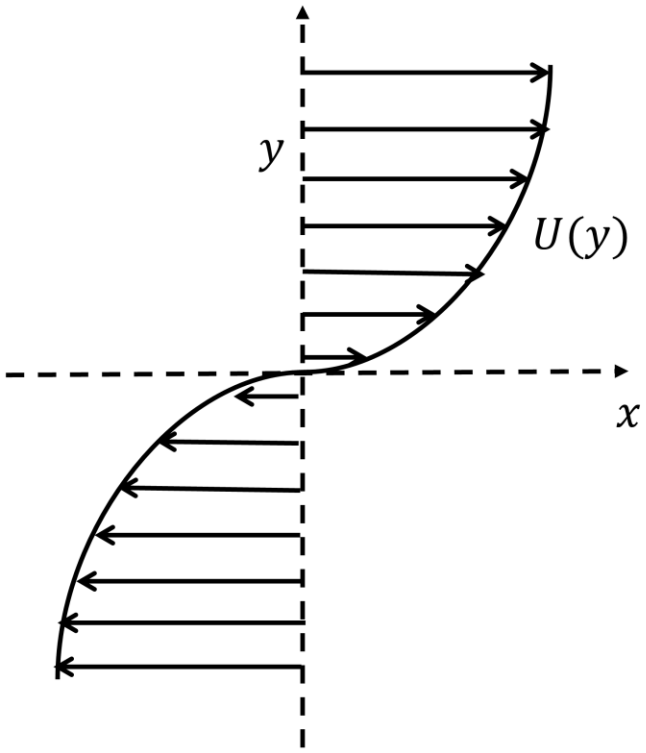

Figure 5-7 Illustration of a typical shear.

a) Reynolds number is $Re = 1000$.

This case has a low Reynolds number. The spectrum is shown in Figure 5-8. From the spectrum, we find one unstable mode whose phase speed is $c = 0.5114i$. Because of positive imaginary part, the flow is unstable. In addition, the eigenfunction $\hat{v}$ associated with this unstable mode is shown in Figure 5-9.

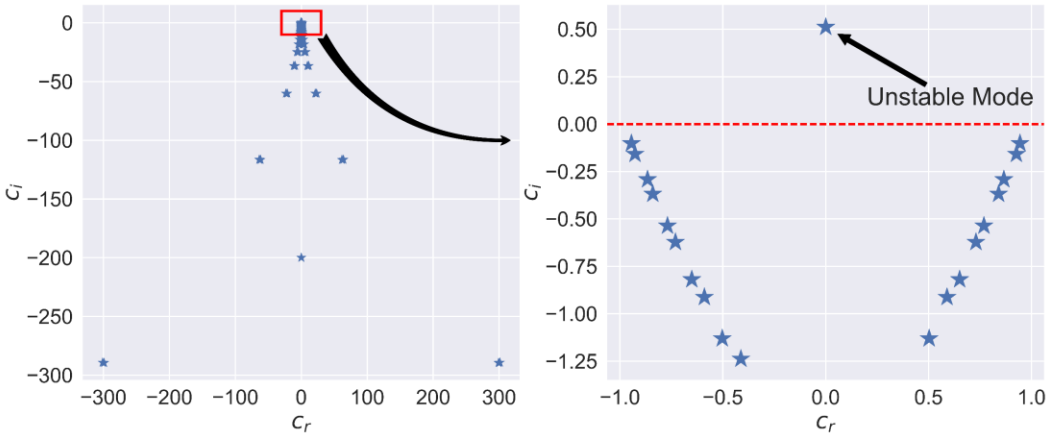

(a) Global view (b) Zoom-in view

Figure 5-8 Spectrum of shear flow ($Re = 1000$).

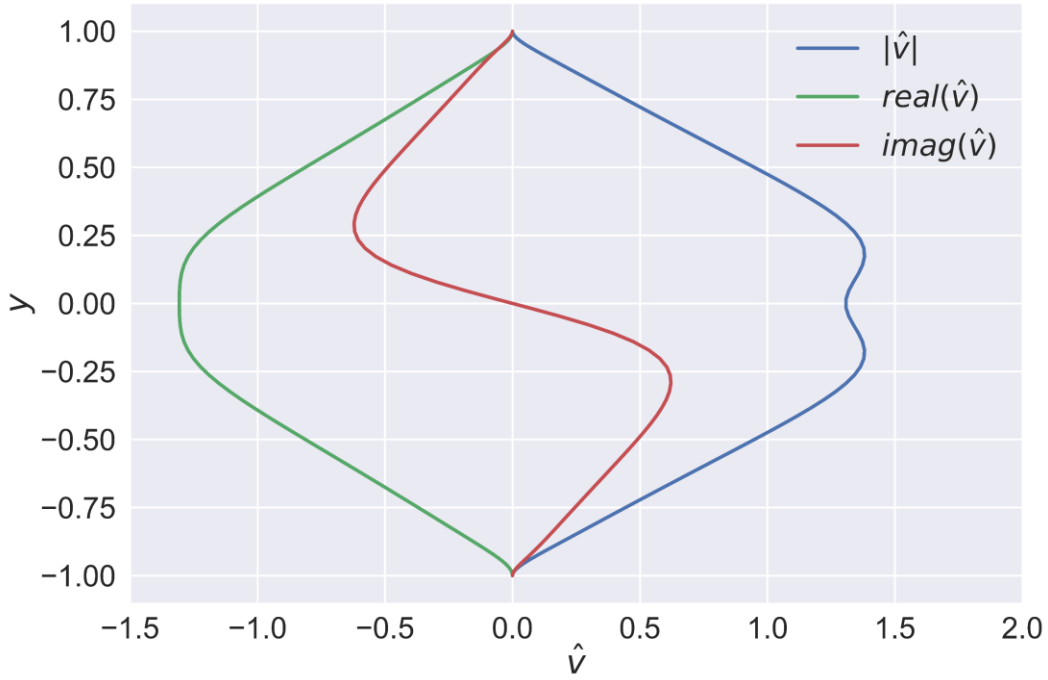

Figure 5-9 Eigenfunction $\hat{v}$ associated with $c = 0.5114i$.

b) Reynolds number is $Re = 10$.

This case has a lower Reynolds number. After running, we obtain the spectrum that is shown in Figure 5-10. We can observe that all phase speed c have negative imaginary part. So the shear flow is stable when $Re = 10$.

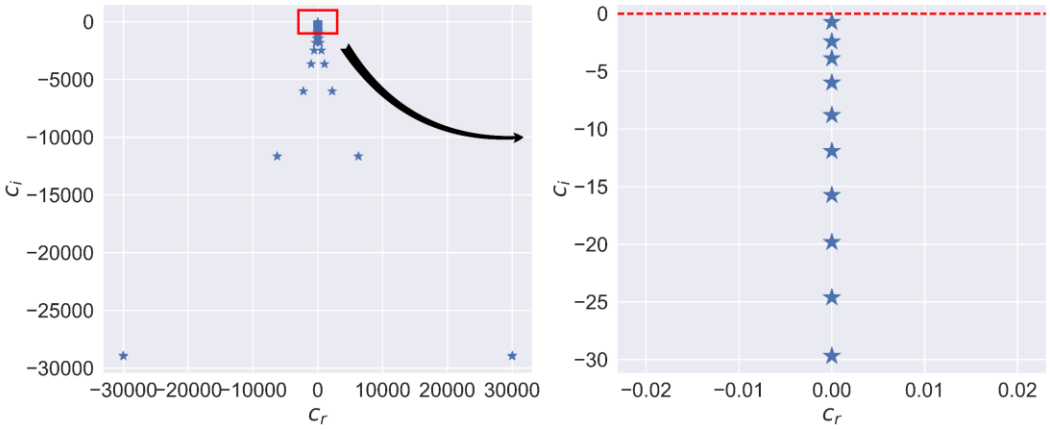

(a) Global view (b) Zoom-in view

Figure 5-10 Spectrum of shear flow ($Re = 10$).

Therefore, this typical shear flow is conditional stable.

5.4.4 Shear from DNS data

Recall Figure 4-18, a high shear layer generates above the head of Λ vortices because of the ejection effect of Λ vortices. Now we extract a velocity profile from DNS data at the position $x = 443.5$ and $y = 5.5$ at $t = 6.00T$, as shown in Figure 5-11. This velocity profile represents a real shear in transitional flow and we will analyze the stability by Chebyshev spectrum method.

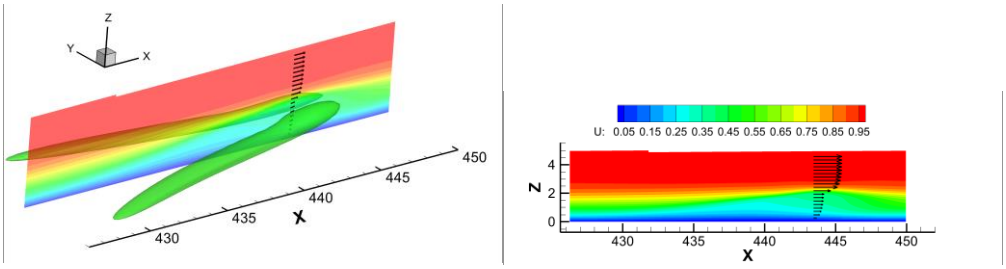

(a) b)

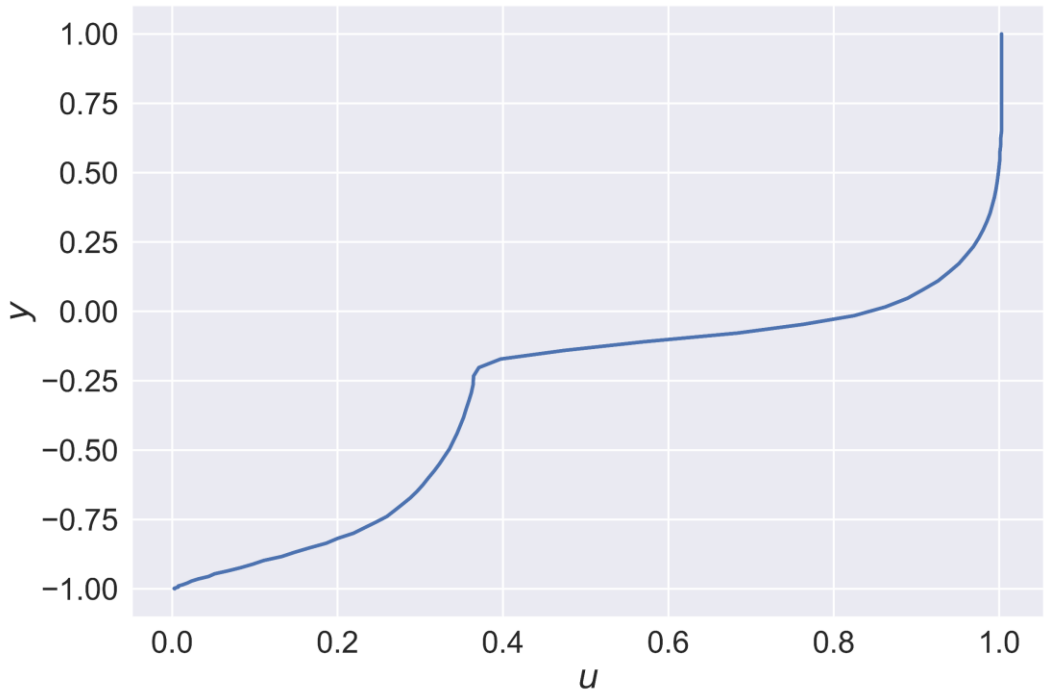

(c)

Figure 5-11 A shear profile extracted from DNS data. (a) shows a global view of vortex structures by iso-surface $\Omega = 0.52$ and the position of x-z plane where we do data extraction; (b) shows the velocity profile we extract and (c) gives an aesthetic description of velocity profile.

The same computing parameters are given as in previous flows: $N = 100$, $\alpha = 1$ and β =0. We run the case with Reynolds number $Re = 1000$ which is consistent with DNS computation condition, see Table 2-3. The spectrum of this flow is shown in Figure 5-12. We find one unstable mode with associated phase speed $c = 0.626 + 0.0053i$. Hence this shear flow is unstable. And the eigenfunction $\hat{v}$ associated with this unstable mode is shown in Figure 5-13.

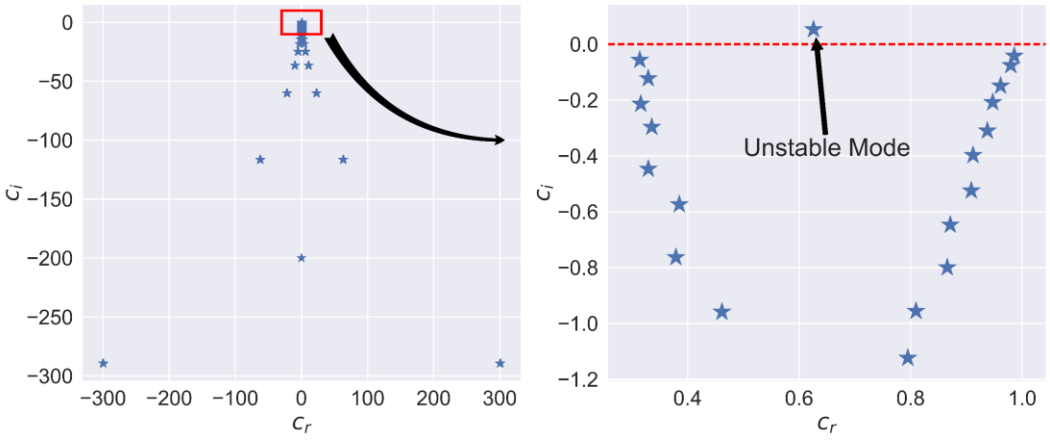

(a) Global view (b) Zoom-in view

Figure 5-12 Spectrum of shear flow from DNS data ($Re = 1000$).

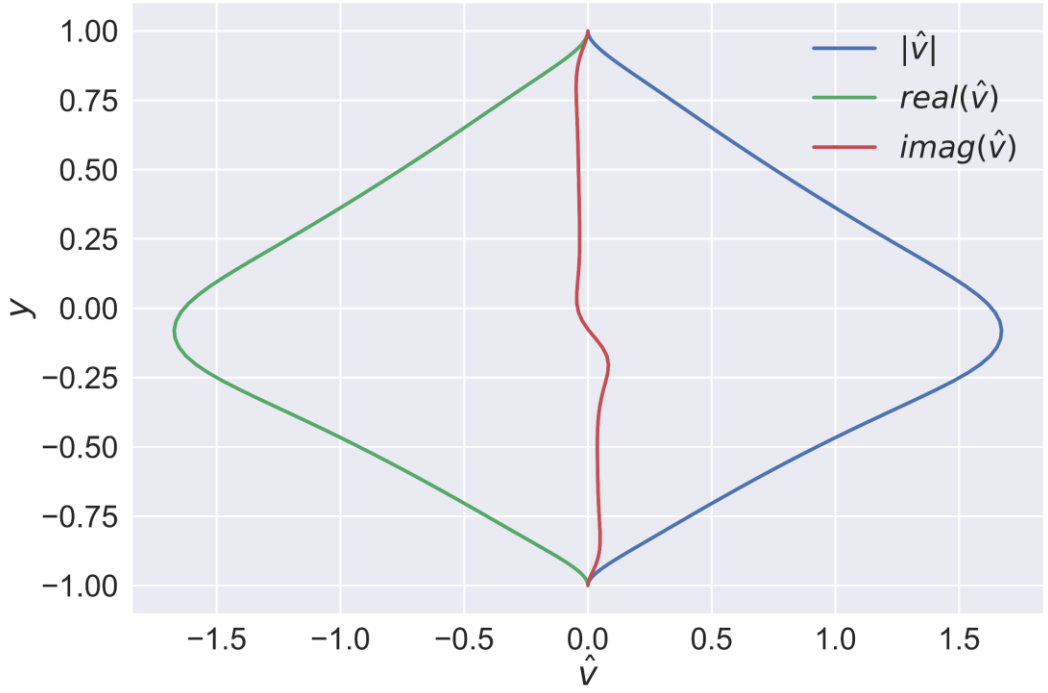

Figure 5-13 Eigenfunction $\hat{v}$ associated with $c = 0.626 + 0.0053i$.

5.5 Summary

In this chapter, Orr-Sommerfeld equation is derived and the Chebyshev spectral method is introduced to solve the stability problem. By Chebyshev spectral method, we find the shear induced by Λ vortex ejection is unstable. Then question is: if the shear is unstable, what is it going to be? The development of Λ vortex to hairpin vortex packets will be given in next chapter.

Chapter 6

Development of Λ Vortex to Hairpin Vortex Packet

After showing the instability of high shear layer induced by Λ vortex ejection, a detailed observation is carried out to figure out the process of a Λ vortex developing to a vortex packet, based on the DNS data and Ω vortex identification method. A sketch of a hairpin vortex will be given in section 6.1 and the details of development of Λ vortex to hairpin vortex packet will be shown in section 6.2. Section 6.3 will reveal an interesting phenomenon about the speed around the hairpin vortices.

6.1 Hairpin Vortex Structure

Hairpin vortices are widely recognized as a fundamental coherent structure since their appearance in every significant process during transition. Figure 6-1 depicts the sketch of a typical symmetric hairpin vortex [52]. The hairpin vortex usually consists of three parts: (1) Two counter-rotating quasi-streamwise vortices, known as two legs; (2) A ring-like vortex named as the vortex head, where the spanwise vorticity is dominant, sitting on top farther from the wall, (3) Necks connect the head and legs. The head is always Ω-shaped and the term “vortex ring” is often used alternatively to describe the combination of head and necks.

“Sweeps” and “ejections” refer to $(u'v')_4$ and $(u'v')_2$ from quadrant analysis. Events associated with Λ vortex or hairpin legs are called “first ejection” and “first sweep” while “second ejection” and “second sweep” are used to describe events related to the vortex rings, see Figure 6-1.

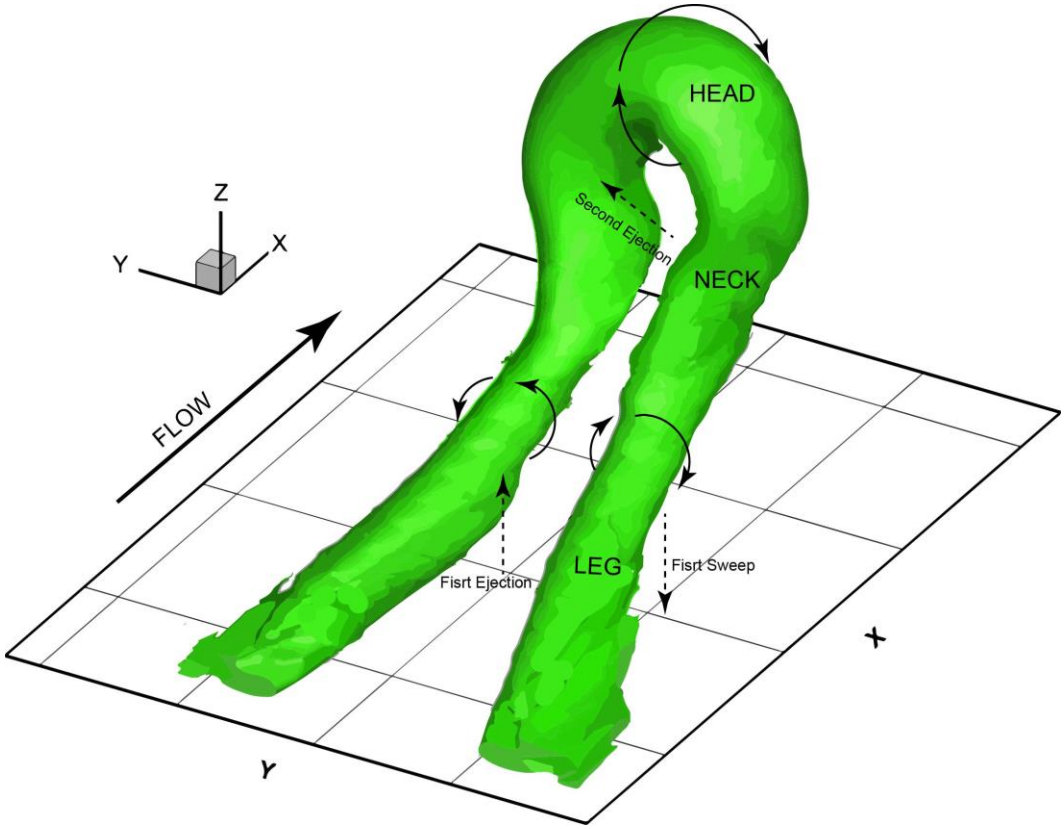

Figure 6-1 The sketch of a typical symmetric hairpin vortex.[52]

6.2 Hainpin vortex generation and development

A series of snapshots are obtained from DNS database to investigate the development of Λ vortex to hairpin vortex packets. Figure 6-2 shows the iso-surface of $\Omega = 0.52$ and $\|\boldsymbol{A}\|_F = 0.6$ at $t = 6.16T$, where T is the period of T-S wave. From Figure 6-2(b), we find the first ring generates at the top of the high strain rate region. Comparing Figure 6-2(b) with Figure 4-16(c), the high strain rate region moves up. This also can be checked by Figure 6-3, which shows the iso-surface of $\Omega = 0.52$ and $\|\boldsymbol{A}\|_F = 0.6$ at $t = 6.30T$. Comparing Figure 6-3 with Figure 6-2(b), the second high strain rate region moves upper at $t = 6.30T$. Then the second ring generates following as a result.

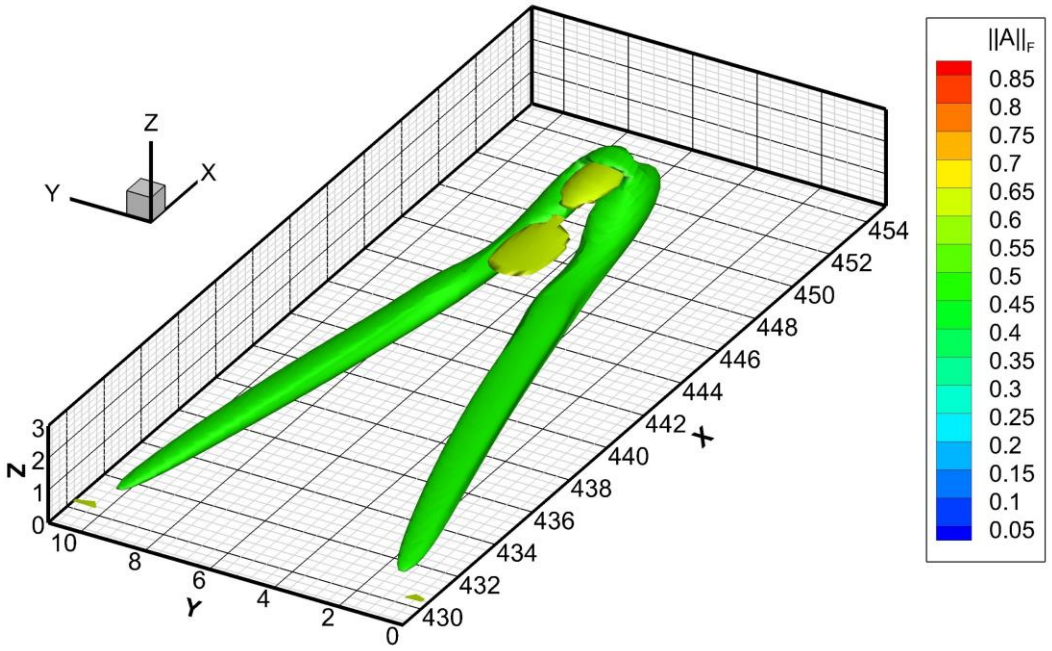

(a) Global view

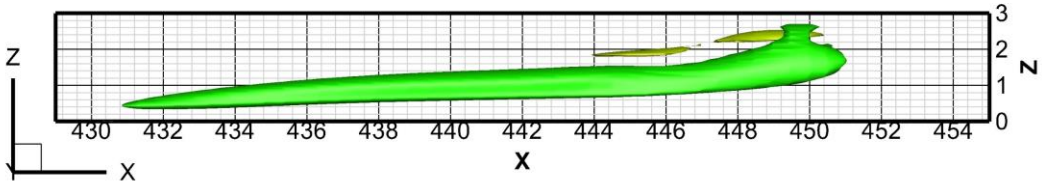

(b) X-Z view

Figure 6-2. The iso-surface of $\Omega = 0.52$ and $\|\boldsymbol{A}\|_F = 0.6$ at $t = 6.16T$, where T is the period of T-S wave.

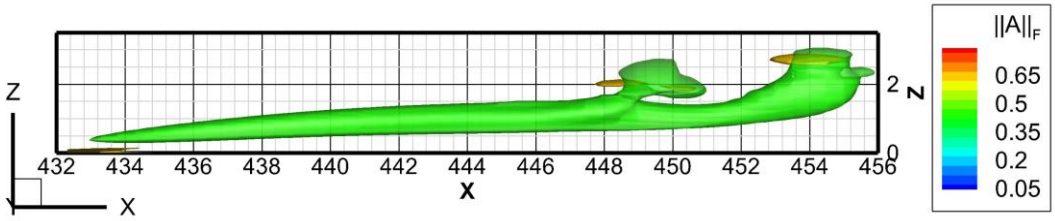

Figure 6-3 The iso-surface of $\Omega = 0.52$ and $\|\boldsymbol{A}\|_F = 0.6$ at $t = 6.30T$, where T is the period of T-S wave.

Note that in Figure 6-3, there is a protuberance at the “mandible” of the second ring. This protuberance grows along lower front direction to enfold the legs of the first vortex ring. It is more clear in Figure 6-4. Figure 6-4 gives the vortex structures at $t = 6.43T$ in global, X-Z and X-Y view. The red arrows indicate the direction of the protuberance developing.

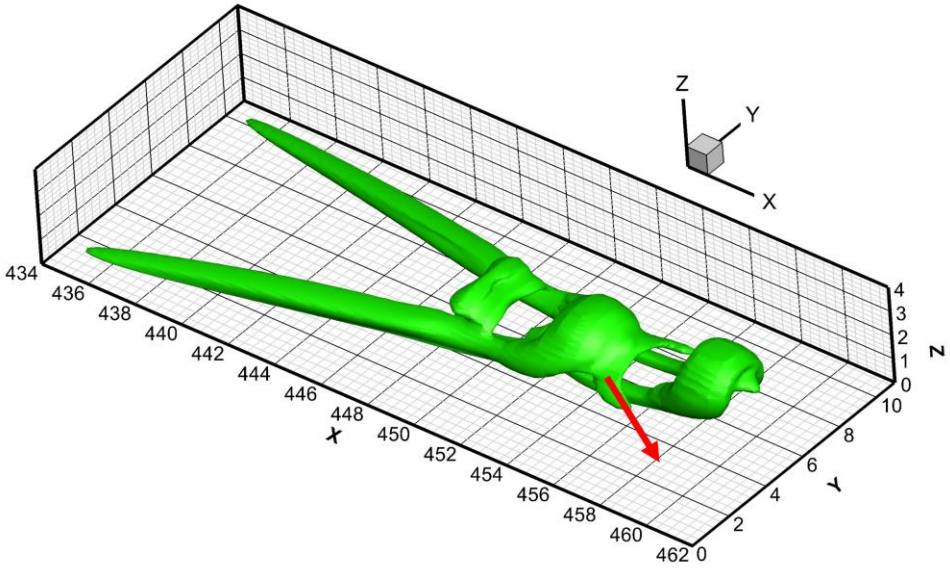

(a) Global view

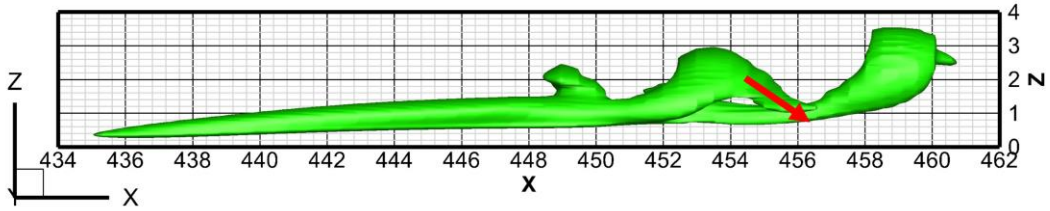

(b) X-Z view

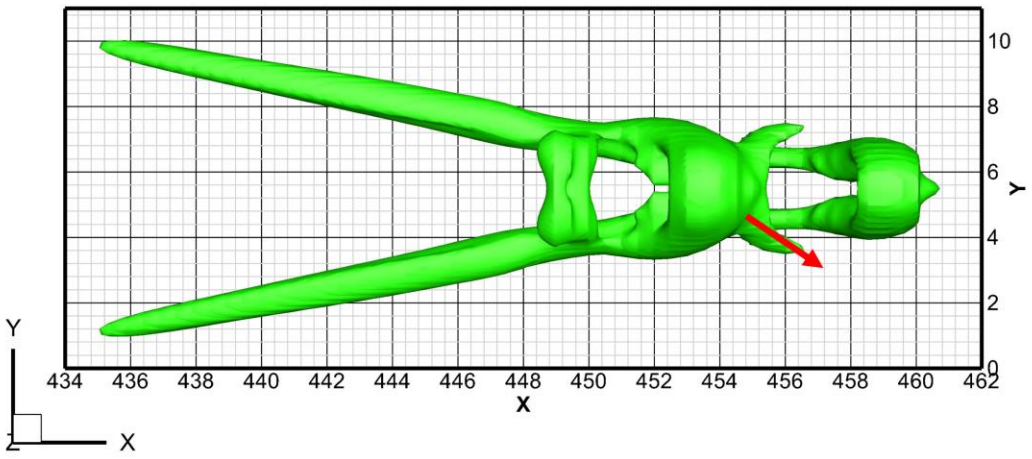

(c) X-Y view

Figure 6-4 The iso-surface of $\Omega = 0.52$ at $t = 6.43T$, where T is the period of T-S wave.

Figure 6-5 shows the the vortex structures at $t = 6.43T$ in X-Z view, X-Y top view and bottom view. The protuberance extends to the bottom and is parallel to the leg of the first hairpin vortex, see Figure 6-5(a). And the first hairpin vortex has been separated from the Λ-vortex, see Figure 6-5(c).

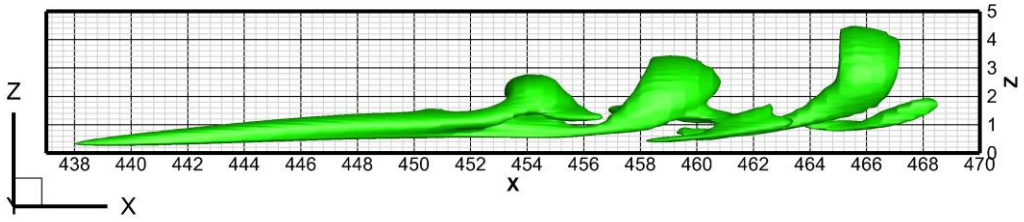

(a) X-Z view

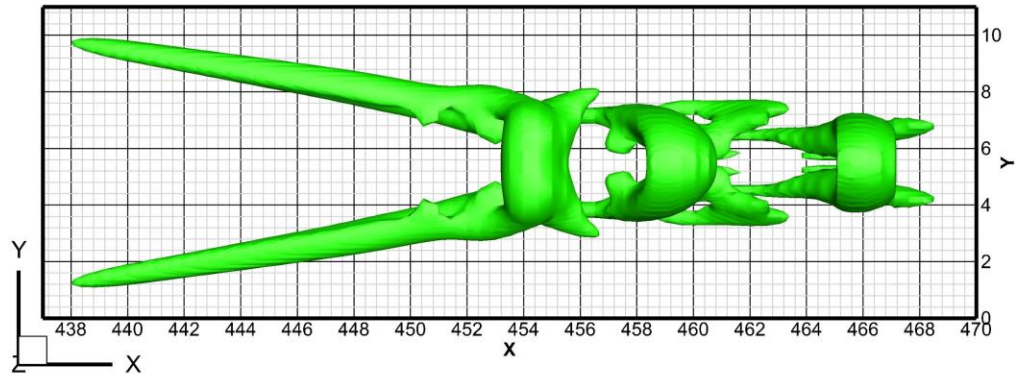

(b) X-Y view (Top)

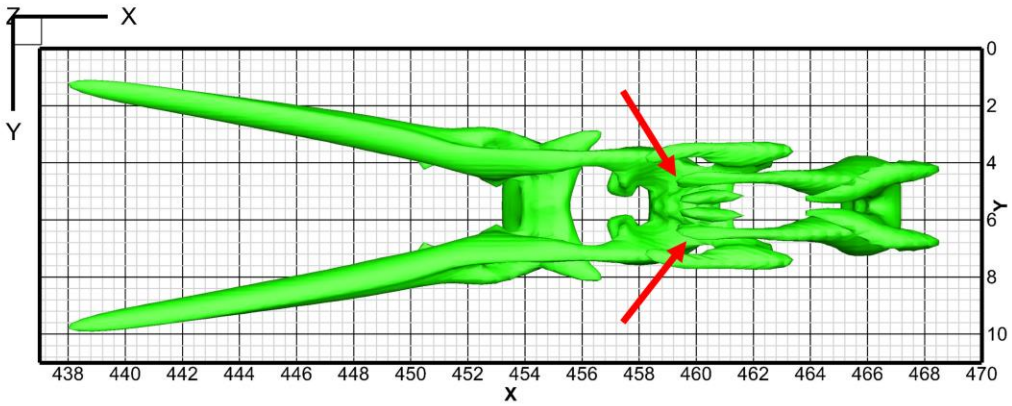

(c) X-Y view (Bottom)

Figure 6-5 The iso-surface of $\Omega = 0.52$ at $t = 6.60T$, where T is the period of T-S wave.

The distribution of ω_x on the slice of $x = 475$ with stream traces (black lines) at $t = 6.60T$ is shown in Figure 6-6. We can find the protuberance and the leg of the first hairpin are counter-rotating, see Figure 6-6(b). This is the possible reason that the first hairpin vortex separate from the Λ-vortex. Also from Figure 6-6(a), we can find the separations of the first three hairpin vortex from Λ-vortex have the similar process, that is, the separations are all with the extension of the protuberance of latter one.

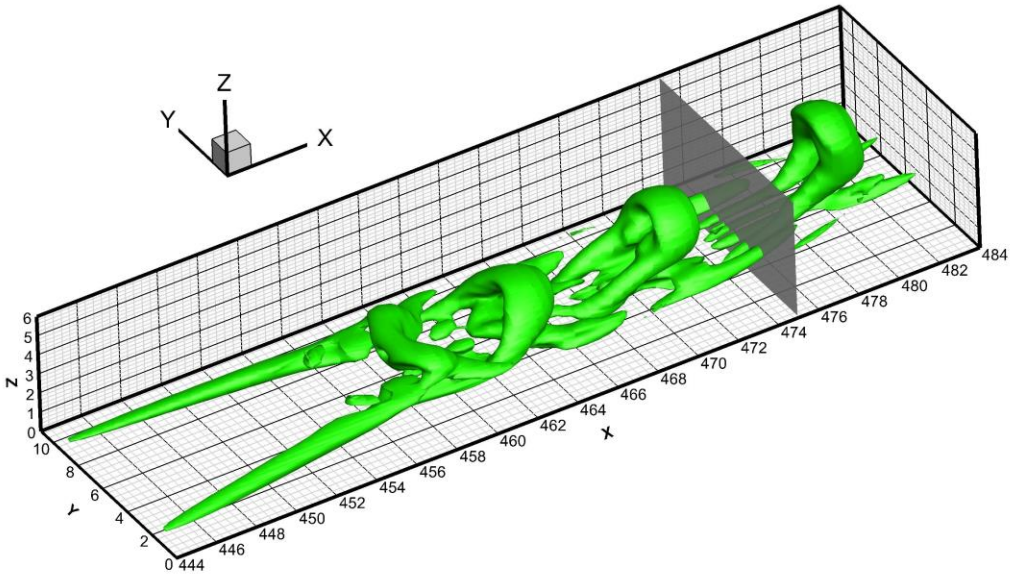

(a) The position of slice of $x = 475$

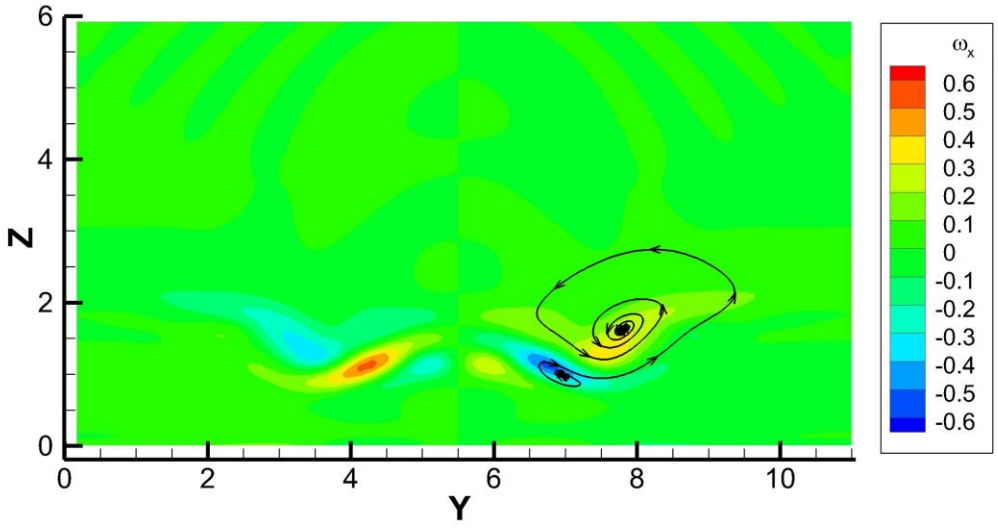

(b)

Figure 6-6 The distribution of ω_x on the slice of $x = 475$ with stream traces (black lines) at $t = 6.90T$, where T is the period of T-S wave.

The process of the generation of the fourth and fifth hairpin vortices is different from the first three hairpins, see Figure 6-7. The generation of the fourth and fifth hairpin

vortices is accompanying with the development of inverted Λ-vortex. And these inverted Λ-vortices rotate opposite to Λ-vortex, see Figure 6-8.

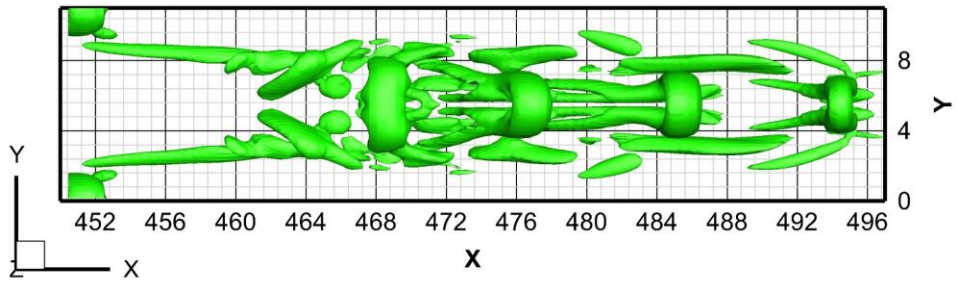

(a) $t = 7.20T$

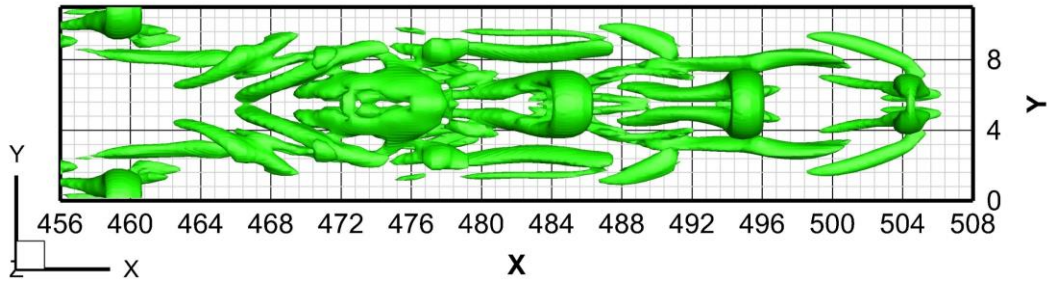

(b) $t = 7.40T$

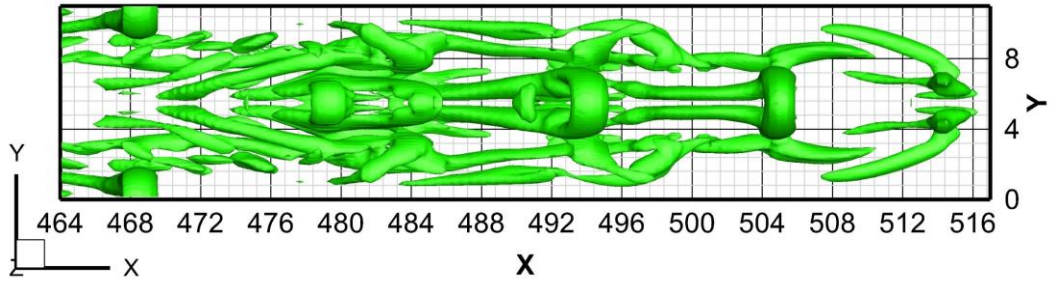

(c) $t = 7.60T$

Figure 6-7 The process of the fourth and fifth hairpin vortices generation in top view.

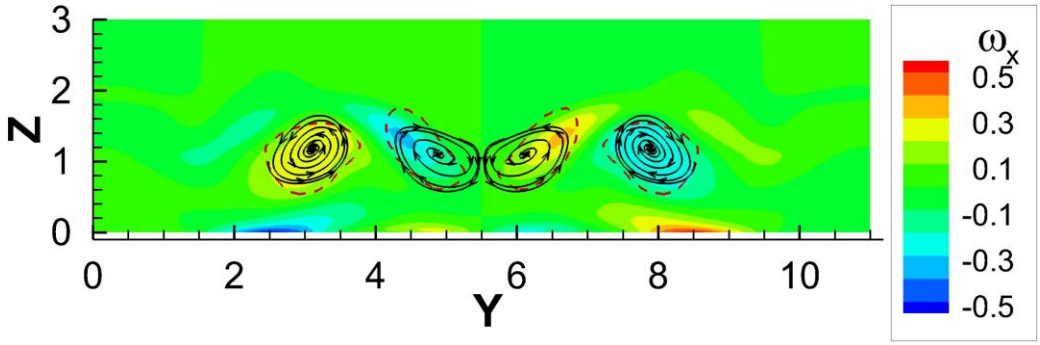

Figure 6-8 The distribution of ω_x on the slice of $x = 462$ with stream traces (black lines) at $t = 7.20T$, where T is the period of T-S wave. The red dashed circles are the contour of $\Omega = 0.52$.

The Λ vortex develops into a hairpin vortex packet containing five hairpin vortices, according to our observation from DNS data. There are no more hairpin vortices generate in one packets and it maybe because the original Λ vortex structure has ceased to exist, see Figure 6-7(c). And there are no enough energy to eject the low speed near the wall up to generate new high shear layers.

6.3 High Speed Zone around Hairpin Vortex

In the process of investigating hairpin vortex packets generation, our group found an interesting phenomenon [63] : the maximum velocity around some vortex rings in boundary layer flows locates near the neck of hairpin vortex, and this maximum velocity is greater than 1, namely, the initial velocity. Furthermore, the high-speed region comes into sight when the vortex ring becomes perpendicular.

Figure 6-9 shows three consecutive vortex rings and their streamwise velocity distribution. Figure 6-9(c) shows the maximum streamwise velocity of this vortex ring is at

top of it while the first vortex ring in Figure 6-9(a) is more perpendicular with maximum velocity around the neck region shown in Figure 6-9(b). For the third vortex ring, which is oblique more obviously, the maximum velocity also locates at the top as illustrated in Figure 6-9(d).

From Figure 6-9(c) and Figure 6-9(d), we can see that even when the maximum velocity locates at the top of vortex ring, the maximum streamwise velocity reaches 1.05, or even 1.06. This maximum speed is higher than the incoming velocity, and cannot be caused by inflow disturbance since the disturbance is much smaller.

Figure 6-10 shows the iso-surface of streamwise velocity u=1.045. It can be found that the maximum velocity around some vortex rings locates around the neck region while the maxima around some rings are on the top. Figure 6-10 also verified the assumption that, when the ring is more perpendicular, the maxima tend to locate at the neck region rather than on the top.

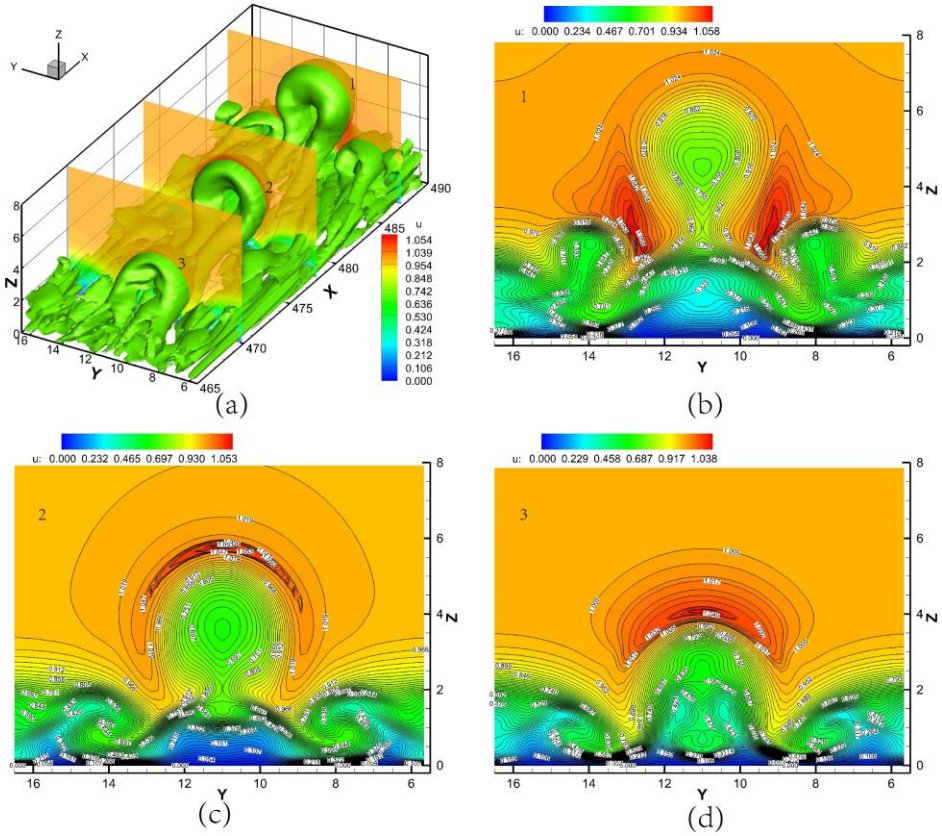

Figure 6-9 Three consecutive vortex rings and their streamwise velocity distribution.

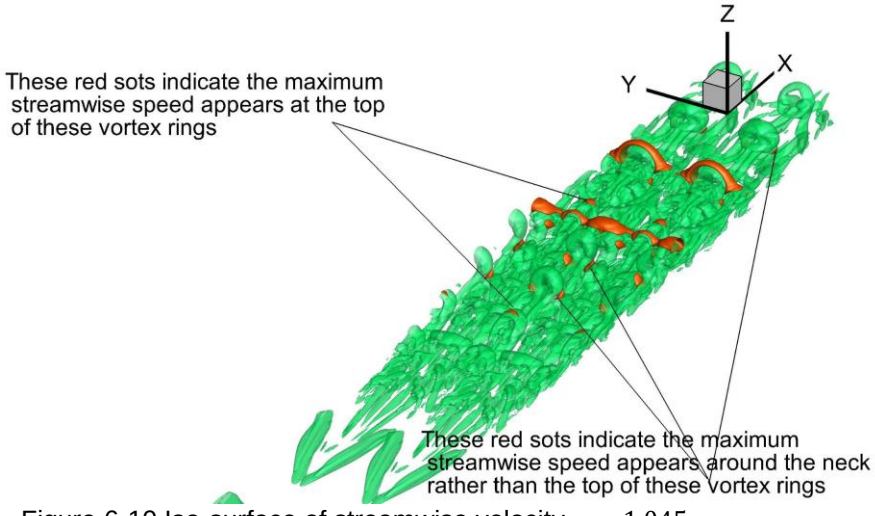

Figure 6-10 Iso-surface of streamwise velocity $u = 1.045$.

6.4 Summary

In this chapter, the development of Λ vortex to hairpin vortex packet is shown in detail. The generation of vortex ring is accompanied by a move-up of shear, and the former hairpin vortex separating from Λ vortex is always accompanied by the “mandible” development of latter hairpin vortex. The inverted Λ vortex generates before the fourth and fifth hairpin vortices form and the inverted Λ vortex rotate in an opposite direction to the main Λ vortex. The high-speed zone around hairpin vortex is not always at the top of the head of vortex ring. When vortex ring is more perpendicular, the high-speed zone locates around neck region of the hairpin vortex.

This development is in very early stage of transition, so the vortical structures are organized and sparse. With the advance of time, the hairpin vortex packets will intertwine and interact with each other. So, the vortical structures in late stage of transition will be more complicated and chaotic. To investigate the vortical structures in late stage of transition, the proper orthogonal decomposition will be utilized in next chapter.

Chapter 7

Late-stage Transitional Boundary Layer Structures POD analysis

In this chapter, we will use the proper orthogonal decomposition (POD) method [64] in the Euclidean space $\mathbb{R}^m$ to analyze the boundary layer structures in late-stage transition. In section 7.1, we will revisit POD and apply POD on late stage of transitional boundary layer in section 7.2 to investigate the principal component of the flow field.

7.1 Proper Orthogonal Decomposition

The goal of POD is to find a proper orthonormal basis, the POD basis $\{\psi_i\}_{i=1}^d$ of rank d, for the snapshot set spanned by n given vectors (the so-called snapshots) $y_1, \dots, y_n \in \mathbb{R}^m$. We assume that $d \leq \min\{m, n\}$ holds true.

Let $Y = (y_1, \dots, y_n)$ be a real-valued $m \times n$ matrix of rank $d \leq \min\{m, n\}$ with columns $y_j \in \mathbb{R}^m, 1 \leq j \leq n$. Singular value decomposition (SVD) [65] guarantees the existence of real numbers $\sigma_1 \geq \sigma_2 \geq \cdots \geq \sigma_d > 0$ and orthogonal matrices $\Psi \in \mathbb{R}^{m\times m}$ with columns $\{\psi_i\}_{i=1}^m$ and $\Phi \in \mathbb{R}^{n\times n}$ with columns $\{\phi_i\}_{i=1}^n$ such that

$$\Psi^t Y \Phi = \begin{pmatrix} D & 0 \\ 0 & 0 \end{pmatrix}, \tag{7-1}$$

where $D = diag(\sigma_1, \dots, \sigma_d) \in \mathbb{R}^{d\times d}$ and 't' stands for the transpose of a matrix. Moreover, the vectors $\{\psi_i\}_{i=1}^d$ and $\{\phi_i\}_{i=1}^d$ satisfy

$$Y\phi_i = \sigma_i \psi_i \text{ and } Y^t \psi_i = \sigma_i \phi_i \text{ for } i = 1, \dots, d. \tag{7-2}$$

They are eigenvectors of YY^t and Y^tY, respectively, with eigenvalues $\lambda_i = \sigma_i^2 > 0, i = 1, \dots, d$. The vectors $\{\psi_i\}_{i=d+1}^m$ and $\{\phi_i\}_{i=d+1}^n$ are eigenvectors of YY^t and Y^tY with eigenvalue 0.

Since Ψ is orthogonal, we find that

$$y_j = \sum_{i=1}^{d} \langle \psi_i, y_j \rangle_{\mathbb{R}^m} \psi_i \text{ for } j = 1, \dots, n, \tag{7-3}$$

where $\langle \cdot, \cdot \rangle_{\mathbb{R}^m}$ denotes the canonical inner product in $\mathbb{R}^m$. We denote $M_{i,j} = \langle \psi_i, y_j \rangle_{\mathbb{R}^m} \psi_i$ as the i-th mode of snapshot y_j. Note that $y_j = \sum_{i=1}^{d} M_{i,j}$ and we use, in practical application, the first ℓ ($\ell \leq d$) modes to reconstruct the snapshot, say y_{rec_j}. And the error of reconstruction is defined as $err_j = \|y_j - y_{rec_j}\|$.

Next we turn to the practical computation of a POD-basis of rank ℓ. If $n < m$ then one can determine the POD basis of rank ℓ as follows: Compute the eigenvectors $\phi_1, \dots, \phi_\ell \in \mathbb{R}^n$ by solving the symmetric $n \times n$ eigenvalue problem

$$Y^t Y \phi_i = \lambda_i \phi_i \quad \text{for } i = 1, \dots, \ell, \tag{7-4}$$

and set, by Eq (7-2),

$$\psi_i = \frac{1}{\sqrt{\lambda_i}} Y \phi_i \quad \text{for } i = 1, \dots, \ell. \tag{7-5}$$

For historical reasons this method of for determine the POD-basis is sometimes called the method of snapshots. On the other hand, if $m < n$ holds, we can obtain the POD basis by solving the $m \times m$ eigenvalue problem

$$Y Y^t \psi_i = \lambda_i \psi_i \quad \text{for } i = 1, \dots, \ell. \tag{7-6}$$

For the application of POD to concrete problems the choice of ℓ is certainly of central importance for applying POD. It appears that no general a-priori rules are available. Rather the choice of ℓ is based on heuristic considerations combined with observing the ratio of the modeled to the total energy contained in the system Y, which is expressed by

$$\mathcal{E}(\ell) = \frac{\sum_{i=1}^{\ell} \lambda_i}{\sum_{i=1}^{d} \lambda_i}. \tag{7-7}$$

7.2 POD on Late-stage Transitional Boundary Layer

In late-stage transitional boundary layer, the vortices develop into more complicated structures, see Figure 7-1. To investigate the principal components of these vortical structures, I apply POD over 100 snapshots of late transitional flow. A subzone is extracted to reduce the computation complexity. The parameters of the subzone are given in Table 7-1.

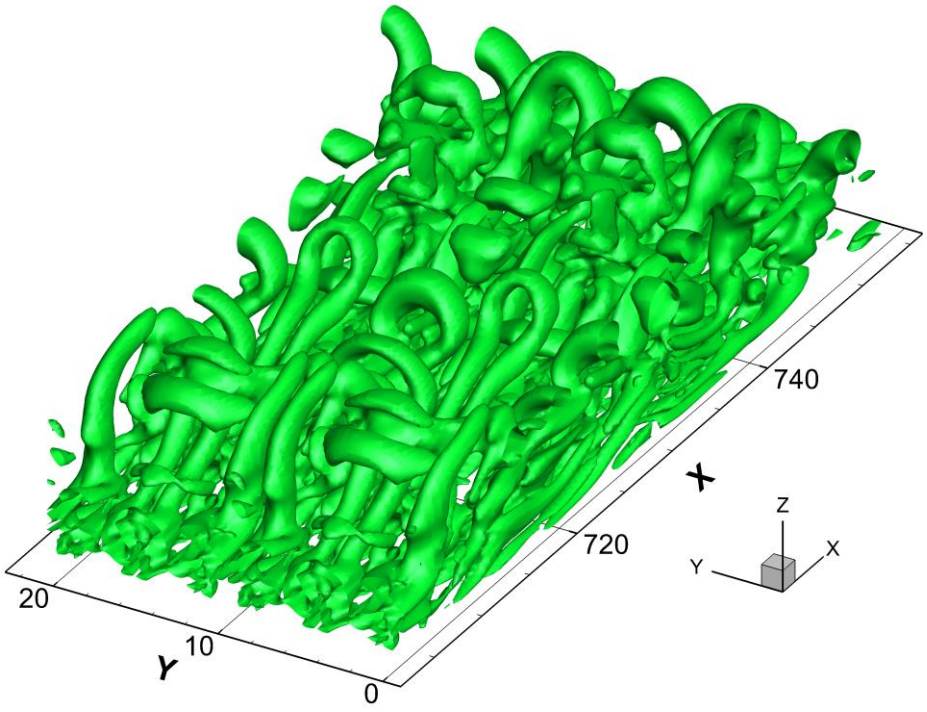

Figure 7-1 Vortical structures in late-stage transitional boundary layer.

Table 7-1 Parameters of subzone

	Start Index	End Index
I (in ξ direction)	161	260
J (in η direction)	1	128
K (in ζ direction)	1	200

The snapshot y_j is defined as

$$y_j = \begin{pmatrix} u^{(j)}_{161,1,1} \\ \vdots \\ u^{(j)}_{260,1,1} \\ u^{(j)}_{161,2,1} \\ \vdots \\ u^{(j)}_{260,2,1} \\ \vdots \\ u^{(j)}_{I,J,K} \\ \vdots \\ u^{(j)}_{260,128,200} \\ \vdots \\ v^{(j)}_{I,J,K} \\ \vdots \\ w^{(j)}_{I,J,K} \\ \vdots \\ w^{(j)}_{260,128,200} \end{pmatrix} \text{ for } j = 1, \dots, 100, \tag{7-8}$$

where $u^{(j)}, v^{(j)}$ and $w^{(j)}$ are velocity fields at $t = (17.5 + 0.01j)T$. So $y_j \in \mathbb{R}^m$ with $m = 7{,}680{,}000$ and $Y = (y_1, \dots, y_{100})$ is a matrix with dimension $7{,}680{,}000 \times 100$. After computing, the eigenvalues λ_i of matrix Y^tY are given in descent order in Figure 7-2.

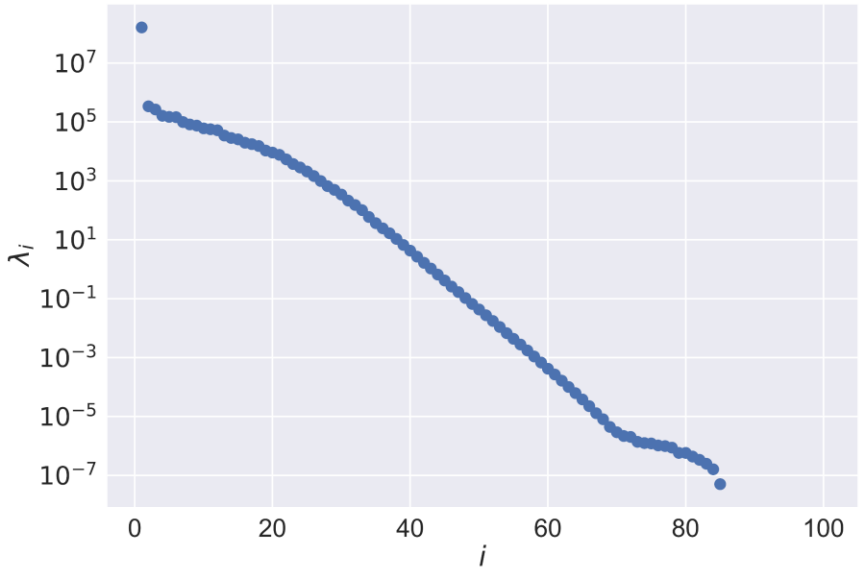

Figure 7-2 Eigenvalues λ_i of matrix Y^tY.

To choose the suitable number ℓ modes to reconstruct the snapshot, the ratio $\mathcal{E}(\ell)$ is shown in Figure 7-3. By the distribution of $\mathcal{E}(\ell)$, only first 20 modes will recover the snapshot very well. An intuitive comparison is given in Figure 7-4. Figure 7-4(a) shows the vortical structures at $t = 17.51T$ by iso-surface $\Omega = 0.52$ while Figure 7-4(b) shows the vortical structures based on the reconstructed data by first 20 modes. We can figure out, by comparison, the reconstruction performs very good.

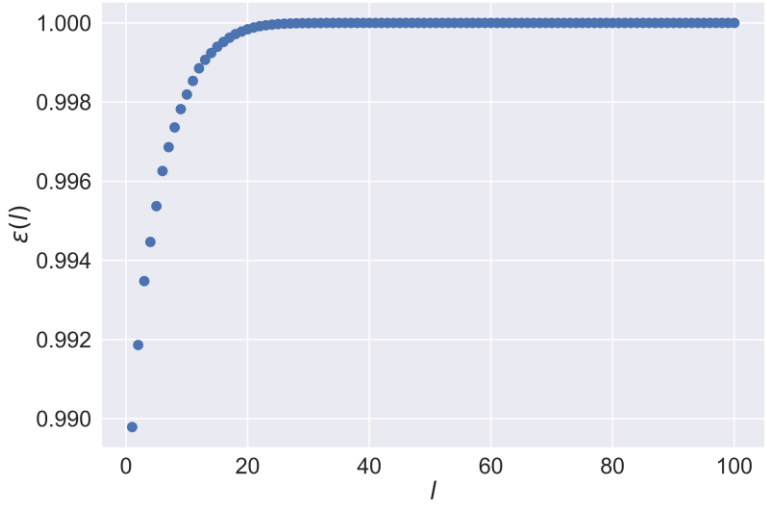

Figure 7-3 Distribution of $\mathcal{E}(\ell)$.

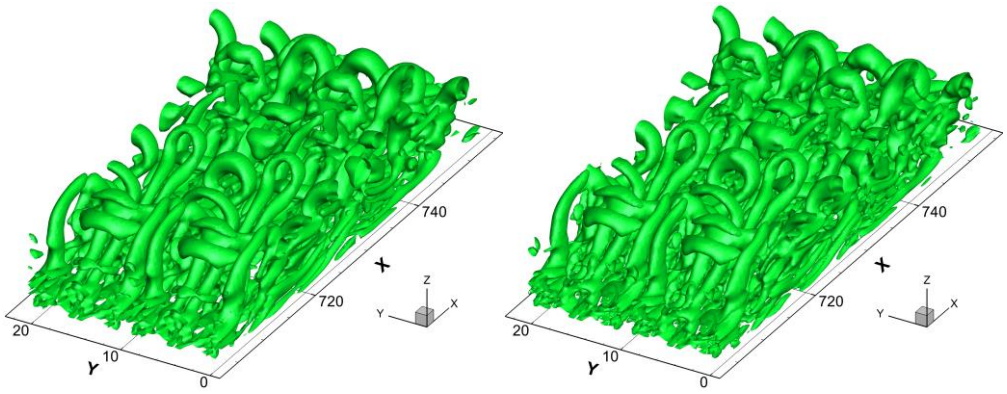

(a) (b)

Figure 7-4 Iso-surface of $\Omega = 0.52$ at $t = 17.51T$. (a) original data; (b) reconstructed data by first 20 modes.

More rigorously, a statistical result is given in Figure 7-5, which shows that the error of reconstruction with respect to modes amount. The black dots indicate the mean values of 100 snapshots and gray bars indicate the standard deviations.

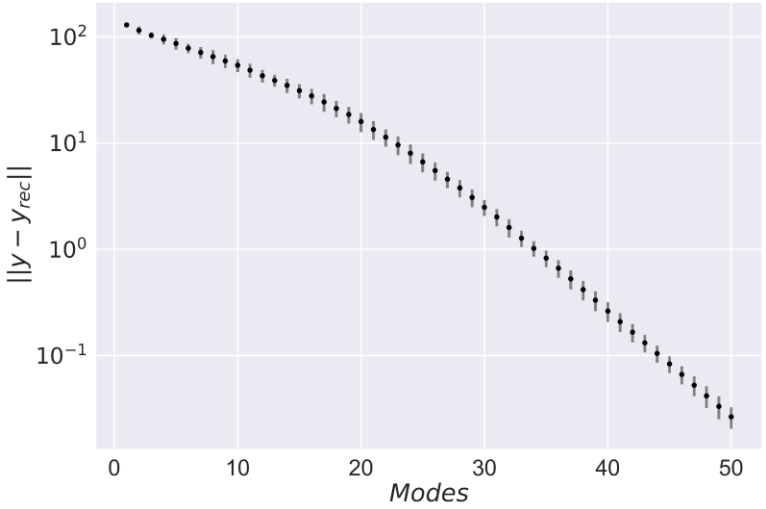

Figure 7-5 Error of reconstruction $\|y - y_{rec}\|$ with respect to modes amount used. Black dot indicates the mean of 100 snapshots and gray bar indicates the correlated standard deviation.

Figure 7-6 shows the vortical structures in first 30 modes at $t = 17.51T$. The vortical structures are indicated by iso-surfaces of $\Omega = 0.52$. We can find that some modes contribute to streamwise vortical structures, such as the first one. Some modes contribute to spanwise vortical structures, such as No.13. Some modes contribute to small scale vortical structures, such as No.14. And some modes even do not have vortical structures, like No.30, which means this mode contributes deformation. In fact, all modes after No.30 do not have vortical structures, which means the maximum Ω in these modes are all less than 0.5, see Figure 7-7.

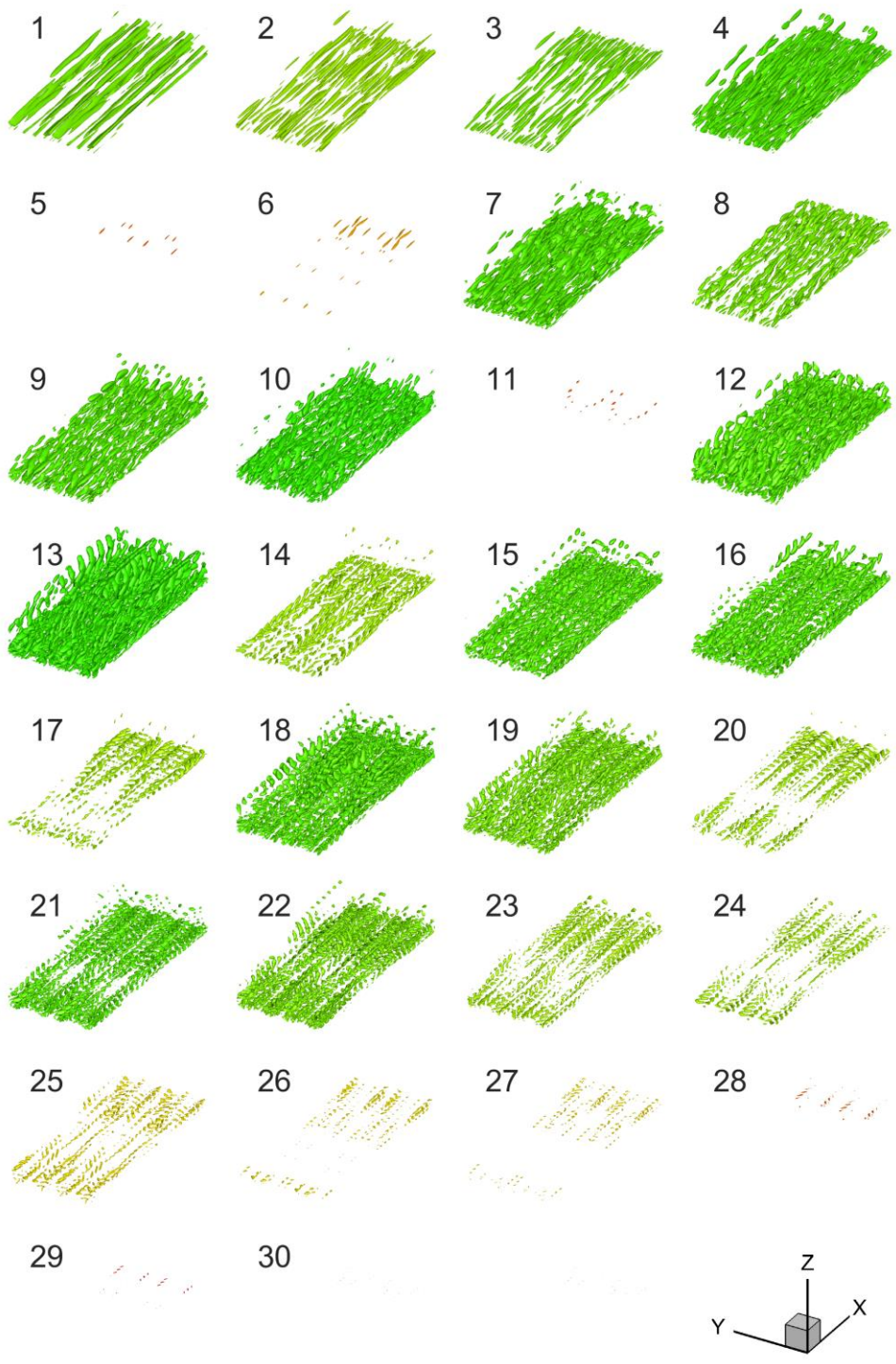

Figure 7-6 Vortical structures (iso-surfaces of $\Omega = 0.52$) of first 30 modes at $t = 17.51T$.

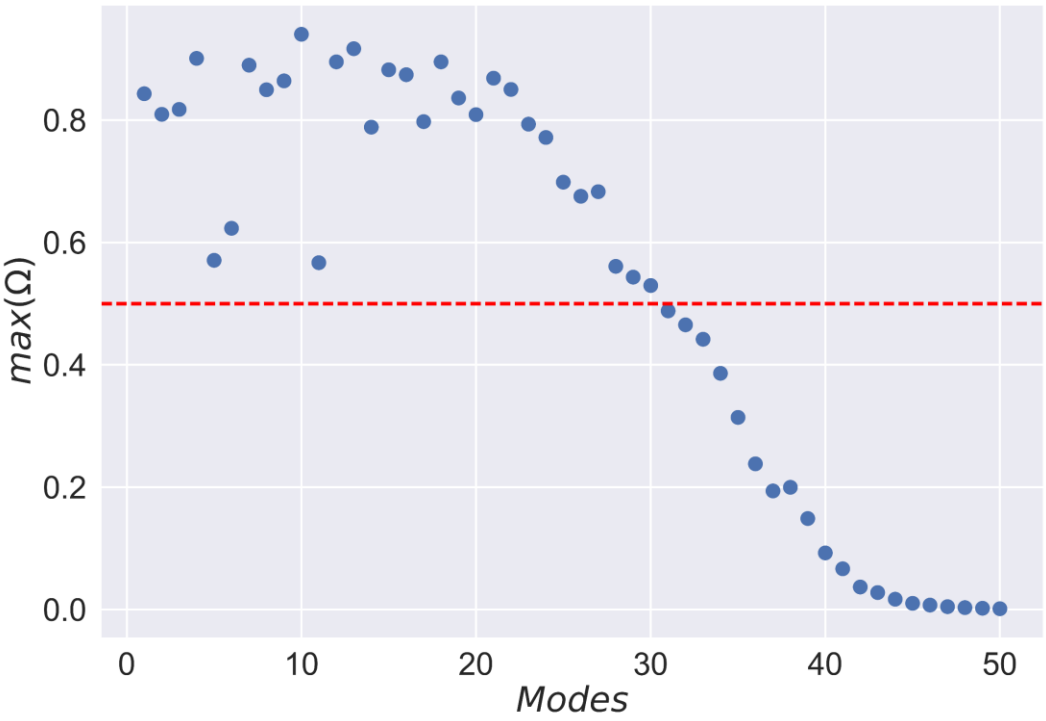

Figure 7-7 $\max(\Omega)$ in first 50 modes.

The first mode should obtain more attentions, because it is the most principal component with $\mathcal{E}(1) \approx 99\%$, see Figure 7-3. The vortical structures of the first mode at $t = 17.51T$ are given in Figure 7-8 in details. It tells us that the vortices in the first mode are streamwise vortices and they are in pair. It indicates that the mechanism of vortex rings generation in late-stage is the same as the first vortex packets: paired streamwise vortices eject the low speed zone at the bottom to the higher position, and high shear layers generate and develop into spanwise vortices which are vortex rings. Figure 7-9 gives the distribution of streamwise velocity u on a streamwise plane in the first mode. Figure 7-9(a) shows the position of the streamwise plane. The green surfaces are iso-surfaces of $\Omega = 0.52$, which indicate the vortices. Figure 7-9(b) gives the u distribution on the plane. The white circles are contour lines of $\Omega = 0.52$, which indicate the positions of

the vortices, and the black spirals are stream traces of particles. It clearly shows a pair of counter-rotating vortices eject the low speed zone up, which is similar with Figure 4-18(c).

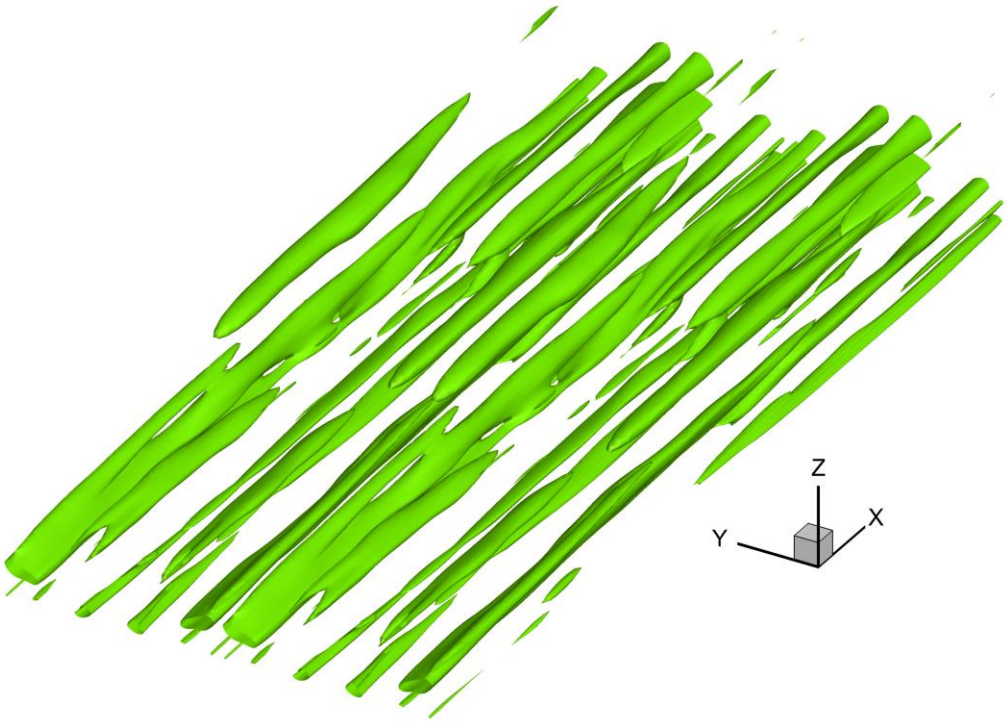

(a) Global view

(b) X-Z view

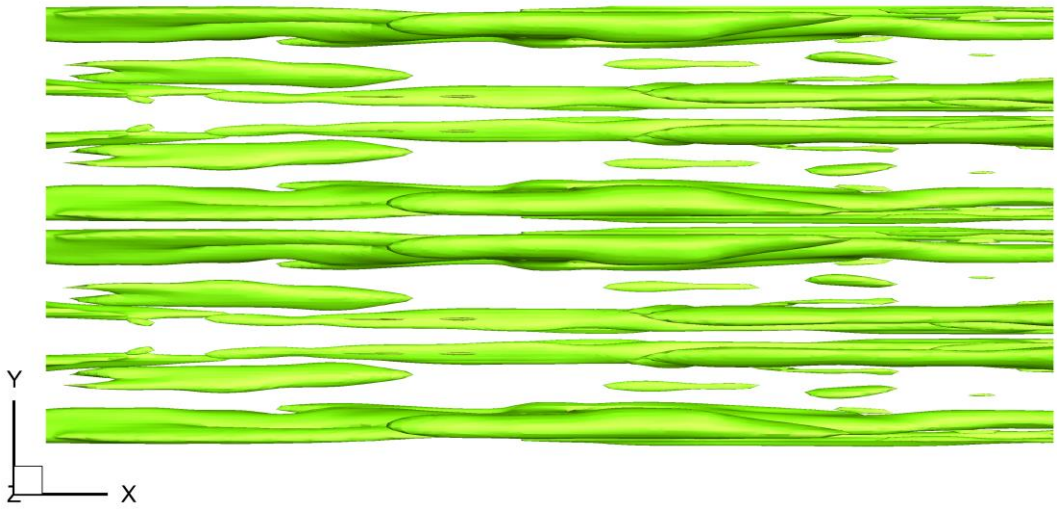

(c) X-Y view

(d) Y-Z view

Figure 7-8 The vortical structures of the first mode at $t = 17.51T$.

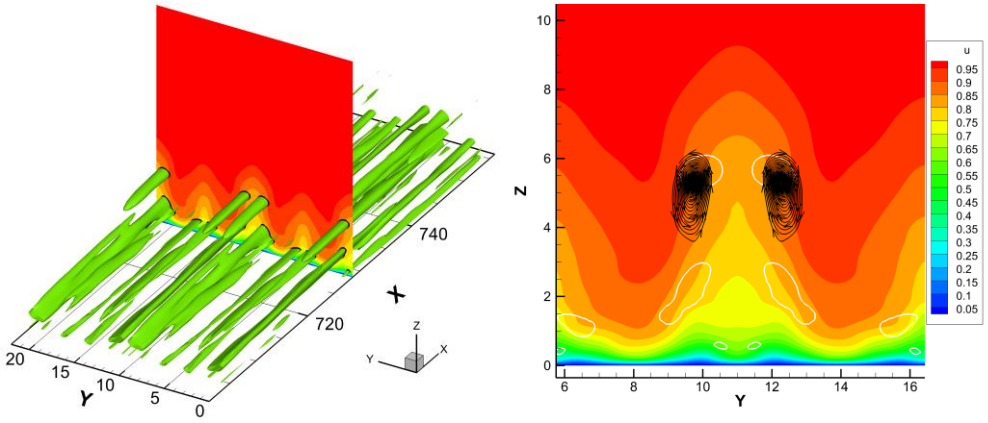

(a) (b)

Figure 7-9 The distribution of streamwise velocity u in first mode.

7.3 Summary

In this chapter, the proper orthogonal decomposition is applied to study the vortical structure in late stage of transitional boundary layer. By investigating the most principal component of the flow field, I find streamwise vortices play significant role in late stage of transition. It reveals the consistency of Liu's theory: a pair of streamwise vortices ejects the low speed zone up and high shear layer generates; because of the instability of the high shear layer in boundary layer, the vortex ring forms and vortex packet develops.

Chapter 8

Concluding Remarks

The tensor field $\nabla \boldsymbol{V}$ can be split into two parts: symmetric part (deformation) and antisymmetric part (vorticity). And based on the idea that vorticity overtakes deformation in vortices, a new vortex identification method, Ω-method, is posted. The Ω-method has a relative uniform threshold to reveal the vortical structures and it is proved that Ω-method can capture the low-pressure zone very well.

In the development of perturbation and formation of Λ vortex, the spanwise partial derivative of velocity plays a significant role. The Λ vortices are in pair with counter-rotation, resulting in an ejection effect that take the low speed near wall up. A high shear layer generates above the head of Λ vortices because of the ejection effect of Λ vortices. This high shear layer is unstable after Chebyshev spectral method is applied to solve the Orr-Sommerfeld eigenvalue equation.

The Λ vortex gradually develops into hairpin vortex packet. In the process of development, the generation of vortex ring is accompanied by a move-up of shear, and the former hairpin vortex separating from Λ vortex is always accompanied by the "mandible" development of latter hairpin vortex. The inverted Λ-vortex generates before the fourth and fifth hairpin vortices form and the inverted Λ-vortex rotate in an opposite direction to the main Λ vortex. The high-speed zone around hairpin vortex is not always at the top of the head of vortex ring. When vortex ring is more perpendicular, the high-speed zone locates around neck region of the hairpin vortex.

By proper orthogonal decomposition, the vortical structures in late stage of transition is studied. After investigating the most principal component of the flow field, the streamwise vortices are believed to play significant role in late stage of transition.

Appendix A

MATLAB Code of Chebyshev Spectral Method for Linear Stability

```
% main.m
% INPUT
%
% nosmod = number of Orr-Sommerfeld modes
% R      = Reynolds number
% alp    = alpha (streamwise wave number)
% beta   = beta (spanwise wave number)

    close all;
    clear all;

    zi=sqrt(-1);

% input data
    iflow=input('Poiseuille (1); Couette flow (2);Shear (3): ');
    nosmod=input('Enter N the number of OS modes: ');
    R=input('Enter the Reynolds number: ');
    alp=input('Enter alpha: ');
    beta=input('Enter beta: ');

% generate Chebyshev differentiation matrices
    [D0,D1,D2,D4]=Dmat(nosmod);


% mean velocity
    ak2=alp^2+beta^2;
    Nos=nosmod+1;
    yj=cos(pi*(0:1:Nos-1)'/(Nos-1));
    if iflow==1,
        u=ones(length(yj),1)-yj.^2;
        ddu=-2*ones(length(u),1);
    elseif iflow==2,
        u=yj;
        ddu=0*ones(length(u),1);
    elseif iflow==3,
        a=1;
        b=4;
        u=a*tanh(b*yj);
        ddu=-2*b^2*u.*(sech(b*yj)).^2;

    end;

% set up Orr-Sommerfeld matrices A and B
    B11=D2-ak2*D0;
    A11=-(D4-2*ak2*D2+(ak2^2)*D0)/(zi*alp*R);
    A11=A11+u*ones(1,length(u)).*B11-(ddu*ones(1,length(u))).*D0;
    er=-200*zi;
    A=[er*D0(1,:); er*D1(1,:); A11(3:Nos-2,:); ...
        er*D1(Nos,:); er*D0(Nos,:) ];
    B=[D0(1,:); D1(1,:); B11(3:Nos-2,:); ...
        D1(Nos,:); D0(Nos,:)];
```

```
% compute the Orr-Sommerfeld matrix (by inverting B)
    d=B\A;

    [xs,es]=iord2(d);

    k=find(imag(es)>0);
    if k
        disp(imag(es(k)));
        figure(1);
        vp=D0*xs(:,k);
        plot(sqrt(vp.*conj(vp)),yj);
    else
        disp('stable!!!');
    end
```

```
function [D0,D1,D2,D4]=Dmat(N)
%
% Function to create differentiation matrices

% N  = number of modes
% D0 = zero'th derivative matrix
% D1 = first derivative matrix
% D2 = second derivative matrix
% D4 = fourth derivative matrix

% initialize
    num=round(abs(N));

% create DO
    D0= [] ;
    vec=(0:1:num)' ;
    for j=0:1:num
        D0=[D0 cos(j*pi*vec/num)];
    end;

% create higher derivative matrices
    lv=length(vec);
    D1=[zeros(lv,1) D0(:,1) 4*D0(:,2)];
    D2=[zeros(lv,1) zeros(lv,1) 4*D0(:,1)];
    D3=[zeros(lv,1) zeros(lv,1) zeros(lv,1)];
    D4=[zeros(lv,1) zeros(lv,1) zeros(lv,1)];
    for j=3:num
        D1=[D1 2*j*D0(:,j)+j*D1(:,j-1)/(j-2)];
        D2=[D2 2*j*D1(:,j)+j*D2(:,j-1)/(j-2)];
        D3=[D3 2*j*D2(:,j)+j*D3(:,j-1)/(j-2)];
        D4=[D4 2*j*D3(:,j)+j*D4(:,j-1)/(j-2)];
    end;
```

```
function [xs,es]=iord2(d)

% This function computes the eigenvalues of a matrix d and
% orders the eigenvalues so that the imaginary parts are
% decreasing.
%
% INPUT
% d = input matrix
%
% OUTPUT
% es = ordered eigenvalues
% xs = eigenvectors

    [v,e]=eig(d) ;
    e=diag(e);
    [eimag,is]=sort(-imag(e));
    xs=v(: ,is);
          es=e(is);
```

References

[1] H. Helmholtz, “Über Integrale der hydrodynamischen Gleichungen, welche den Wirbelbewegungen entsprechen,” *J. für die reine und Angew. Math.*, vol. 55, pp. 25–55.

[2] H. Lamb, *Hydrodynamics*. Cambridge university press, 1932.

[3] L. Prandtl, “Uber Flüssigkeitsbewegung bei sehr kleiner Reibung,” *Verhandlungen des dritten Int. Math.*, vol. Heidelberg, pp. 484–491, 1904.

[4] W. F. Durand, *Aerodynamic Theory*. Berlin, Heidelberg: Springer Berlin Heidelberg, 1935.

[5] S. Goldstein, *Modern developments in fluid mechanics. Vol. II*. 1938.

[6] D.Küchemann, “Report on the IUTAM symposium on concentrated vortex motions in fluids,” *J. Fluid Mech.*, vol. 21, pp. 1–20, 1965.

[7] T. Theodorsen, “Mechanism of turbulence,” in *Proceedings of the Second Midwestern Conference on Fluid Mechanics (Vol. 1719)*, 1952.

[8] C. Liu and Z. Liu, “Multigrid Mapping and Box Relaxation for Simulation of the Whole Process of Flow Transition in 3D Boundary Layers,” *J. Comput. Phys.*, vol. 119, no. 2, pp. 325–341, Jul. 1995.

[9] C. Liu and Z. Liu, “Direct numerical simulation for flow transition around airfoils,” in *Proceedings of First AFOSR International Conference on DNS/LES*, 1997, pp. 13–28.

[10] S. Bake, D. G. W. Meyer, and U. Rist, “Turbulence mechanism in Klebanoff transition: a quantitative comparison of experiment and direct numerical simulation,” *J. Fluid Mech.*, vol. 459, pp. 217–243, 2002.

[11] X. Wu and P. Moin, “Direct numerical simulation of turbulence in a nominally zero-pressure-gradient flat-plate boundary layer,” *J. Fluid Mech.*, vol. 630, p. 5, 2009.

[12] Z. W. Duan, Z. X. Xiao, and S. Fu, “Direct numerical simulation of hypersonic transition induced by an isolated cylindrical roughness element,” *Sci. China Physics, Mech. Astron.*, vol. 57, no. 12, pp. 2330–2345, 2014.

[13] M. R. Head and P. Bandyopadhyay, “New aspects of turbulent boundary-layer structure,” *J. Fluid Mech.*, vol. 107, no. 1981, p. 297, 1981.

[14] F. R. Hama and J. Nutant, “Detailed flow-field observations in the transition process in a thick boundary layer,” in *Proceedings of the 1963 Heat Transfer and Fluid Mechanics Institute*, 1963, pp. 77–93.

[15] S. J. Kline, W. C. Reynolds, F. A. Schraubt, and P. W. Runstadlers, “The structure of turbulent boundary layers,” *J . Fluid Meeh*, vol. 30, no. 4, pp. 741–773, 1967.

[16] E. R. Corino and R. S. Brodkey, “A visual investigation of the wall region in turbulent flow,” *J. Fluid Mech.*, vol. 37, no. 1, p. 1, 1969.

[17] T. Herbert, “Secondary Instability of Boundary Layers,” *Annu. Rev. Fluid Mech.*, vol. 20, no. 1, pp. 487–526, Jan. 1988.

[18] Y. S. Kachanov, “Physical Mechanisms of Laminar-Boundary-Layer Transition,” *Annu. Rev. Fluid Mech.*, vol. 26, no. 1, pp. 411–482, Jan. 1994.

[19] J. Kim, P. Moin, and R. Moser, “Turbulence statistics in fully developed channel flow at low Reynolds number,” *J. Fluid Mech.*, vol. 177, no. 1, p. 133, 1987.

[20] P. R. Spalart, “Direct simulation of a turbulent boundary layer up to R=1410,” *J. Fluid Mech.*, vol. 187, pp. 61–98, 1988.

[21] P. Moin and K. Mahesh, “DIRECT NUMERICAL SIMULATION: A Tool in Turbulence Research,” *Annu. Rev. Fluid Mech.*, vol. 30, no. 1, pp. 539–578, 1998.

[22] C. R. Smith, J. D. A. Walker, A. H. Haidari, and U. Sobrun, “On the Dynamics of Near-Wall Turbulence,” *Philos. Trans. R. Soc.*, vol. 336, no. 1641, pp. 131–175, 1991.

[23] S. Robinson, “Coherent Motions In The Turbulent Boundary Layer,” *Annu. Rev. Fluid Mech.*, vol. 23, no. 1, pp. 601–639, 1991.

[24] S. K. Robinson, “A perspective on coherent structures and conceptual models for turbulent boundary layer physics,” in *AIAA, Fluid Dynamics, Plasma Dynamics and Lasers Conference,21st*, 1990, p. 17.

[25] W. Schoppa and F. Hussain, “Coherent structure generation in near-wall turbulence,” *J. Fluid Mech.*, vol. 453, pp. 57–108, 2002.

[26] C. Liu and L. Zhining, “Multigrid mapping and box relaxation for simulation of the whole process of flow transition in 3D boundary layers,” *J. Comput. Phys.*, vol. 119, no. 2, pp. 325–341, 1995.

[27] Z. Liu, G. Xiong, and C. Liu, “Direct numerical simulation for the whole process of transition on 3-D airfoils,” in *Fluid Dynamics Conference*, 1996.

[28] R. J. Adrian, “Hairpin vortex organization in wall turbulencea,” *Phys. Fluids*, vol. 19, no. 4, 2007.

[29] U. Rist and H. Fasel, “Direct numerical simulation of controlled transition in a flat-plate boundary layer,” *J. Fluid Mech.*, vol. 298, no. 1, p. 211, 1995.

[30] T. Sayadi, C. W. Hamman, and P. Moin, “Direct numerical simulation of complete H-type and K-type transitions with implications for the dynamics of turbulent boundary layers,” *J. Fluid Mech.*, vol. 724, pp. 480–509, Jun. 2013.

[31] C. Liu, Y. Yan, and P. Lu, “Physics of turbulence generation and sustenance in a boundary layer,” *Comput. Fluids*, vol. 102, pp. 353–384, Oct. 2014.

[32] G. K. (George K. Batchelor, *An introduction to fluid dynamics*. Cambridge University Press, 1999.

[33] P. G. Saffman, *Vortex dynamics*. Cambridge University Press, 1992.

[34] H. J. Lugt, *Introduction to Vortex Theory*. 1997.

[35] J. Wu, H. Ma, and M. Zhou, *Vorticity and Vortex*. Springer Science & Business Media, 2007.

[36] W. Schoppa and F. Hussain, “Formation of near-wall streamwise vortices by streak instability,” in *IUTAM Symposium on Simulation and Identification of Organized Structures in Flows*, 1999, pp. 61–78.

[37] H.-S. Dou, “Physics of flow instability and turbulent transition in shear flows,” *Int. J. Phys. Sci.*, vol. 6, no. 6, pp. 1411–1425, 2011.

[38] J. Zhou, R. J. Adrian, and S. Balachandar, “Autogeneration of near-wall vortical structures in channel flow,” *Phys. Fluids*, vol. 8, no. 1, p. 288, 1996.

[39] J. Zhou, R. J. Adrian, S. Balachandar, and T. M. Kendall, “Mechanisms for generating coherent packets of hairpin vortices in channel flow,” *J. Fluid Mech.*, vol. 387, p. S002211209900467X, May 1999.

[40] J. M. Wallace, “Highlights from 50 years of turbulent boundary layer research,” *J. Turbul.*, vol. 13, no. July 2015, p. N53, 2012.

[41] P. Davidson, *Turbulence: An Introduction for Scientists and Engineers*. Oxford University Press, 2004.

[42] J. Jeong and F. Hussain, “On the identification of a vortex,” *J. Fluid Mech.*, vol. 285, no. 1, p. 69, Feb. 1995.

[43] L. D. Landau and E. M. Lifshitz, *Fluid Mechanics*, vol. 6, no. 1. Pergamon books Ltd, 1987.

[44] S. K. Robinson, “Coherent Motions In The Turbulent Boundary Layer,” *Annu. Rev. Fluid Mech.*, vol. 23, no. 1, pp. 601–639, 1991.

[45] A. E. Perry and M. S. Chong, “A Description of Eddying Motions and Flow Patterns Using Critical-Point Concepts,” *Annu. Rev. Fluid Mech.*, vol. 19, no. 1, pp. 125–155, Jan. 1987.

[46] J. C. R. Hunt, A. A. Wray, and P. Moin, “Eddies, streams, and convergence zones in turbulent flows,” in *Center for Turbulence Research, Proceedings of the Summer Program*, 1988, pp. 193–208.

[47] G. Haller, “An objective definition of a vortex,” *J. Fluid Mech.*, vol. 525, pp. 1–26, 2005.

[48] S. C. Shadden, F. Lekien, and J. E. Marsden, “Definition and properties of Lagrangian coherent structures from finite-time Lyapunov exponents in two-dimensional aperiodic flows,” *Phys. D Nonlinear Phenom.*, vol. 212, no. 3–4, pp. 271–304, 2005.

[49] B. Pierce, P. Moin, and T. Sayadi, “Application of vortex identification schemes to direct numerical simulation data of a transitional boundary layer,” *Phys. Fluids*, vol. 25, no. 1, p. 15102, 2013.

[50] C. Liu and X. Cai, “New theory on turbulence generation and structure—DNS and experiment,” *Sci. China Physics, Mech. Astron.*, vol. 60, no. 8, p. 84731, 2017.

[51] C. Liu, Y. Wang, Y. Yang, and Z. Duan, “New omega vortex identification method,” *Sci. China Physics, Mech. Astron.*, vol. 59, no. 8, p. 684711, Aug. 2016.

[52] Y. Wang, H. Al-Dujaly, Y. Yan, N. Zhao, and C. Liu, “Physics of multiple level hairpin vortex structures in turbulence,” *Sci. China Physics, Mech. Astron.*, vol. 59, no. 2, p. 624703, Feb. 2016.

[53] S. K. Lele, “Compact Finite-Difference Schemes with Spectral-Like Resolution,” *J. Comput. Phys.*, vol. 103, no. 1, pp. 16–42, 1992.

[54] C. W. Shu and S. Osher, “Efficient implementation of essentially non-oscillatory shock-capturing schemes,” *J. Comput. Phys.*, vol. 77, no. 2, pp. 439–471, 1988.

[55] L. Jiang, H. Shan, and C. Liu, “Weighted compact scheme for shock capturing,” *Int. J. Comput. …*, no. October 2012, pp. 37–41, 2001.

[56] M. R. Malik, “Numerical methods for hypersonic boundary layer stability,” *J. Comput. Phys.*, vol. 86, no. 2, pp. 376–413, 1990.

[57] L. Jiang, C. L. Chang, M. Choudhari, and C. Liu, “Cross-validation of DNS and PSE results for instability wave propagation in compressible boundary layers past curvilinear surfaces,” 2003.

[58] L. Chen, X. Liu, M. Oliveira, and C. Liu, “DNS for Late Stage Structure of Flow Transition on a Flat-Plate Boundary Layer,” American Institute of Aeronautics and Astronautics, Orlando, Florida, Jan. 2010.

[59] P. Lu, Z. Wang, L. Chen, and C. Liu, “Numerical study on U-shaped vortex formation in late boundary layer transition,” *Comput. Fluids*, vol. 55, pp. 36–47, 2012.

[60] C. Liu and L. Chen, “Parallel DNS for vortex structure of late stages of flow transition,” *Comput. Fluids*, vol. 45, no. 1, pp. 129–137, 2011.

[61] C. Lee and R. Li, “Dominant structure for turbulent production in a transitional boundary layer,” *J. Turbul.*, vol. 8, no. 55, p. N55, Jan. 2007.

[62] S. Tian, Y. Yang, and C. Liu, “DNS Study on Chaotic Behavior of the Late Flow Transition and Turbulence,” in *The 10th CHAOS International Conference*, 2017.

[63] Y. Wang, Y. Yang, S. Chern, and C. Liu, “DNS Study on Motion around a Vortex Ring in Transitional Boundary Layers,” American Institute of Aeronautics and Astronautics, San Diego, California, Jan. 2016.

[64] S. Volkwein, *Proper Orthogonal Decomposition: Theory and Reduced-Order Modelling*. University of Konstanz, 2013.

[65] B. Noble, *Applied Linear Algebra*. Englewood Cliffs, NJ : Prentice-Hall, 1969.

Biographical Information

Yong Yang has received a Bachelor of Science degree in Aircraft Design and Engineering from Nanjing University of Aeronautics and Astronautics in China and a Master of Science degree in Applied Mathematics from University of Texas at Arlington. He worked at the Center for Numerical Simulation and Modeling for research projects for four years. He was awarded the National Scholarship in China in 2009 and Mathematics Academic Excellence Scholarship in University of Texas at Arlington in 2016 because of his academic excellence. His research at the University of Texas at Arlington has earned the Outstanding Graduate Research Award of Department of Mathematics in 2016. His research interests include computational fluid dynamics and numerical methods.